

High power continuous wave tunable laser sources from visible to Mid-IR based on optical parametric oscillators

By

Mukesh Kumar Shukla

PHYS11201204011

National Institute of Science Education and Research, Bhubaneswar

A thesis submitted to the

Board of Studies in Physical Sciences

In partial fulfillment of requirements

for the Degree of

Doctor of Philosophy

of

HOMI BHABHA NATIONAL INSTITUTE



February 2019

Homi Bhabha National Institute

Recommendations of the Viva Voce Committee

As members of the Viva Voce Committee, we certify that we have read the dissertation prepared by Mukesh Kumar Shukla entitled “**High power continuous wave tunable laser sources from visible to Mid-IR based on optical parametric oscillator**” and recommend that it maybe accepted as fulfilling the thesis requirement for the Degree of Doctor of Philosophy.

Bedangadas Mohanty Date: 5/2/2019
Chair - Prof. Bedangadas Mohanty

Ritwick Das Date: 05/02/19
Guide/Convener - Dr. Ritwick Das

M. R. Shenoy Date:
Examiner - Prof. M. R. Shenoy

Ashok K Mohapatra Date: 05/02/2019
Member 1 - Dr. Ashok K Mohapatra

K. Senapati Date: 05/02/2019
Member 2 - Dr. Kartikeshwar Senapati

R. Jha Date: 05/02/19
Member 3 - Dr. Rajan Jha

Final approval and acceptance of this thesis is contingent upon the candidate's submission of the final copies of the thesis to HBNI.

I hereby certify that I have read this dissertation prepared under my direction and recommend that it may be accepted as fulfilling the thesis requirement.

Date: 05.02.19

Place: Bhubaneswar

Ritwick Das
Guide

STATEMENT BY AUTHOR

This dissertation has been submitted in partial fulfillment of requirements for an advanced degree at Homi Bhabha National Institute (HBNI) and is deposited in the Library to be made available to borrowers under rules of the HBNI.

Brief quotations from this dissertation are allowable without special permission, provided that accurate acknowledgement of source is made. Requests for permission for extended quotation from or reproduction of this manuscript in whole or in part may be granted by the Competent Authority of HBNI when in his or her judgement the proposed use of the material is in the interests of scholarship. In all other instances, however, permission must be obtained from the author.


Mukesh Kumar Shukla

DECLARATION

I, hereby declare that the investigation presented in the thesis has been carried out by me. The work is original and has not been submitted earlier as a whole or in part for a degree / diploma at this or any other Institution / University.

Mukesh Kumar Shukla
Mukesh Kumar Shukla

List of Publications arising from the thesis

Journals

1. **Mukesh K. Shukla**, and R. Das, “High-Power single-frequency source in the Mid-Infrared using a singly resonant optical parametric oscillator pumped by Yb-fiber laser,” *IEEE Journal of Selected Topics in Quantum Electronics*, vol. 24, pp. 1-6, Sep. 2018.
2. **Mukesh K. Shukla**, P. S. Maji, and R. Das, “Yb-fiber laser pumped high-power, broadly tunable, single-frequency red source based on a singly resonant optical parametric oscillator,” *Optics Letters*, vol. 41, pp. 3033-3036 Jun. 2016.
3. **Mukesh K. Shukla**, S. Kumar, R. Das, “Single-pass, multi-watt second-harmonic-generation in congruent and stoichiometric $LiTaO_3$,” *IEEE Photonics Technology Letters*, vol. 27, pp. 1379-1382, Jul. 2015.

Conferences

1. **Mukesh K. Shukla**, and R. Das, “High Power, tunable, Mid-IR generation with singly resonant optical parametric oscillator,” *2017 Conference on Lasers and Electro-Optics Pacific Rim (CLEO-PR)*, Singapore, Singapore, pp. 1-2, 2017.
2. **Mukesh K. Shukla**, P. S. Maji, and R. Das, “Performance of $\beta - BaB_2O_4$ and BiB_3O_6 as an intra-cavity frequency-doubling element in singly-resonant optical parametric oscillators,” in *13th International Conference on Fiber Optics and Photonics*, OSA Technical Digest (online) (Optical Society of America, 2016), paper W3A.41.
3. **Mukesh K. Shukla**, P. Maji, and R. Das, “On the performance of $\beta - BaB_2O_4$ and BiB_3O_6 as an intra-cavity frequency-doubling element in optical parametric

- oscillators,” in *Frontiers in Optics/Laser Science 2016*, OSA Technical Digest (online) (Optical Society of America, 2016), paper JTh2A.110.
4. **Mukesh K. Shukla**, P. S. Maji, R. Das, “2.6 W, single-frequency, broadly tunable red-source based on Yb-fiber laser”, Conference on Lasers and Electro-Optics (CLEO), OSA Technical Digest (online) (Optical Society of America, 2016), paper JTU5A.58 2016.
 5. **Mukesh K. Shukla**, S. Kumar and R. Das, “Single-pass, multi-watt second-harmonic-generation in congruent and stoichiometric $LiTaO_3$ ”, Photonics Conference (IPC), 2015, Reston, VA, 2015, pp. 63-64.
 6. **Mukesh K. Shukla**, S. Kumar, R. Das, “High-power frequency-doubled Yb-fiber laser”, 12th International Conference on Fibre Optics and Photonics (Photonics) 2014 paper: S5A.29, OSA Technical Digest.
 7. **Mukesh K Shukla**, S. Kumar, R. Das, “High-power, single-frequency, single-pass second-harmonic-generation by optimally focused Yb-fiber laser”, *Advanced Solid State Lasers (ASSL)* 2014 paper: ATh2A.22, OSA Technical Digest.
 8. **Mukesh K Shukla**, S. Kumar, R. Das, “Saturation effects in high-power, continuous-wave, frequency doubling of Yb-fiber laser using MgO:cPPLT”, *Proc. of International Conference on Optics and Opto-electronics (ICOL)* 2014 held at IRDE, Dehradun, India, Mar. 2014.

Others

Journals

1. **Mukesh K. Shukla**, and R. Das, “Tamm-plamon-polaritons and edge-modes in Thue-Morse photonic crystals, under review, 2018.

2. A. Kumari, S. Kumar, **Mukesh K. Shukla**, G. Kumar, P. S. Maji, R. Vijya, and R. Das, “Critical coupling to Tamm-plamons: Structural dependence,” *Journal of Physics D: Applied Physics*, vol. 51, pp. 255103, 2018.
3. **Mukesh K. Shukla**, and R. Das, “Tamm-plasmon-polaritons in 1D photonic quasicrystals,” *Optics Letters*, vol. 43, pp. 362-365, 2018.
4. P. S. Maji, **Mukesh K. Shukla**, and R. Das, “Blood component detection based on miniaturized self-referenced hybrid Tamm-plasmon-polariton sensor,” *Sensors and Actuators B: Chemical*, vol. 255, pp. 729-734, 2018.
5. S. Kumar, **Mukesh K. Shukla**, P. S. Maji, and R. Das, “Self-referenced refractive index sensing with hybrid-Tamm-plasmon-polariton modes in sub-wavelength analyte layers,” *Journal of Physics D: Applied Physics*, vol. 50, pp. 375106, 2017.
6. **Mukesh K. Shukla**, S. Kumar, R. Das, “Single-pass, efficient type-I phase-matched frequency-doubling of high-power ultrashort-pulse Yb-fiber laser using LiB_3O_5 ,” *Applied Physics B: Lasers and Optics*, vol. 122, pp. 114 May 2016.
7. R. Das, **Mukesh K. Shukla**, “Measurement of nonlinear refractive index in open-aperture Z-scan experiments,” *Pramana Journal of Physics*, vol. 83, pp. 985-994, Sep. 2014.

Conferences

1. **Mukesh K. Shukla**, P. S. Maji, and R. Das, “Tamm-plasmon-polaritons in photonic quasi-crystals,” *2017 Conference on Lasers and Electro-Optics Pacific Rim (CLEO-PR)*, Singapore, Singapore, pp. 1-2, 2017.
2. S. Kumar, **Mukesh K. Shukla**, P. S. Maji and R. Das, “Refractive index sensor based on hybrid-Tamm plasmon-polariton and cavity mode,” *2017 Conference on Lasers and Electro-Optics Pacific Rim (CLEO-PR)*, Singapore, Singapore, 2017, pp. 1-2.

3. **Mukesh K. Shukla** and R. Das, "Tamm plasmon polaritons in aperiodic metal deposited Bragg reflectors," in *Frontiers in Optics 2017, OSA Technical Digest* (online) (Optical Society of America, 2017), paper JTU3A.115.
4. S. Kumar, **Mukesh K. Shukla**, and R. Das, "On the Coupling Efficiency of Tamm Plasmon Polaritons," in *Frontiers in Optics 2017, OSA Technical Digest* (online) (Optical Society of America, 2017), paper JW3A.99.
5. **Mukesh K Shukla**, S. Kumar, R. Das, "High-power frequency-doubling of ultra-fast Yb-fiber laser in LBO crystal", *Nonlinear Optics (NLO) 2015 Paper Number: W4A.13*.
6. R. Das, **Mukesh K Shukla**, "Measurement of nonlinear refractive index in open-aperture Z-scan Experiments", *Workshop on Recent Advances in Photonics (WRAP)*, IIT Delhi, Dec. 2013, IEEE Conference Publications.

Mukesh Kumar Shukla
Mukesh Kumar Shukla

To my parents... . . .

ACKNOWLEDGEMENTS

Many thanks to all whose research work inspired me to reach here.

I would like to express my special appreciation and thanks to my advisor *Dr. Ritwick Das*. I thank him for encouraging my research through numerous valuable discussions and for allowing me to grow as a research scientist. Your advice on both research as well as on my career have been priceless. I would especially like to thank him for his patience, thoughtfulness and meticulous editing and guidance.

Its needless to say that the members of school of physical sciences have played important role in my work through their active participation as well as by providing their inputs on my research during reviews. Specially I thank Prof. Bedangadas Mohanty, Dr. Ashok K Mohapatra, and Dr. Kartikeswar Senapati for being my doctoral committee member and for their constructive yearly evaluation of my research work. I would also like to thank Dr. Rajan Jha for being an external member.

I thank my university teachers Prof. Hari Prakash, Prof. Ranjana Prakash and Prof. Naresh Chandra for their motivation to pursue PhD in nonlinear optics.

During the initial days of the lab there were only two people in the lab I and Samir. I thank him for his constructive critical inputs in various official as well as unofficial matters. I thank Awanish for helping me with the CST Studio Suite and making the funny environment in the lab. Later Partha sir joined the lab and I also thank him for sharing his PhD experience. I supervised Rashmi and Anupa in various small projects so I would also like to thank them for being patient enough with me. Special thanks to Rashmi for her help to understand polariton scattering. I would also like to thank Jitendra bhaiya for sharing his expertise in fiber optics. I also thank newly joined members of the lab Abhishek and Shailja for helping me in correcting the drafts. I also thank all my colleagues as well as juniors at NISER for their constant support. Special thanks to 6 A.M. club members.

I thank my friends Manglanand, Amit, Rahul, Aparbal, Manoj, Atul for their scientific and non scientific discussions. Special thanks to Rajesh Bhaiya, Shekhar sir, Santosh, Ankit.

And, most importantly, I want to thank my parents. I am the person I am, because of you. I would also like to thank my sisters Babita and Golu and also my cute nephew Tukku. Special thanks to my Dada, Dadi, Chacha, Chachi and my beloved Manshi, Rimjhim, Tolu. Finally, I thank my wife Shiva for her love and care. Thank you.

Mukesh Kumar Shukla
Mukesh Kumar Shukla

Contents

Synopsis	xxi
List of Figures	xxix
List of Tables	xxxvii
Nomenclature	xxxix
1 Introduction	1
2 Fundamentals of Nonlinear Optics	11
2.1 Historical Background	11
2.2 Nonlinear Optical Physics	12
2.3 Second order nonlinear phenomenon	14
2.4 Wave equation for parametric process	18
2.5 Phase-matching condition	20
2.5.1 Birefringence phase-matching	21
2.5.2 Quasi-phase matching	25
2.6 Optical Parametric oscillator	27
2.7 OPOs and resonance wavelengths	30
2.8 Threshold of SRO and DRO	31
2.9 Tuning characteristics of SRO	33
2.10 Nonlinear crystals for OPO	35

2.11	Cavity design	36
2.11.1	Matrix formulation for beam propagation	36
2.12	Gaussian Beam	38
2.13	Gaussian beam propagation in the OPO ring cavity	42
2.14	Boyd-Kleinman Theory of SHG of Gaussian beam	46
2.15	Stimulated polariton scattering in $LiNbO_3$	48
3	High power Mid-IR optical parametric oscillator	53
3.1	Motivation	53
3.2	Experimental Set-up	57
3.2.1	Laser and beam focusing	57
3.2.2	Cavity	58
3.2.3	Nonlinear Crystal	59
3.3	Results and Discussion	60
3.3.1	Signal and idler tuning	60
3.3.2	Power scaling at $T = 100^\circ C$ and $P_p = 16 W$	61
3.3.3	Signal Spectrum	62
3.3.4	Signal out-coupling in SRO and temperature tuning	64
3.3.5	Signal frequency characteristics	67
3.3.6	Power-stability	68
3.3.7	M^2 and beam profile	70
3.4	Conclusion	70
4	Intra-cavity tunable SHG from Yb-fiber laser pumped PPLN SRO	73
4.1	Introduction	73
4.2	Experimental Set-up	76
4.2.1	Laser and beam focusing	76
4.2.2	Nonlinear crystals	76
4.2.3	Cavity mirrors	77

4.3	Cavity design	78
4.4	Temperature tuning	80
4.5	Single-frequency intra-cavity SHG	80
4.6	Line-width and M^2 measurement	83
4.7	Frequency and Power fluctuations	85
4.8	Conclusion	87
5	Frequency-doubling of high power Yb-fiber laser	89
5.1	Motivation	89
5.2	Experimental Set-up	92
5.3	Phase-matching temperature and tolerance	94
5.4	Phase-matching at higher powers	96
5.5	Optimally focused SHG power-scaling	97
5.5.1	Power stability	101
5.5.2	M^2 and Beam-Profile	103
5.5.3	Single frequency operation and frequency stability	103
5.6	Conclusion	105
6	Summary and future perspective	109
	Bibliography	113
	Appendix A Mirror characterization	125
	Appendix B M^2 Measurement	127

Synopsis

Electromagnetic spectrum, ranging from deep ultra-violet (UV) to far-infrared or terahertz (THz) frequencies, is an important tool for applications in science and technology. After the invention of the lasers in 1960, research activities in the areas of communication, spectroscopy, meteorology, and medicine have undergone an unprecedented growth over the last 50 years [1]. Lasers have played important role in shaping as well as resolving many theoretical aspects of modern physics in form of spectroscopic analysis. Due to the inherent mechanism of coherent generation, most of the lasers are of fixed frequency and a few have limited tunability over a narrow spectral band. In addition, broad tunability along with high optical power remains a challenge in the field of laser development. Some semiconductor diode lasers have exhibited a possibility of achieving high power with broad tunability. However, their tunability is limited up to $2\mu\text{m}$ owing to paucity of material availability and sophisticated electronics. Although, few lasers such as Ti:sapphire, dye-lasers, $\text{Cr}^{2+} : \text{ZnSe}$ and quantum cascaded lasers (QCLs) etc. have shown tunability in some sections of electromagnetic spectrum, it is not appreciable in terms of versatility demanded by spectroscopic and sensing applications [2,3].

Optical parametric oscillators (OPOs) can be utilized to cover unfathomed regions of the electro-magnetic spectrum in comparison to conventional lasers as they did not rely on stimulated emission [4]. Rather, they employ basic principle of optical frequency conversion in nonlinear optics. They can operate in all time scales such as from continuous-wave (CW) to femtosecond and deliver high output powers as well as high beam quality with a fine tunability in the wavelength. In fact, CW operation of OPOs promises the generation

of narrow-linewidth and frequency-stable output with wide and continuously tunable spectral coverage. The working of an OPO depends on the spontaneous parametric fluorescence followed by a difference frequency generation (DFG) process. Spontaneous parametric fluorescence is the process in which spontaneous generation of the signal and idler photons from the pump photon takes place. After satisfying energy and momentum conservation this process leads to spontaneous generation of light at signal (ω_s) and idler (ω_i) frequencies. This is similar to the spontaneous emission of a laser cavity which initiates the laser oscillation. In the DFG process, every photon that is created at difference frequency $\omega_p = \omega_s + \omega_i$, a photon at higher input frequency (ω_s) must be destroyed and a photon at the lower input frequency (ω_i) must be created [5]. When a $\chi^{(2)}$ nonlinear material, placed inside an optical cavity, is pumped by a laser then by the virtue of spontaneous parametric fluorescence and DFG, pump wavelength is converted into two longer wavelength (smaller frequency) photons which are called signal and idler. Such a system is termed as optical parametric oscillator. The optical cavity could be in a varied configuration which includes a linear cavity, ring cavity, bow-tie cavity etc. If the cavity mirrors are highly reflective for only signal then it is called as singly resonant optical parametric oscillator (SRO). On the other hand, if the mirrors resonates more than one wave, the system is termed as doubly or triply resonant optical parametric oscillators. The properties of nonlinear crystal and the beam quality of the pump laser plays an important role for the operation of the OPO. The development of new nonlinear materials and high power spectrally pure laser sources in the late 1980s led to the practical realization of OPOs. In fact, the pulsed OPOs have now become common as their oscillation threshold is very low which played a vital role in their commercialization. But still, the use of CW OPOs remains challenge as they require high power ($> 10 W$) pump source with high spatial as well as temporal beam quality. The very first CW SRO was developed by Yang et al. in the year of 1993 [6] which utilized a birefringent KTP crystal inside a ring cavity with a Nd:YAG laser as pump source. In order to satisfy the momentum conservation condition, the phase-matching between the interacting waves needs to be sat-

isfied. Birefringent phase-matching (BPM) using anisotropic crystals is the most widely employed technique. In BPM, the optic-axis (or axes) of a uniaxial (or biaxial) crystal is rotated with respect to the incident beam in such a way so that the refractive index at the interacting waves satisfies the phase-matching condition. However, BPM has its own limitations e.g. it may not be possible to find a material that has sufficient birefringence to provide phase-matching at the wavelength of interest. Quasi-phase-matching (QPM) technique achieves phase-matching through artificial structuring of the nonlinear material [7]. QPM has revolutionized the area of frequency conversion and guarantees a very high conversion efficiency than the conventional birefringence phase-matching. Nowadays, QPM materials are being utilized frequently in CW OPOs as they have also reduced the required threshold for the oscillation of the CW OPOs. Periodically-poled LiNbO₃ (PPLN) is one of the key QPM material in case of frequency conversion as it has larger effective nonlinear coefficient ($d_{eff} > 25 pm/V$) as well as it covers a long transparency range (330 – 5500 nm) [8].

The present thesis essentially covers three projects where each project is focused on generating high-power, coherent radiation in different spectral bands using a common Yb-fiber laser based pump source. The projects are listed below

1. Demonstration of high power mid-infrared (MIR) optical parametric oscillator
2. Demonstration of intra-cavity frequency-doubled optical parametric oscillator
3. High efficiency, single-pass second-harmonic-generation using stoichiometrically and congruently grown $LiTaO_3$ crystal.

In the first project, a high power CW singly resonant optical parametric oscillator (SRO) which is tunable in the mid-infrared have demonstrated [9]. A 80 mm long PPLN crystal having multiple grating (Λ) from 28.5 to 31 μm in steps of 0.5 μm is pumped with a high power Yb-fiber laser delivering a 40 W maximum output at a wavelength of 1064 nm having a $M^2 < 1.05$. The SRO cavity is a four mirror ring-cavity with two concave ($f = -200 mm$) and two flat mirrors. All the cavity mirrors exhibit high-reflection (HR)

for signal band ($R > 99.3\%$ for $1350\text{ nm} - 1650\text{ nm}$) and high transmission (HT) for pump ($R > 99\%$) as well as idler waves ($R > 90\%$ for $2900\text{ nm} - 4500\text{ nm}$). By focusing the pump beam on the PPLN ($\Lambda = 29\ \mu\text{m}$) and varying the temperature of the crystal-oven, we have generated a tunable radiation from $3761 - 3970\text{ nm}$ yielding a maximum power of 2 W at 3895 nm when the incident pump power is $\approx 16\text{ W}$. Interestingly, we observed that the signal spectrum of SRO is not a single peak rather it is accompanied by several other peaks. LiNbO₃ is Raman active as well as infrared active. We attributed these additional peaks as a result of stimulated polariton scattering. Such polariton modes arise due to strong interaction of intra-cavity signal frequency with Raman as well as IR active modes of LiNbO₃ [10,11]. In order to get single frequency signal operation we have replaced one of the cavity mirrors with a 5% out-coupler ($R > 95\%$ for $1350\text{ nm} - 1650\text{ nm}$), the stimulated polariton modes are suppressed as a consequence of additional cavity losses. Along with a tunable signal extending from 1453 to 1484 nm , we obtained the maximum signal power of $\approx 4\text{ W}$ at 1464 nm at the maximum pump power of $\approx 16\text{ W}$. In addition, we have measured the frequency and power stability of the out-coupled signal and idler beams over long as well as short durations. The improvement in beam quality of idler was discernible when the intra-cavity signal was out-coupled, which is essentially a consequence of reduced thermal load on MgO:PPLN crystal.

In the 2nd project, we have demonstrated an efficient and tunable source generating multi-watt single-frequency red radiation by intra-cavity frequency doubling of the signal in a MgO:PPLN-based SRO [12]. By optimally designing the SRO cavity in a six-mirror configuration, we generate *approx* 276 nm wide tunable idler radiation in mid-infrared with a maximum power of $P_i = 2.05\text{ W}$ at a pump power of $P_p = 14.0\text{ W}$. The resonant signal is frequency doubled using a 10 mm-long BiB_3O_6 (BiBO) crystal ($\theta = 10.6^\circ, \phi = 0.0$) by utilizing the type - 1 ($o + o \rightarrow e$) birefringence phase matching. This resulted in tunability of a red beam from ≈ 753 to 780 nm band with maximum power $P_r \approx 4.0\text{ W}$ recorded at $\lambda_r \approx 756\text{ nm}$. The deployment of a six-mirror SRO ensures single-frequency generation of red across the entire tuning range by inducing additional

losses to Raman modes of $LiNbO_3$ and, thus, inhibiting their oscillation. Using a scanning Fabry–Perot interferometer (FPI), nominal linewidth of the red beam is measured to be $\approx 3\text{ MHz}$ which changes marginally over the entire tuning range. Long-term (over 1 h) peak-to-peak frequency fluctuation of the generated red beam is estimated to be about 3.3 GHz under free-running conditions at $P_p = 16.0\text{ W}$. The generated red beam is delivered in a TEM_{00} mode profile with $M^2 \leq 1.32$ at maximum power in a red beam. This idea is being further extended to generate efficient tunable ultra-violet/violet radiation by optimally designing the cavity.

In addition to the OPO based investigations, we have also carried out single-pass second-harmonic-generation (SHG) of the aforementioned cw Yb-fiber laser using a 1) congruently grown $LiTaO_3$ crystal and 2) stoichiometrically grown $LiTaO_3$ crystal in order to understand the behaviour of differently grown crystals at high pump powers [13]. Using a Yb-fiber laser pump source delivering a single-frequency output of 40 W at 1064 nm, we have generated $\approx 8.5\text{ W}$ and $\approx 14.5\text{ W}$ of single-frequency radiation at 532 nm from 8mol% MgO-doped periodically poled, congruently grown $LiTaO_3$ (MgO:cPPLT) crystal and 0.5mol% MgO-doped periodically poled, stoichiometrically grown $LiTaO_3$ (MgO:sPPLT) crystal respectively. SHG conversion efficiencies in excess of 24% for 5-cm long MgO:cPPLT and $\geq 36\%$ for 3-cm long MgO:sPPLT have been obtained. The impact of thermal dephasing was distinctly discernible in variation of SH power for MgO:cPPLT crystal. However, the manifestations due to thermal loading were found out to be significantly smaller in case of MgO:sPPLT. This lead to saturation of SHG efficiency at pump powers $\geq 20\text{ W}$ for MgO:cPPLT. The long-term peak-to-peak power-fluctuation in case of MgO:sPPLT is recorded to be $\approx 4\%$ for the green beam over a 4-h duration which shows improved performance over MgO:cPPLT output (peak-to-peak power-fluctuation $\approx 11\%$). In addition, the 532-nm radiation exhibited single-frequency characteristics with linewidth of 12 MHz (MgO:cPPLT) and 5 MHz (MgO:sPPLT).

References

1. C. H. Townes, *How the laser happened: Adventures of a Scientist*, Oxford University Press, 1999.
2. F. Tittle, D. Richter, and A. Fried, “Mid-infrared laser applications in spectroscopy,” *Topics Appl. Phys.*, vol. 89, pp. 445–516, 2003.
3. I. T. Sorokina and K. L. Vodopyanov, *Solid-State Mid-Infrared Laser Sources (Topics in Applied Physics)*. New York, NY, USA: Springer, 2003.
4. M. Ebrahim-Zadeh, “Continuous-wave optical parametric oscillators,” in *OSA Handbook of Optics*, vol. 4. Washington, DC, USA: Opt. Soc. Amer., 2010, pp. 1–33.
5. R. W. Boyd. *Nonlinear Optics*, Academic Press, second edition, 2003.
6. S. T. Yang, R. C. Eckardt, and R. L. Byer, “Continuous-wave singly resonant optical parametric oscillator pumped by a single-frequency resonantly doubled Nd:YAG laser,” *Optics Letters*, vol. 18 no. 12, pp. 971–973, 1993.
7. W. P. Risk, T.R. Gosnell, and A. P. Nurmikko, *Compact Blue Green Lasers*, Cambridge University Press, 2003.
8. D. N. Nikogosyan, *Nonlinear optical crystals: A complete survey*. 2005.
9. Mukesh K. Shukla, and R. Das, “High-Power single-frequency source in the Mid-Infrared using a singly resonant optical parametric oscillator pumped by Yb-fiber laser,” *IEEE J. Sel. Top. Quant. Electron.*, vol. 24, pp. 1-6, 2018.
10. A. M. Warriar, R. Li, J. Lin, A. J. Lee, H. M. Pask, and D. J. Spence, “Tunable terahertz generation in the picosecond regime from the stimulated polariton scattering in a *LiNbO3* crystal,” *Opt. Lett.*, vol. 41, no. 18, pp. 4409–4412, 2016.
11. A. Barker and R. Loudon, “Dielectric properties and optical phonons in *LiNbO3*,” *Phys. Rev.*, vol. 158, no. 2, pp. 433–445, 1967.

12. Mukesh K. Shukla, P. S. Maji, and R. Das, "Yb-fiber laser pumped high-power, broadly tunable, single-frequency red source based on a singly resonant optical parametric oscillator," *Opt. Lett.*, vol. 41, pp. 3033-3036, 2016.
13. Mukesh K. Shukla, S. Kumar, R. Das, "Single-pass, multi-watt second-harmonic-generation in congruent and stoichiometric $LiTaO_3$," *IEEE Photon. Technol. Lett.*, vol. 27, pp. 1379-1382, 2015.

List of Figures

1.1	Electromagnetic spectrum ranging from deep ultra-violet (UV), visible, near infrared (NIR), mid infrared (MIR) to far infrared (FIR).	3
1.2	(a) Schematic of the spontaneous parametric fluorescence and (b) optical parametric oscillator.	5
1.3	Schematic of the Research work done in this thesis	8
2.1	Electric field effect on an atom	12
2.2	Schematic of second-order <i>i. e.</i> $\chi^{(2)}$ -processes for various frequency conversions such as (sum frequency generation in which two frequencies added together to generate a third one, (b) second harmonic generation a special case for the sum frequency generation, (c) difference frequency generation and (d) parametric generation <i>i.e.</i> spontaneous generation of signal and idler photons from the pump photon.)	16
2.4	Representation of index ellipsoids in uniaxial (a) positive and (b) negative crystals.	22
2.5	The intersecting ellipsoids for the positive uniaxial crystals shows the phase matching condition at an angle θ which is also known as the angle PM.	22
2.6	Variation of the refractive index of BBO crystal with wavelength as per the Sellmeier eq. (2.33) and (2.34)	24

2.7	Schematic of a QPM process after each coherence length, the direction of polarisation (P_s) is inverted. In the birefringence case, the SHG builds up quadratically with the perfect phase-matching <i>i.e.</i> $\Delta k = 0$ along the propagation direction. In QPM, this build-up is a ‘model’ step process with $\Delta k \neq 0$ as additional π phase-shift is introduced for each coherence length. In case of no phase-matching, the periodic variation of SHG with $\Delta k \neq 0$ is shown.	25
2.8	(a) Singly-resonant OPO where only one frequency <i>i.e.</i> signal resonates inside the cavity, (b) doubly-resonant <i>i.e.</i> both signal and idler resonates (c) the triply resonant OPO where all the three wavelengths resonate.	29
2.9	Variation of signal and Idler wavelengths at different grating periods (Λ_{QPM}) ranging from 28 – 31.5 μm at fixed pump of 1064 nm for MgO doped PPLN crystal.	35
2.10	Cavity designs \Rightarrow (a) two mirror linear cavity, (b) four mirror ring cavity, (c) three mirror V-shaped cavity and (d) four mirror X-shaped cavity.	37
2.11	(a) Propagation of a Gaussian beam along z direction with a initial beam-waist w_0 which will eventually modify to $w(z)$ and the radius of curvature will be $R(z)$. (b) Illustration of the Rayleigh range (z_R) and the confocal parameter (b) of the focused Gaussian beam a spot size of w_0	41
2.12	(a) A simulated temporal profile a Gaussian beam in TEM_{00} mode and (b) beam profile of Yb-fiber laser operating at 1064 nm.	43

- 2.13 Four mirror ring cavity SRO \Rightarrow (a) The center of the crystal is designated as $z = 0$. $M_{1,2,3,4}$ are four mirrors where $M_{1,4}$ has radius of curvature 200 mm and the mirrors $M_{2,3}$ are plane. (b) the pump beam has a beam waist $w_0 = 75\ \mu\text{m}$ and originates from $z = 0$ which results in a signal waist of $w_s = 94\ \mu\text{m}$. The exiting signal comes out of the crystal at Lc_1 with a small divergence. At a distance d_2 , the beam diverges fast and when it reaches M_1 , it tends to focus. The beam focuses to $w(z)$ at the center of the two mirrors ($M_{1,4}$) before diverging again. 45
- 2.15 Boyd-Klienman focusing parameter as a function of focusing. Theoretically, the maximum value of h parameter is 1.068 at $\xi = 2.84$ 48
- 2.16 Crystal diagram of $LiNbO_3$ 49
- 2.17 (a) Dispersion curve of $LiNbO_3$ (Green solid line). The red lines are phase matching angles for the pump beam and the stokes beams. (b) Stokes generation in $LiNbO_3$. (c) Wave-vectors in stokes generation.) 50
- 3.1 Experimental set-up of 4-mirror SRO in ring cavity configuration \Rightarrow HWP: half-wave-plate, PBS: polarizing-beam-splitter, L_1 : diverging lens ($f = -75\text{ mm}$), L_2 : converging lens ($f = 100\text{ mm}$), $M_{1,2}$: concave mirrors with radius of curvature $R = -200\text{mm}$, $M_{3,4,5}$: plane mirrors, M_{oc} : out-coupling mirror, and $D_{1,2,3}$: Thermal detectors. 57
- 3.2 Variation of threshold power (circle) and idler power (square) with idler wavelength when the temperature of the PPLN crystal is varied from $30^\circ\text{C} - 190^\circ\text{C}$ 59
- 3.3 Measurement of the idler power (P_{idler}) and corresponding pump depletion with variation of the pump (P_{pump}). A maximum $P_{idler} \approx 1.6\text{ W}$ was observed at $P_{pump} \approx 10\text{ W}$ and maximum pump depletion was $\approx 50\%$ 61

3.4	(a) Measured spectra of the oscillating signal in the high Q 4-mirror ring SRO. The generated modes (side-bands) are attributed as the stimulated polariton scattering. (b) Signal spectra measured for the low Q-cavity (OC-SRO).	63
3.5	The solid blue line indicates dispersion <i>i.e.</i> wavevector (k) vs frequency plot of $LiNbO_3$ crystal. The black are the phase-matching curves having angles 1.6° , 3.5° , and 12.8° respectively. The red dots indicate the generated polariton modes for corresponding wavelength shifts from signal.	64
3.6	In OC-SRO case (a) the idler power (P_{idler}) and the (b) signal power (P_{signal}) along with their respective wavelengths when the temperature of the crystal-oven is continuously changed from $35^\circ C$ to $190^\circ C$ at $P_{pump} = 16 W$	65
3.7	(a) Measurement of the idler and signal powers along with the variation of the pump power in OC-SRO design at a temperature of $100^\circ C$. (b) Measured pump depletion along with the change in the pump power (P_p).	66
3.8	(a) Wavelength fluctuation measured with wavemeter (HighFinesse). The peak-to-peak fluctuation in the signal beam was $41 GHz$ for $\approx 1 - hour$. And for one minute it is $488 MHz$. (b) FPI measurement confirms the single frequency operation and the measured line-width is $22.5 MHz$	67
3.9	Peak-to-peak fluctuation, which is given in the RMS (root mean square), in the power of the (a) idler in the SRO and (b) signal as well as idler in OC-SRO design for $\approx 1 - hour$	68
3.10	Transverse intensity beam profiles depicting the Gaussian TEM_{00} mode. (a) The idler beam profile in SRO. (b) The signal beam in the OC-SRO. (c) The idler beam in the OC-SRO configuration. The respective M^2 values are shown on the figures.	69

4.1	Schematic of intra-cavity second-harmonic-generation (IC-SHG) in SRO \Rightarrow FI: Faraday isolater; HWP: half wave plate; PBS: polarizing beam splitter; L_1 and L_2 : lenses; $M_{1,2}$: mirrors with radius of curvature (ROC) -200 mm ; $M_{3,4,7}$: plane mirrors; $M_{5,6}$: mirrors with ROC -150 mm . . .	76
4.2	(a) Four-mirror and (b) Six-mirror cavity along with the corresponding Signal spectrum	78
4.3	Variation of generated idler power as a function of idler wavelength when <i>MgO:PPLN</i> crystal temperature was varied from $30 - 185^\circ\text{C}$ (in step of 5°C) at $P_p = 14\text{ W}$ and $\Lambda = 30\mu\text{m}$ in case of (a) BBO-based SRO and (b) BiBO-based SRO.	79
4.4	Variation of generated SH-NIR power as a function of SH-NIR wave- length when <i>MgO:PPLN</i> crystal temperature was varied from $30 - 185^\circ\text{C}$ at $P_p = 14\text{ W}$ and $\Lambda = 30\mu\text{m}$ in case of (a) BBO-based SRO and (b) BIBO-based SRO.	81
4.5	Variation of generated SH-NIR power and corresponding idler power as a function of pump power for (a) BBO-based SRO and (c) BIBO-based SRO. Variation of pump-depletion (in %) as a function of pump power for (b) BBO-based SRO and (d) BIBO-based SRO.	82
4.6	Fabry-Perot interferometer (FPI) spectrum of SH-NIR in (a) BBO-based SRO and (b) BIBO-based SRO. Recorded beam-intensity-profiles with measured M^2 values of SH-NIR beam for (c) BBO-based SRO and (d) BiBO-based SRO.	84
4.7	(a) Frequency and (b) power fluctuations in SH-NIR beam over an hour for BBO-based SRO (red) and BiBO-based SRO (blue) when $P_p = 14\text{ W}$ and $\Lambda = 30\mu\text{m}$	86
5.1	The variation of eye sensitivity function with wavelength as per recom- mendation of CIE 1978.	90

5.2	Single-pass SHG experimental schematics \Rightarrow HWP: half wave plate; PBS: polarizing beam splitter; L_1 and L_2 : lenses; M_1 and M_2 : dichroic mirrors.	92
5.3	(a) Teflon supported crystal oven, (b) Metal sink supported crystal oven.	94
5.4	Measurement of phase matching temperature of (a) MgO:cPPLT and (b) MgO:sPPLT at $P_{pump} = 1 W$	95
5.5	Phase matching at high pump powers. (a) At $P_{pump} = 10, 20, 30 W$ the crystal oven temperature and the generated SH power for MgO:cPPLT crystal. And (b) is the same for MgO:sPPLT.	96
5.6	(a) The change in the crystal oven temperature along with the increase in the pump power for MgO:cPPLT and MgO:sPPLT. (b) Thermal characteristics for MgO:cPPLT and MgO:sPPLT.	98
5.7	The generated SH power or P_{SH} (at $532 nm$) along with the change in pump power for both the crystals indicated with the blue dots. The green dots indicates the experimentally observed conversion efficiency by continuously varying pump power for MgO:cPPLT and MgO:sPPLT crystals.	99
5.8	(a) Plot of the square of the average pump power along with the generated SH power MgO:cPPLT and MgO:sPPLT crystals. (b) In presence of 8 W green power generated from the MgO:sPPLT crystal the variation of the input pump power and the output pump in the MgO:cPPLT crystal.	100
5.9	Stability measurement of the generated SH power in (a) MgO:cPPLT crystal at $P_{pump} \approx 10 W, 20 W$ and $40 W$. Rapid degradation in the SH power at $40W$ is due to the accumulated thermal effects. (b) Peak-to-peak power fluctuation in the MgO:sPPLT at $P_{pump} \approx 40W$ is $\approx 4\%$	102
5.10	Transverse beam profile recorded with CCD camera for (a) MgO:cPPLT crystal and (b) MgO:sPPLT crystal.	103

5.11	Peak-to-peak fluctuation in the wavelength of the generated SH from (a) MgO:cPPLT crystal and (b) MgO:sPPLT crystal.	104
5.12	Fabry-Perot spectra of the (a) MgO:cPPLT and (b) MgO:sPPLT crystal.)	105
5.13	A picture of generated SHG in the lab	107
A.1	Experimental set-up for the OPG of the 1064 <i>nm</i> nanosecond laser and SHG of the generated signal beam.	126
A.2	Transmission of the mirror at different wavelengths	126

List of Tables

1.1	Various commercially available lasers along with their wavelengths of operation	2
1.2	Popular nonlinear materials and their transparency range	4
2.1	Wavelength tunability of an SRO made of 5mol% MgO doped PPLN crystal with a pump of 1064 nm.	33
2.2	Ray matrix diagram of the various optical systems.	39
3.1	Reflectivity and transmission characteristics of mirrors used in the SRO	58
4.1	Comparison chart of both the intra-cavity SROs	86
5.1	Properties of the generated SH power from the MgO:cPPLT and Mg:sPPLT crystals.	106

Nomenclature

Greek Symbols

ξ Boyd-Kleinman focusing parameter

Superscripts

$\chi^{(2)}$ 2nd order nonlinear susceptibility

$\chi^{(3)}$ 3rd order nonlinear susceptibility

Subscripts

d_{eff} Effective nonlinear coefficient

P_{dep} Pump depletion

P_{idler} Idler power

P_{pump} Pump power

P_{SH} SH power

T_{pm} Phase matching temperature

List of Abbreviations

ATE Accumulated Thermal Effects

BBO $\beta - BaB_2O_4$

BiBO	Bi_3BO_6
BPM	Birefringent phase matching
CW	Continuous Wave
DFG	Difference frequency generation
DRO	Doubly-Resonant Optical Parametric Oscillator
HWP	Half Wave Plate
IC-SHG	Intra cavity second harmonic generation
LSDL	Lead salt diode laser
MIR	Mid-infrared
NIR	Near infrared
OC-SRO	Out-coupling SRO
OPG	Optical Parametric Generation
OPO	Optical Parametric Oscillator
PBS	Polarizing Beam Splitter
PM	Phase Matching
PPLN	Periodically poled $LiNbO_3$
PPLT	Periodically poled $LiTaO_3$
QCL	Quantum cascade laser
QPM	Quasi phase matching
SHG	Second harmonic generation

SPS Stimulated Polariton Scattering

SRO Singly-resonant optical parametric oscillator

Chapter 1

Introduction

LASER is the acronym for “*Light Amplification by Stimulated Emission of Radiation*” and one of the greatest inventions of its kind in the 20th century [1]. It was Schawlow and Townes who extended the theoretical concepts of light amplification into a working principle of MASER (microwave amplification of stimulated emission of radiation), which is a microwave version of a laser in the year 1958 [2]. The path from theory to experimental realization of this device was not straightforward. In fact, it took ingredients from many different disciplines for reaching the present level of widespread popularity as well as utility [3]. In 1960, T. Maiman got the first laser radiation from a cylindrical pink ruby crystal by pumping it from a helical flashlamp [4]. The end faces of the crystal were polished with a small hole at one end to observe the red light (694 nm) emission. Subsequently, Ali Javan *et al.* invented the famous *He-Ne* laser in the same year of the Maiman’s discovery and hence, they realized the first continuous wave (CW) laser [5]. These inventions laid the foundation of many new fields in science and instrumentation. Additionally, it played a key role in addressing various theoretical aspects of ground breaking experiments such as *Bose-Einstein-condensation* and the detection of *Gravitational waves* [6, 7].

Laser systems find applications in diverse fields such as micro-machining, spectroscopy, information technology, biophotonics, material processing, medical sciences

Table 1.1 Various commercially available lasers along with their wavelengths of operation

Laser	Wavelength (nm)
<i>Excimer*</i> (<i>F₂, ArF, KrF, XeBr, XeCl, XeF</i>)	157, 193, 248, 282, 308, 358
<i>Argon ion</i>	514.5
<i>Rodamine – 6G</i>	560 – 640
<i>He – Ne</i>	632.8
<i>Ruby</i>	694.3
<i>Laser diodes</i>	375, 404 – 690, 705 – 2000
<i>Ti : sapphire</i>	700 – 1050
<i>Nd³⁺ : YAG</i>	1064
<i>Er – glass</i>	1540
<i>Quantum cascade lasers</i>	3500 – 66000
<i>CO₂</i>	10600

and many more [8, 9]. The range finding was the earliest application of laser. In fact, within four years of the invention of the ruby laser, fully militarised active-range finders were manufactured using pulsed ruby lasers. This discovery of ruby laser triggered an intensive search for other material suitable for lasing. In the decade of 1970 and 1980, many lasers were developed based on alexandrite, titanium-doped sapphire and chromium doped fluoride crystals. Diode lasers capable of operating in CW mode also emerged in this decade. The most promising tunable laser was *Ti:sapphire* laser which was discovered by P. F Moulton in 1982. The main advantage of this was its tunability, which is from 680 nm to 980 nm and also it can work in CW as well as in femtosecond format using the mode-locking techniques. Nowadays, there are many laser systems operating in various spectral bands. Table 1.1 comprises some of the popular lasers which are commercially available. One of the key aspects of the present day laser technology is that the pulses can be generated on a time-scale as low as $< 10^{-16}$ s and absolute frequencies as accurate as 10^{-15} s⁻¹ could be measured.

Although the laser systems are in use for more than 50 years now, there are bands in the electromagnetic spectrum (Fig.1.1) where their presence is negligible. This is primarily because of the unavailability of the suitable medium which exhibits desirable

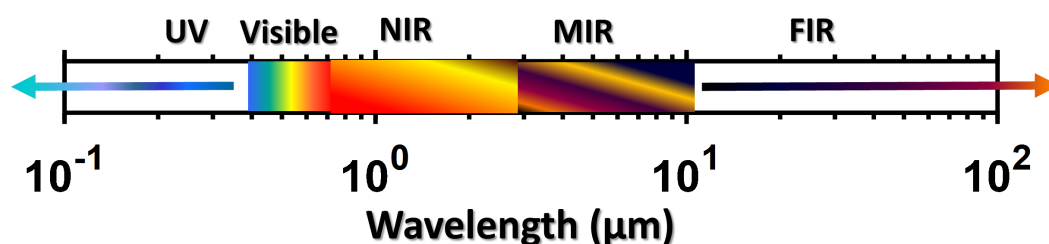


Figure 1.1 Electromagnetic spectrum ranging from deep ultra-violet (UV), visible, near infrared (NIR), mid infrared (MIR) to far infrared (FIR).

gain spectrum in those bands. Wavelength (or frequency) tunability in laser wavelength is also one prominent issue which hinders their utilization in numerous fields. Although few lasers such as Ti:sapphire, dye-lasers, and quantum cascaded lasers (QCLs) etc. have exhibited coarse as well as fine wavelength tunability in a few regions of the optical spectrum, it is not sufficient for various applications in spectroscopy and microscopy.

Around a year after the discovery of laser, Franken *et al.* has shown the second harmonic generation (SHG) of the ruby laser operating at 694.3 nm and thereby, generating half wavelength at 347.2 nm [10]. This demonstrated the existence of 2^{nd} order nonlinear optical coefficients in the ruby crystal and a new field in optics emerged which laterally known as nonlinear optics. Although, it was J. Kerr and latter Raman *et al.* who observed the nonlinear optical phenomenon years before this discovery [11–14]. Schrodinger’s work is considered to be first description of nonlinear optical phenomenon in 1942 [15, 16]. In a short span of time, more nonlinear optical processes such as optical parametric generation and oscillation were demonstrated, which has the capability to generate tunable radiations with high power. These processes essentially depend on the 2^{nd} order nonlinear polarization ($\chi^{(2)}$) which are also referred as $\chi^{(2)}$ -effects [17]. The materials which do not possess a center of inversion symmetry exhibits the $\chi^{(2)}$ based nonlinear optical process. In Table 1.2 some of the popular $\chi^{(2)}$ materials are listed along with their transparency range [18]. Their high nonlinear coefficient and the possibility to achieve-phase matching is key to deploy them in parametric devices [19]. Continuous wavelength tunability can be achieved from the parametric generation process over a broad spectrum

Table 1.2 Popular nonlinear materials and their transparency range

Material	Transparency (nm)
KBBF ($KBe_2BO_3F_2$)	147 - 3500
BBO ($\beta - BaB_2O_4$)	185 - 2600
BiBO (BiB_3O_6)	286 - 2500
$LiTaO_3$	280 - 5500
$LiNbO_3$	330 - 5500
$GaAs$	997 - 17000

by varying the phase-matching condition in the nonlinear medium. The first tunable optical parametric oscillator (OPO) was reported by Giordmaine and Miller in the year 1965 [20]. They observed a wavelength tunable optical pulses from 970 nm to 1150 nm in a lithium metaniobate crystal by pumping it from a giant pulse $Nd^{3+} : CaWO_4$ laser delivering frequency doubled output wavelength at 529 nm. Since then, the OPOs have seen unprecedented growth in the pulsed regime as they can cover unfathomed regions of the electromagnetic spectrum in comparison to conventional lasers. The main advantage of OPOs is that they do not rely on stimulated emission between two ‘real’ energy levels rather, they employ the basic principle of nonlinear optics. This facilitates the generation of high-power coherent as well as tunable radiation in a desired spectral band. They can operate in all time scales such as from CW to femtosecond and deliver high output powers as well as high beam quality with a fine wavelength tunability across any spectrum [21]. In fact, CW operation of OPOs promises the generation of narrow-linewidth and frequency-stable output with wide and continuously tunable spectral coverage. This has numerous applications such as high-resolution spectroscopy, development of modern generation quantum information systems, and biophotonic applications such as confocal microscopy, flow cytometry, selective fluorophore activation, and excitation [22–25, 9]. Specifically, the tunable MIR OPOs have shown parts per trillion trace-gas detection with the help of chemical spectroscopic techniques [26, 27]. Some of the techniques such as molecular beam spectroscopy and trace-gas detection require high average power which

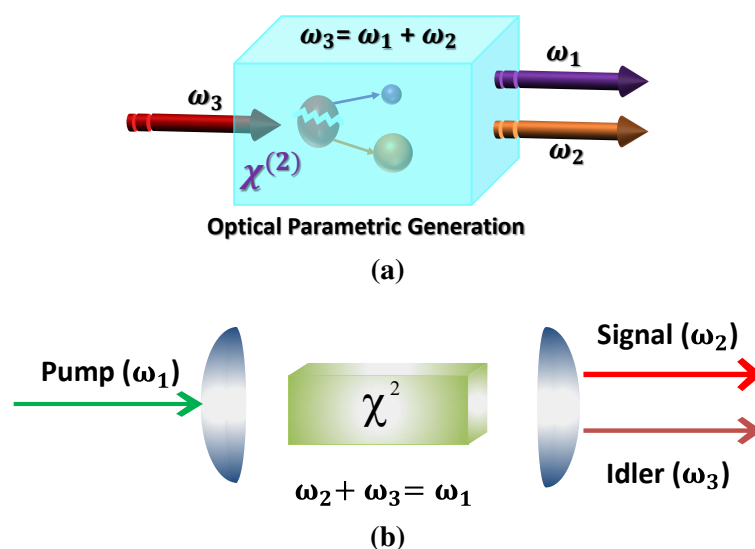


Figure 1.2 (a) Schematic of the spontaneous parametric fluorescence and (b) optical parametric oscillator.

can not be satisfied with the conventional laser sources and thus, the OPOs fill-in this gap with high-power continuously tunable operation.

The working of an OPO is governed by the spontaneous parametric fluorescence followed by a sustainable difference frequency generation process (DFG). Spontaneous parametric fluorescence is a process in which spontaneous generation of the two photons, namely signal, and idler, from the pump photon takes place. After satisfying the energy and momentum conservation, this process leads to the spontaneous generation of light at signal (ω_s) and idler (ω_i) frequencies. This is similar to the spontaneous emission of a laser cavity which initiates the laser oscillation. In the DFG process, every photon that is created at difference frequency $\omega_3 = \omega_1 - \omega_2$, a photon at higher input frequency (ω_1) must be destroyed and a photon at the lower input frequency (ω_2) must be created which is illustrated in the Figure 1.2(a) [17]. This process leads to the amplification of the lower-frequency field (signal) and hence, it is also known as the optical parametric amplification. The gain resulted from this field can be utilized to construct a device which is known as the optical parametric oscillator. When a nonlinear material with non-zero $\chi^{(2)}$ value is placed inside an optical cavity and a high-power pump laser is incident then the newly generated frequencies are forced to oscillate in the cavity. This process is

termed as optical parametric oscillator. An illustration of optical parametric oscillation is given in the Figure 1.2(b). The OPO cavities are classified into two types (i) standing-wave cavity and (ii) a ring cavity. Standing wave cavity can be a linear two mirror cavity or a four-mirror X-cavity whereas a ring cavity exhibits a circulation of beam using 3 or more mirrors. In case of OPOs, ring-cavity is a preferred configuration due to the fact that the gain in a conventional DFG process is in the forward direction. Based on the resonant frequencies, OPOs could be categorized as singly-resonant, doubly-resonant and triply-resonant or alternately pump-enhanced. If the cavity mirrors are highly-reflective for only signal wavelength then it is called as singly-resonant optical parametric oscillator (SRO) . If the cavity mirrors are highly reflective for both *i.e.* signal and idler beams then this configuration is termed as doubly-resonant optical parametric oscillator (DRO) . Pump enhanced OPO is a special case of DRO. At an early stage of OPO development, the DRO based configurations were most popular as DROs require almost $100\times$ less threshold than SROs. However, resonating both wavelengths also increases the complexity of the system. SROs are advantageous in this respect as the restrictions on the cavity tolerances are not as severe as that of the DROs.

The properties of nonlinear crystal and the beam quality, as well as the output of the pump laser, plays an important role for the operation of the OPO. Especially the poor quality of the nonlinear crystals adversely affects the conversion efficiency of the process. The development of new nonlinear material and high-power spectrally pure laser sources in the late 1980s led to the practical realization of OPOs. In fact, the pulsed OPOs have now become common as their oscillation threshold could easily achieve in a pulsed configuration which played a vital role in their commercialization. On the contrary, the realization of CW OPOs still remains a challenge as they require high power (> 5 W) pump source with very high spatial as well as temporal beam quality. The very first CW SRO was developed by Yang *et al.* in the year of 1993 [28]. They had utilized a birefringent KTP crystal inside the cavity which was pumped by a Nd:YAG laser. With respect to phase-matching, birefringent phase matching (BPM) is a well-known technique

where the angle of birefringent crystals are angle-tuned for realizing matching of phase-velocities of interacting beams. However, BPM has its own limitations *e.g.* it may not be possible to find a material that has sufficient birefringence to provide phase-matching at the spectral band of interest. Quasi phase matching (QPM) technique, on the other hand, achieves phase-matching through the artificial structuring of the nonlinear material. QPM has revolutionized the area of frequency conversion and guarantees a very high conversion efficiency than the conventional BPM. Present generation QPM materials are fundamental to the realization of CW OPOs as they substantially reduce the threshold pump power for sustaining the oscillation in CW OPOs. Periodically poled $LiNbO_3$ (PPLN) is one of the key QPM material in case of frequency conversion as it has larger effective nonlinear coefficient ($d_{eff} > 17 \text{ pm/V}$) as well as it covers a long transparency range (330 – 5500 nm) [19]. In order to improve the photo-refractive features, PPLN is often doped with the MgO. Belonging to the same family of nonlinear materials, $LiTaO_3$ (doped with MgO) is a preferred choice to generate frequencies in the blue-green and ultra-violet region of the spectrum.

The present thesis discusses a variety of practical $\chi^{(2)}$ based devices using one kind of pump laser source. The discussion is primarily focused on different configurations for generating tunable radiation extending from visible to mid-infrared (MIR) is being generated. Outline of the present thesis is described in the Fig. 1.3. The entire research work is located in the CW regime with a *Yb:fiber* laser based pump source. The maximum output provided by the pump laser is 40 W at an operating wavelength of 1064 nm. In order to generate high power near-infrared (NIR) and MIR radiation, the thesis describes an SRO made up to MgO doped PPLN crystal. It is well-known that $LiNbO_3$ shows infrared-active modes as well as Raman-active modes and consequently, it could support polariton scattering. We observed the stimulated-polariton-scattering (SPS) of the signal beam in the SRO generating MIR frequencies. Further, in order to obtain single-frequency radiation, we have out-coupled the generated multimode signal by replacing one of the cavity mirrors with an out-coupling mirror. For the generation of visible/NIR tunable

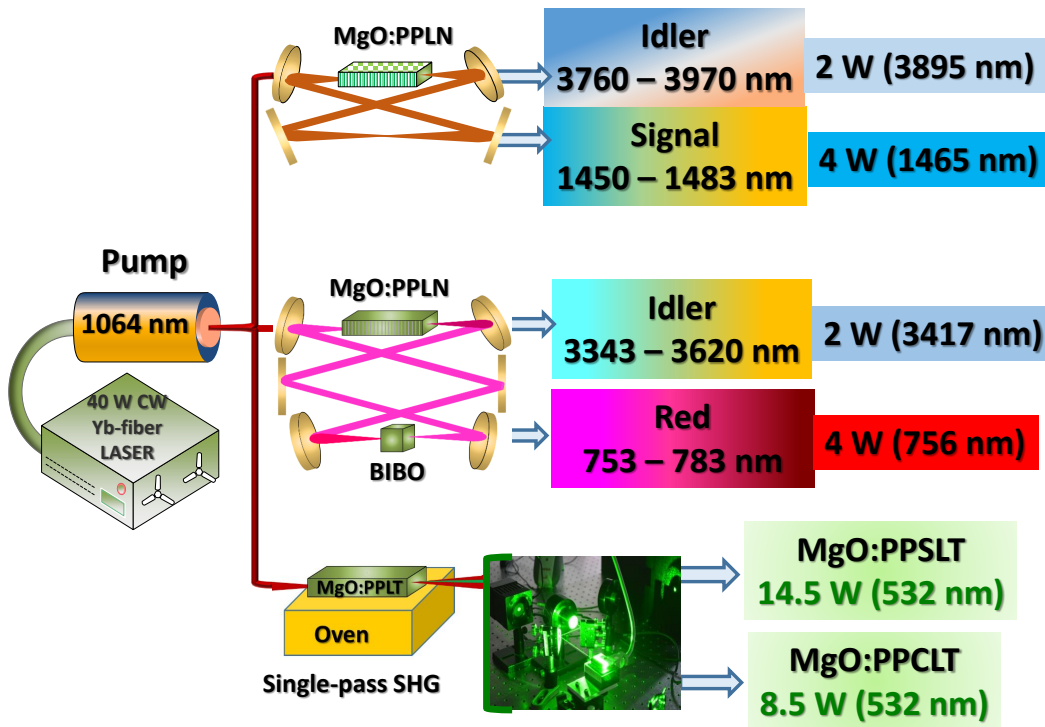


Figure 1.3 Schematic of the Research work done in this thesis

radiation the signal of the SRO in six-mirror ring-cavity configuration is executed through intra-cavity frequency-doubling in Bi_3BO_6 (BIBO) crystal. In an investigation, we have performed the SHG of the pump (*Yb : fiber*) laser with two variants of periodically poled $LiTaO_3$ (PPLT) crystal for realising a reliable and efficient source in the green band of visible spectrum ($\lambda = 532 \text{ nm}$). In this study, one crystal is chosen to be stoichiometrically grown PPLT crystal whereas the other is a congruently-grown variant of PPLT crystal. The present thesis is divided into six chapters.

In chapter 2, we have introduced and discussed the fundamentals of a few nonlinear optical interactions, namely SHG, DFG, and OPOs. The necessity of the phase-matching (PM) condition in nonlinear optics along with two popular PM schemes *i.e.* birefringence PM and quasi-PM is discussed. Ray matrix design of some optical elements and the Gaussian beam propagation is also illustrated in this chapter. The solution of coupled-wave equations (with plane-wave approximation) in case of OPOs along with various possible cavity designs are also discussed. Further, by utilizing the Gaussian beam

propagation in a stable SRO cavity for the MgO doped PPLN crystal is presented. In the end, a brief description of SPS in $LiNbO_3$ is discussed with an aim to generate coherent terahertz radiation.

A tunable high power SRO operating in MIR is presented in chapter 3 [29]. The generated signal contained side-bands at high power regime which has been attributed to stimulated Raman as well as polariton scattering in $LiNbO_3$ crystal. By deploying the concept of signal out-coupling, we restrict the generation of the signal in single-mode which have shown to reasonably extended tunability. The recorded power and frequency stability of the generated signal, as well as the idler, is presented to establish the viability of the scheme as a practical MIR source. The spatial and temporal characteristics of the generated MIR beam is discussed.

Chapter 4 presents a tunable frequency-doubled SRO operating in the visible as well as in MIR [30]. The configuration is a six-mirror ring-cavity MgO-doped PPLN based SRO. The frequency doubling of the resonant signal is executed through two different nonlinear crystals, namely BIBO and BBO ($\beta - BaB_2O_4$), in two different experimental configurations. A high-power, frequency-tunable visible radiation is achieved from the SRO which has significant importance in the field of medical sciences as well as in quantum optics. Various spatial, as well as temporal beam characteristics, are being presented with an aim to understand the underlying physical mechanism at high pump powers. A comparison of both the tunable visible/NIR radiation obtained from the two different experimental configurations is presented in detail.

In the penultimate chapter, we present a detailed comparison between two high-power single-frequency green sources operating at a fixed wavelength of 532 nm [31]. Both the sources are pumped by a $Yb - fiber$ laser operating at 1064 nm. We deploy two variants of crystals, namely congruently-grown $LiTaO_3$ and stoichiometrically-grown $LiTaO_3$, in a periodically-poled arrangement. An efficiency, in excess of 36%, in a single-pass configuration is obtained in the stoichiometric variant of PPLT crystal which is maximum conversion efficiency reported till date. This chapter also focuses on the

thermal manifestation in the $LiTaO_3$ crystals at high pump powers and it was observed that the thermal dephasing is a dominant factor in the congruent variant. A variety of measurements is presented for appreciating the role of physical properties of the crystal as well as underlying physical mechanisms governing the generation of single-frequency green radiation. Such high-power, coherent sources are immensely important for the pumping of the *Ti:sapphire* lasers and various NIR/visible OPOs.

Finally, we have summarised our work in chapter 6 along with the future prospects of the presented thesis.

Chapter 2

Fundamentals of Nonlinear Optics

2.1 Historical Background

The first experiment which led the foundation of nonlinear optics was done by J. Kerr in 1875 [11, 12]. He observed a change in the refractive index in some organic liquids as well as glasses in presence of strong DC electric field. In this experiment, he collimated the light from sun and dispersed it through a prism. This was followed by passing the beam through a sample which was placed between a pair of crossed polarizers. In order to observe the impact of optical nonlinearity, a strong transverse electric field was applied to the sample. He found that the transmitted intensity from the sample is a quadratic function of the applied voltage [32]. Later, this phenomena is known as Kerr effect and after the invention of Laser in 1960, it is replaced as Optical Kerr Effect or intensity dependent refractive index which is often written as

$$n = n_0 + n_2 I \quad (2.1)$$

where n_0 is the linear refractive index, I is the intensity and n_2 is the Kerr coefficient.

Using a laser, the first nonlinear optical phenomenon was reported by Franken *et al.* in 1961. Here, they observed SHG in a quartz crystal by pumping it from a frequency

doubled $Nd^{3+} : CaWO_4$ laser. The nonlinear crystal for this study was ferroelectric $LiNbO_3$ which is single domain sample grown from Czochralski technique [4, 10]. This experiment became the benchmark for the field and motivated many scholars to study various nonlinear optical phenomena.

2.2 Nonlinear Optical Physics

The interaction of electromagnetic wave and matter come under the umbrella of optical physics. The earlier concept in optics involve reflection and refraction which can be explained by understanding of the electric dipole radiation with a knowledge of linear optics. The induced polarization has a linear dependence on the applied electric field which is written as

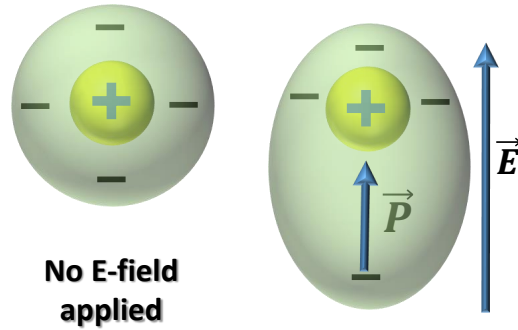


Figure 2.1 Electric field effect on an atom

$$\tilde{\mathbf{P}}(t) = \epsilon_0 \chi^{(1)} \tilde{\mathbf{E}}(t) \quad (2.2)$$

where \mathbf{P} and \mathbf{E} are the polarization and electric field vectors, respectively, ϵ_0 is relative permittivity of free space and $\chi^{(1)}$ is called as linear susceptibility [17].

In general, the frequency of the optical radiation depend on χ which is a tensor. This relation holds only in the linear regime *i. e.* the linear optics in which the dipole oscillation and the emitted radiation from the dipole are at the same frequency as the input electric field. However, when the strength of the electric field is high enough with respect to the inter-atomic field, the dipole displacement shows nonlinear behavior with the electric field. This is where the study and observation of nonlinear optical phenomenon comes into play which could be categorised in domain of a strong field optics.

Let us understand this with a simple model as described by Risk *et al.* [33]. Suppose the atoms of the crystal is made of positively charged nucleus and negatively charged electron whose centres coincide with each other as shown in the Fig. 2.1. This is an equilibrium condition with no net polarization. When an electric field at a certain frequency is incident on this atom, the electron cloud is distorted. Hence, a spatial separation between the +ve and -ve centres arise which corresponds to the induced polarization. Since the electric field of light wave is time varying, it will induce an oscillating polarization. If the induced polarization (\mathbf{P}) and the electric field (\mathbf{E}) do not bear a linear relationship then the induced electron cloud is distorted. This distortion results in additional frequencies in polarisation which gives rise to the possibility of generating additional frequencies along with modifying the refractive index [33]. Here, the induced polarization could be expressed using power series expansion as [17]

$$\mathbf{P} = \underbrace{\epsilon_0\chi^{(1)}\mathbf{E}} + \underbrace{\epsilon_0\chi^{(2)}\mathbf{E}^2} + \underbrace{\epsilon_0\chi^{(3)}\mathbf{E}^3} + \dots + \underbrace{\epsilon_0\chi^{(m)}\mathbf{E}^m} \quad (2.3)$$

$$\mathbf{P} = \mathbf{P}^{(1)} + \mathbf{P}^{(2)} + \mathbf{P}^{(3)} + \dots + \mathbf{P}^{(m)} \quad (2.4)$$

$$\mathbf{P} = \mathbf{P}^L + \mathbf{P}^{NL} \quad (2.5)$$

where $\chi^{(2)}, \chi^{(3)}, \dots, \chi^{(m)}$ are higher order nonlinear susceptibilities with a rank of 3, 4, ..., $(m+1)$ and $\mathbf{P}^{(1)} = \mathbf{P}^L$, $\mathbf{P}^{NL} = \mathbf{P}^{(2)} + \mathbf{P}^{(3)} + \dots + \mathbf{P}^{(m)}$ stands for the linear (Eq. (2.2)) and nonlinear polarizations respectively. In this equation, there are tensor products between the nonlinear susceptibility and the electric fields which suggests that if there are multiple incident waves with different frequencies, wavevectors, and polarization directions then all such waves will superpose to generate different frequencies depending on the product of susceptibility tensor and incident field vector. The frequency generation phenomenon will be discussed in the upcoming sections. In general, $\chi^{(2)}$ and $\chi^{(3)}$ are found in the order of 10^{-12} m/V and $10^{-24} \text{ m}^2/\text{V}^2$ whereas $\chi^{(1)}$ is of the order of unity [17]. To observe the effect of $\chi^{(2)}$ and $\chi^{(3)}$, one needs coherent excitation source which

can easily be accessed by the lasers. The invention in 1960 led the foundation of nonlinear optics [4]. In fact, the first phenomenon of nonlinear optics known as second harmonic generation in Quartz crystal was shown from first working Ruby laser in 1961 [10]. The media exhibiting non-zero second-order susceptibility exhibit a missing centre for inversion symmetry whereas crystalline media displaying third-order ($\chi^{(3)}$) susceptibility could be centro-symmetric as well as non-centro-symmetric. In order to understand the impact of missing centre for inversion symmetry in medium possessing $\chi^{(2)}$, let us suppose that the media possesses a centre for inversion symmetry. Inversion symmetry implies that changing the sign of the electric field would reverse the sign of associated polarization *i.e.* if we consider only the coefficient $\chi^{(2)}$ for understanding the nonlinear optical effects then the inverted polarization could be written as

$$-\mathbf{P}^{NL} = \epsilon_0 \chi^{(2)} (-\mathbf{E})^2 \quad (2.6)$$

$$\Rightarrow -\mathbf{P}^{NL} = \epsilon_0 \chi^{(2)} \mathbf{E}^2 \quad (2.7)$$

$$\Rightarrow -\mathbf{P}^{NL} = \mathbf{P}^{NL} \quad (2.8)$$

which is only possible if $\chi^{(2)} = 0$. Thus, $\chi^{(2)}$ related manifestations are not possible in materials possessing centre for inversion symmetry.

2.3 Second order nonlinear phenomenon

Second order nonlinear process is a phenomenon which originates with $\chi^{(2)}$. The related polarization can be written as

$$\mathbf{P}^{NL} = \epsilon_0 \chi^{(2)} \mathbf{E}^2 \quad (2.9)$$

where $\chi^{(2)}$ is often represented as $\chi_{ijk}^{(2)}$ which depicts a rank-3 tensor. The indices i , j and k are cartesian component of electric field and represent the direction of polarization. As discussed above, certain component of $\chi^{(2)}$ -tensor is non-zero only for crystals without a

center of inversion symmetry. Let us consider a electric field with two distinct frequency components ω_1 and ω_2 can be described as

$$\mathbf{E}(t) = \mathbf{E}_1(t)e^{-i\omega_1 t} + \mathbf{E}_2(t)e^{-i\omega_2 t} + c.c. \quad (2.10)$$

where c.c. is referred to as the complex conjugate. The nonlinear polarization can be written as

$$\begin{aligned} \mathbf{P}^{NL}(t) &= \sum_{n=1,2} P(\omega_n)e^{-i\omega_n t} \\ &= \epsilon_0 \chi^{(2)} \left[\underbrace{E_1^2 e^{-i(2\omega_1)t}}_{\text{SHG}} + \underbrace{E_2^2 e^{-i(2\omega_2)t}}_{\text{SHG}} \right. \\ &\quad + \underbrace{2E_1 E_2 e^{-i(\omega_1 + \omega_2)t}}_{\text{SFG}} \\ &\quad + \underbrace{2E_1 E_2^* e^{-i(\omega_1 - \omega_2)t}}_{\text{DFG}} + c.c. \left. \right] \\ &\quad + 2\epsilon_0 \chi^{(2)} \underbrace{[E_1 E_1^* + E_2 E_2^*]}_{\text{OR}} \end{aligned} \quad (2.11)$$

The terms in this process represents various nonlinear processes such as the first two terms are second harmonic generation (SHG), third and fourth terms are sum frequency generation (SFG) and difference frequency generation (DFG) respectively. The last term is the optical rectification (OR). The complex conjugates does not add any extra process and consequently, we have ignored them in the present discussion. All these processes can be separately labeled as follows

$$\text{Second Harmonic Generation (SHG) : } P(2\omega_1) = \epsilon_0 \chi^{(2)} E_1^2 \quad (2.12)$$

$$\text{Second Harmonic Generation (SHG) : } P(2\omega_2) = \epsilon_0 \chi^{(2)} E_2^2 \quad (2.13)$$

$$\text{Sum Frequency Generation (SFG) : } P(\omega_1 + \omega_2) = 2\epsilon_0 \chi^{(2)} E_1 E_2 \quad (2.14)$$

$$\text{Difference Frequency Generation (DFG) : } P(\omega_1 - \omega_2) = 2\epsilon_0 \chi^{(2)} E_1 E_2^* \quad (2.15)$$

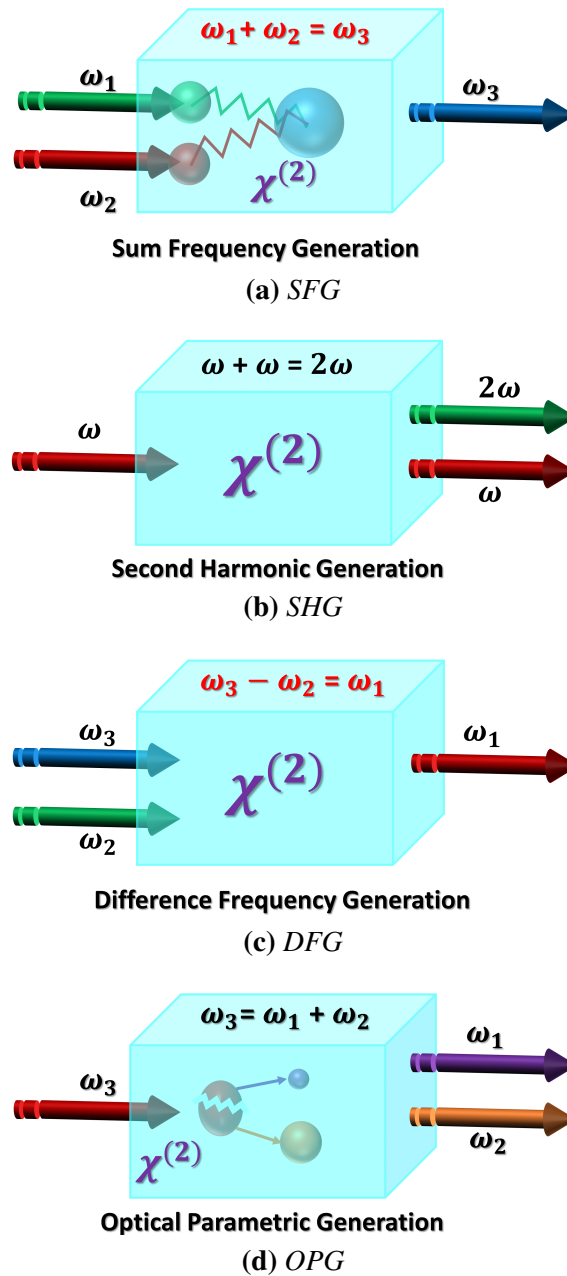


Figure 2.2 Schematic of second-order i. e. $\chi^{(2)}$ -processes for various frequency conversions such as (sum frequency generation in which two frequencies added together to generate a third one, (b) second harmonic generation a special case for the sum frequency generation, (c) difference frequency generation and (d) parametric generation i.e. spontaneous generation of signal and idler photons from the pump photon.)

A pictorial representation depicting various $\chi^{(2)}$ -based nonlinear optical processes are given in the Fig. 2.2. In sum-frequency generation (SFG) two electromagnetic (*em*) waves with frequencies ω_1 and ω_2 are added thereby, generating a new wave having a frequency $\omega_3 = \omega_1 + \omega_2$. Second harmonic generation is a special case of SFG where the waves at identical frequencies ($\omega_1 = \omega_2 = \omega$) are mixed together and generate a new waves $\omega_3 = 2\omega$. In the case of difference frequency generation (DFG) the two *em* waves having frequencies ω_1 and ω_2 are mixed in such a way that they gives rise to a difference-frequency wave such that $\omega_3 = \omega_1 - \omega_2$. In all these processes, the energy and momentum (assuming the processes have quantum mechanical origin) are conserved through phase-matching-condition which will be discussed later in this chapter.

In nonlinear optics, the use of nonlinear coefficient d is more common rather than $\chi^{(2)}$ and this d -tensor is defined as

$$d_{ijk} = \frac{1}{2}\chi_{ijk}^{(2)} \quad (2.16)$$

Under Kleinman symmetry, the the last two indices of d-tensor *i.e.* j, k would be necessarily symmetric. Then, the elements jk could be contracted as

$$\begin{array}{cccccc} jk : & 11 & 22 & 33 & 23, 32 & 31, 13 & 12, 21 \\ l : & 1 & 2 & 3 & 4 & 5 & 6 \end{array} \quad (2.17)$$

Hence the d -tensor, in its contracted form, could be expressed as a 3×6 matrix. Now, if one applies the Klienman symmetry explicitly *i.e.* the indices of d_{ijk} could be freely permuted then d_{il} has only 10 independent elements. Therefore, the d -tensor appear to be

$$d_{il} = \begin{bmatrix} d_{11} & d_{12} & d_{13} & d_{14} & d_{15} & d_{16} \\ d_{21} & d_{22} & d_{23} & d_{24} & d_{25} & d_{26} \\ d_{31} & d_{32} & d_{33} & d_{34} & d_{35} & d_{36} \end{bmatrix} = \begin{bmatrix} d_{11} & d_{12} & d_{13} & d_{14} & d_{15} & d_{16} \\ \mathbf{d}_{16} & d_{22} & d_{23} & d_{24} & \mathbf{d}_{14} & \mathbf{d}_{12} \\ \mathbf{d}_{15} & \mathbf{d}_{24} & d_{33} & \mathbf{d}_{23} & \mathbf{d}_{13} & \mathbf{d}_{14} \end{bmatrix}$$

with this the nonlinear polarization for sum frequency generation *i.e.* $\omega_3 = \omega_1 + \omega_2$ is represented by

$$\begin{bmatrix} P_x(\omega_3) \\ P_y(\omega_3) \\ P_z(\omega_3) \end{bmatrix} = 4\epsilon_0 \begin{bmatrix} d_{11} & d_{12} & d_{13} & d_{14} & d_{15} & d_{16} \\ d_{16} & d_{22} & d_{23} & d_{24} & d_{14} & d_{12} \\ d_{15} & d_{24} & d_{33} & d_{23} & d_{13} & d_{14} \end{bmatrix} \begin{bmatrix} E_x(\omega_1)E_x(\omega_2) \\ E_y(\omega_1)E_y(\omega_2) \\ E_z(\omega_1)E_z(\omega_2) \\ E_y(\omega_1)E_z(\omega_2) + E_z(\omega_1)E_y(\omega_2) \\ E_x(\omega_1)E_z(\omega_2) + E_z(\omega_1)E_x(\omega_2) \\ E_x(\omega_1)E_y(\omega_2) + E_y(\omega_1)E_x(\omega_2) \end{bmatrix} \quad (2.18)$$

2.4 Wave equation for parametric process

The Maxwell's equations could be reduced to the wave equation for a nonlinear media having no free currents and charges as follows [34]

$$\nabla^2 \mathbf{E} = \mu_0 \epsilon_0 \frac{\partial^2 \mathbf{E}}{\partial t^2} + \mu_0 \frac{\partial^2 \mathbf{P}^{NL}}{\partial t^2} \quad (2.19)$$

here, μ_0 is permeability of vacuum, \mathbf{E} and \mathbf{P}^{NL} as described earlier. Further, an electric field \mathbf{E} propagating along z -direction having frequency ω_j where $j = 1, 2, 3$ represents the three interacting fields (pump, signal and idler) could be expressed as

$$\mathbf{E}_j(z, t) = \mathbf{E}(z, \omega_j) e^{i(k_j z - \omega_j t)} + c.c. \quad (2.20)$$

where $k_j = \frac{n_j(\omega_j)\omega}{c}$ is the magnitude of the wavevector with $n_j(\omega_j)$ as the refractive indices of the medium at respective frequencies and c being the speed of light. The medium refractive index is defined as

$$n = n(\omega_j) = \sqrt{\frac{\epsilon(\omega_j)}{\epsilon_0}} \quad (2.21)$$

where $\varepsilon(\omega_j)$ is the permittivity of the medium at the frequency ω_j . Similarly as per the (2.20) the corresponding polarization can be written as

$$\mathbf{P}_j(z, t) = \mathbf{P}(z, \omega_j) e^{-i(k_j z - \omega_j t)} \quad (2.22)$$

Now substituting the values of Eq. (2.20) and Eq. (2.21) in Eq. (2.19) and assuming (i) the interacting waves are plane waves and (ii) *slowly varying envelop approximation* (SVEA) is valid, we simplify the wave equations in the following coupled-wave equations,

$$\frac{\partial E_1}{\partial z} = i \frac{\omega_1^2}{k_1 c^2} d_{eff} E_3 E_2^* e^{i\Delta k z} \quad (2.23)$$

$$\frac{\partial E_2}{\partial z} = i \frac{\omega_2^2}{k_2 c^2} d_{eff} E_3 E_1^* e^{i\Delta k z} \quad (2.24)$$

$$\frac{\partial E_3}{\partial z} = i \frac{\omega_3^2}{k_3 c^2} d_{eff} E_1 E_2 e^{-i\Delta k z} \quad (2.25)$$

Here, $E_{3,2,1}$ are the interacting electric fields which can also be labeled as pump (p), signal (s) and idler (i) respectively for the case of optical parametric amplification/oscillation. All the interacting waves obey the energy and momentum conservation conditions. Accordingly the energy conservation is given by $\omega_3 = \omega_1 + \omega_2$. The phase-mismatch term is defined as $\Delta k = k_3 - k_2 - k_1$. In order to get the maximum conversion efficiency, the phase-mismatch should be $\Delta k = 0$. This can be achieved through various phase-matching methods which will be discussed later in this chapter.

The SHG process is a special case of the coupled equations. (2.23), (2.24) and (2.25) could be modelled for ‘two’ interacting waves such as $\omega_1 = \omega_2 = \omega$ and $\omega_3 = 2\omega$. Accordingly, the equations (2.23), (2.24) and (2.25) modify into

$$\frac{\partial E_{2\omega}}{\partial z} = i \frac{2\omega d_{eff}}{n_{2\omega} c} E_\omega^2 e^{i\Delta k z} \quad (2.26)$$

$$\frac{\partial E_\omega}{\partial z} = i \frac{2\omega d_{eff}}{n_\omega c} E_\omega^* E_{2\omega} e^{-i\Delta k z} \quad (2.27)$$

where E_ω , and $E_{2\omega}$ are the electric fields for the fundamental (ω) and the SH (2ω) waves. $\Delta k = k_{2\omega} - 2k_\omega$ is the phase-mismatch between the fundamental and the SH beam. The refractive indices of the medium at ω and 2ω are denoted as n_ω and $n_{2\omega}$.

If we assume amplitude of the fundamental frequency (ω) to be constant (also known as the ‘no-pump depletion’ approximation) then Eq. (2.26) can be reduced to an analytically solvable form. The SH intensity, in this case, could be represented as [34]

$$I_{2\omega}(z) = \frac{\epsilon_0 n_{2\omega} c}{2} |E_{2\omega}^2| \quad (2.28)$$

$$\Rightarrow I_{2\omega}(z) = \frac{2\omega^2 d_{eff}^2 z^2 I_\omega^2}{\epsilon n_\omega^2 n_{2\omega} c^3} \text{sinc}^2 \left[\frac{\Delta k z}{2} \right] \quad (2.29)$$

here z , I_ω and $I_{2\omega}$ are the crystal length, fundamental beam intensity and SH beam intensity respectively. This relation provides the information that, in order to have the maximum conversion efficiency, the sinc^2 term should be equal to 1. This is only possible if $\Delta k = 0 \Rightarrow n_\omega = n_{2\omega}$ *i.e.* the refractive index at 2ω should be equal to refractive index at ω which is known as the phase-matching (PM) condition as well. The possibility of carrying out phase-matching would be discussed in subsequent sections.

2.5 Phase-matching condition

Phase matching is a necessary condition for the efficient nonlinear optical interaction and generation. It arises due to the difference in velocities (phase velocity) seen by the fundamental and SH wave at ω and 2ω frequencies respectively along the propagation in the nonlinear medium. The SH intensity in the Eq. (2.29) will become maximum $I_{2\omega}(\text{max})$ when $\Delta k = 0$. In order to have a physical understanding of the phase-matching, let us consider a small section of nonlinear material from $z = 0$ to $z = z_0$ as depicted in the Fig. 2.3. As the fundamental beam (λ_ω) interacts with a material, it generates a SH beam at $z = 0$. When this SH beam propagate distance $z = z_0$, it acquires a phase due to the distance (z_0) traveled. The acquired phase will be $\phi_{SH} = \frac{2\pi n_{2\omega}}{\lambda_{2\omega}} z_0$. The phase of the

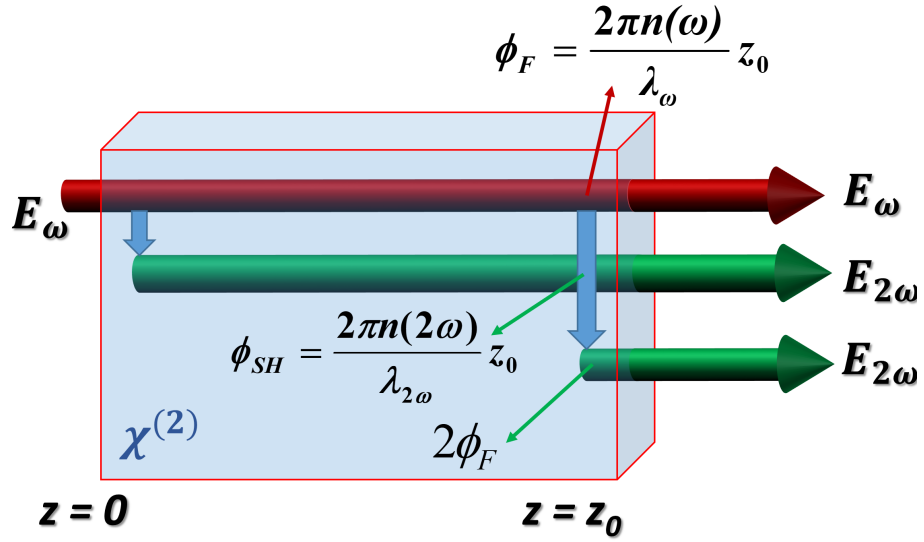


Figure 2.3 A pictorial representation for understanding the physical origin of the phase matching [33]. Phase-difference of the fundamental (in a slice of $\chi^{(2)}$ material) at $Z = 0$ and $z = z_0$ along with the phase of the generated SHG beam at these points gives rise to the phase matching condition i.e. $n(2\omega) - n(\omega) = 0$.

fundamental wave at this point (z_0) will be $\phi_F = \frac{2\pi n_\omega}{\lambda_\omega} z_0$. Additionally, there will be a SH beam generated by the fundamental beam at this point. This will have a phase of $2\phi_F$. Therefore, to constructively add to the generated SH at $z = z_0$, the phase difference should be $2\phi_F - \phi_{SH} = 0$. This condition also reduces to $n_{2\omega} = n_\omega$. So, this implies that if $\Delta k = 0$ then only the SH generated beam at each point in the nonlinear crystal, will add up constructively in phase, thereby providing a maximum SH power. The normal dispersion of conventional materials used in optics always hinder in satisfying the phase-matching condition as $n_{2\omega} > n_\omega$.

In order to circumvent this, there are two popular techniques namely birefringent phase-matching (BPM) and quasi-phase-matching (QPM).

2.5.1 Birefringence phase-matching

This is the most common and oldest phase-matching technique. In order to compensate for the phase-mismatch (non-zero Δk), the birefringence property of anisotropic nonlinear crystal is utilised. The birefringence is a property of optical materials in which, the re-

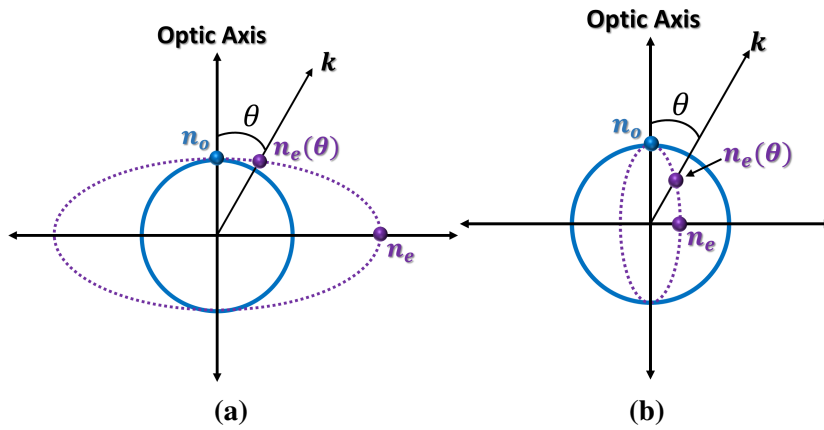


Figure 2.4 Representation of index ellipsoids in uniaxial (a) positive and (b) negative crystals.

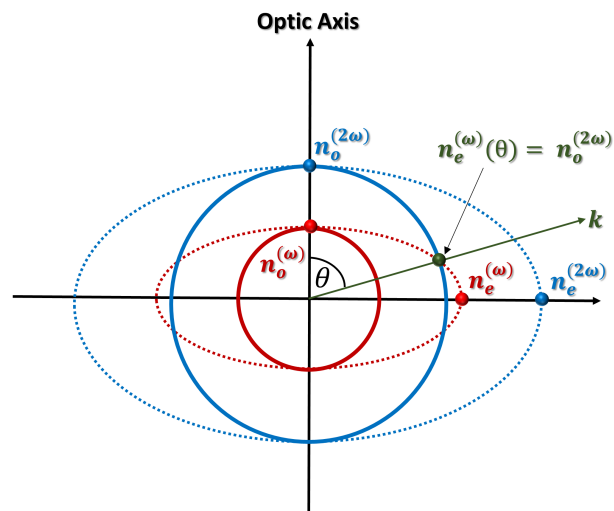


Figure 2.5 The intersecting ellipsoids for the positive uniaxial crystals shows the phase matching condition at an angle θ which is also known as the angle PM.

refractive index of the material depends on the polarisation and the direction of propagation of the incident light beam. Usually, the birefringent crystals are divided into two broad categories (i) uniaxial which have one optic-axis and (ii) biaxial having two optic-axes. A propagating beam sees two different refractive indices in a uniaxial crystal. One is known as ordinary index of refraction (n_o) and other is extra-ordinary index of refraction (n_e). n_o is experienced by the light polarised in the perpendicular direction to the plane containing the propagation vector k and the optic-axis. Similarly, the light polarized in the plane of k and the optic-axis experiences n_e . n_o remains same in all directions whereas n_e depends on the θ which is the angle between the k and the optic-axis. This dependence could be written as

$$\frac{1}{n_e^2(\theta)} = \frac{\cos^2\theta}{n_o^2} + \frac{\sin^2\theta}{n_e'^2} \quad (2.30)$$

where n_e' is the principal value of n_e . This equation tells that

$$n_e(\theta) = n_e' \text{ for } \theta = 90^\circ \quad (2.31)$$

$$n_e(\theta) = n_o \text{ for } \theta = 0^\circ \quad (2.32)$$

There is a further division in the uniaxial crystal such as (i) positive crystals ($n_o < n_e$) and (ii) negative crystal ($n_o > n_e$) which are depicted in Fig. 2.4(a) and 2.4(b). The difference $|\Delta n| = n_o - n_e$ provides the birefringence of the materials. Fig. 2.5 represents the indicatrix diagram for phase matching in a +ve uniaxial crystal. Here, the ordinary refractive index at SH wavelength (2ω) intersects the extraordinary refractive index of fundamental wave (ω) plot at an angle θ . At this point, the PM condition is satisfied. An example with real values is illustrated below.

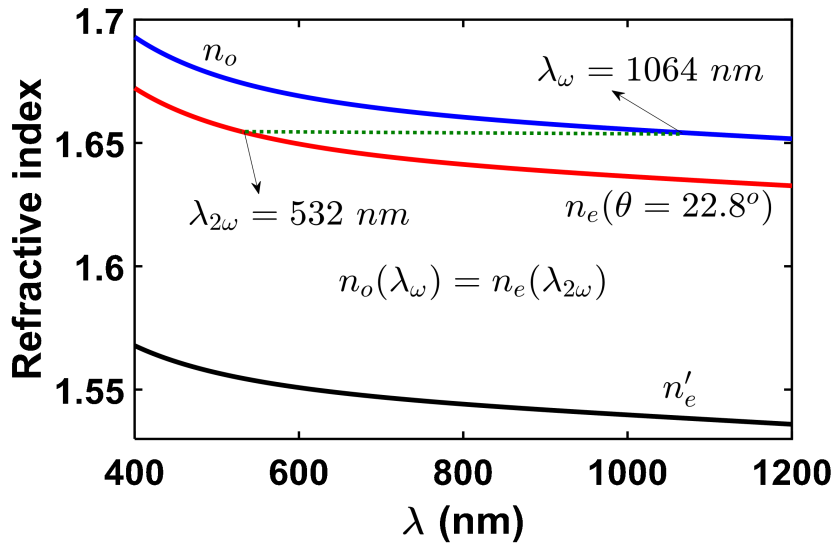


Figure 2.6 Variation of the refractive index of BBO crystal with wavelength as per the Sellmeier eq. (2.33) and (2.34)

In order to understand the BPM, let us take an example of SHG in BBO crystal. It is a $-ve$ uniaxial crystal and it satisfies the following Sellmeier relation as per [35]

$$n_o^2(\lambda) = 2.7359 + \frac{0.01878}{\lambda^2 - 0.01822} - 0.01471\lambda^2 + 0.0006081\lambda^4 - 0.00006740\lambda^6 \quad (2.33)$$

$$n_e^2(\lambda) = 2.3753 + \frac{0.01224}{\lambda^2 - 0.01667} - 0.01627\lambda^2 + 0.0005716\lambda^4 - 0.0000630\lambda^6 \quad (2.34)$$

Using the above Sellmeier relation, type-I ($o + o \rightarrow e$) phase matching can be realised at $\theta = 22.8^\circ$ for a SHG of 1064 nm. The energy conservation could be expressed as $\frac{1}{1064} + \frac{1}{1064} = \frac{1}{532}$. Fig. 2.6 is the plot between the wavelength and the refractive index of the BBO crystal. The red-curve is the ordinary index of variation and the black curve is the extra-ordinary refractive index whereas the blue curve is the extra-ordinary index variation at an angle of $\theta = 22.8^\circ$. It can be observed from this figure that $n_o(1064 \text{ nm}) = n_e(\theta = 22.8^\circ, 532 \text{ nm})$ where the PM condition is being satisfied. Similar examples for efficient SHG also exist for $+ve$ uniaxial crystals.

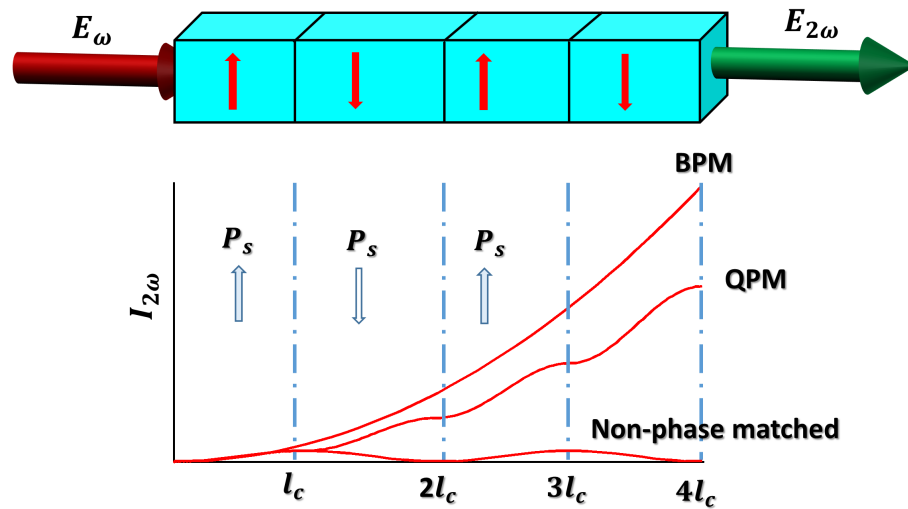


Figure 2.7 Schematic of a QPM process after each coherence length, the direction of polarisation (P_s) is inverted. In the birefringence case, the SHG builds up quadratically with the perfect phase-matching i.e. $\Delta k = 0$ along the propagation direction. In QPM, this build-up is a ‘model’ step process with $\Delta k \neq 0$ as additional π phase-shift is introduced for each coherence length. In case of no phase-matching, the periodic variation of SHG with $\Delta k \neq 0$ is shown.

2.5.2 Quasi-phase matching

As described in the section above, the birefringence property of a certain nonlinear crystal could be used to achieve efficient nonlinear optical interaction. However, BPM has several shortcomings which include (i) it is always not possible to obtain phase-matching at wavelength of interest [33] (ii) the nonlinearity (d_{eff}) of the birefringent materials are also not enough to get the efficient nonlinear interaction. Quasi-phase-matching (QPM) is a promising and practical alternative for BPM when crystals exhibiting ferroelectricity are involved. QPM does not necessarily use the birefringence property of the material. Rather, QPM involves artificial structuring of the nonlinear material to achieve the phase-matching. This provides an added advantage over the BPM as it can also be realised in the isotropic material which exhibit ferroelectric properties. The theory of the QPM was first proposed by Armstrong *et al.* in 1962 [36]. However, it was experimentally realized much later in the decade of 1980 which was essentially a consequence of practical difficulties in structuring nonlinear materials at micrometer scale. The theory of QPM is based on the change of sign of the nonlinear coefficient (d) in medium which exhibits

spontaneous polarisation below the Curie temperature (T_c) in a ferroelectric crystal. Usually, the nonlinear polarization and the generated *em*-wave tends to get out of phase after certain distance called the coherence length (l_c) if the phase-matching condition is not satisfied in a nonlinear crystal. In order to bring back the two in-phase, the nonlinear coefficient is forced to change its sign for after a certain period. This period is known as coherence length and the change in sign of the nonlinear coefficient results in an abrupt addition (or reversal) of phase π to the nonlinear polarization. This brings back the nonlinear polarization and the newly generated *em* wave back into phase. Consequently, a periodic variation (with a period of $2l_c$) in the sign of nonlinear coefficient would result in an efficient frequency conversion.

In order to have a quantitative description of QPM, let us consider a simple case of plane-wave SHG with no-pump depletion approximation discussed above. The solution of the governing equation for the evolution of the SH field under slowly varying amplitude approximation is given by [37],

$$E_{2\omega}(L) = \Gamma \int_0^L d(z) \exp(-i\Delta kz) dz \quad (2.35)$$

here $d(z)$ is the spatially varying nonlinear coefficient and

$$\Delta k = k_{2\omega} - 2k_{\omega} - K_m \quad (2.36)$$

with $K_m = \frac{2\pi m}{\Lambda}$ and $\Lambda = 2l_c$. Eq. (2.36) gives the total wavevector mismatch. It signifies that the QPM will be similar to the conventional phase-matched situation with an effective mismatch Δk shifted by an amount K_m with respect to Δk . This also suggests that an effective nonlinear coefficient $d_Q = d_{eff} G_m$ will be used in place of d_{eff} .

2.6 Optical Parametric oscillator

As described in the Sec. 2.3, a strong pump laser beam will produce a signal and an idler beam while interacting with a medium possessing $\chi^{(2)}$ optical nonlinearity. This process is termed as the parametric fluorescence or optical parametric generation (OPG). The gain in this process is relatively small and therefore, to derive a plausible optical source out of it, a positive feedback scheme necessarily needs to be adopted. In order to realise a positive feedback, the nonlinear crystal ($\chi^{(2)} \neq 0$) is kept inside a optical cavity which provides a feedback through reflecting signal, idler or both. This configuration is known as the optical parametric oscillator. Solid state lasers, which have a similar operating scheme, rely on stimulated emission between real energy eigenstates of a material system whereas the operation of OPOs hinge on the parametric gain associated in transition between two (or more) virtual energy levels. The parametric gain in OPOs is governed by the solution of coupled-wave equations described in Sec. 2.4. Ascertaining an exact solution is not straightforward in case of OPOs, however, a simplified expression for signal gain under no pump depletion approximation could be given by [38]

$$G_s(z=l) = \frac{I_s(z=L)}{I_s(z=0)} - 1 \quad (2.37)$$

$$G_s(z=l) = \Gamma^2 L^2 \frac{\sinh^2 \sqrt{\Gamma^2 - \left(\frac{\Delta k L}{2}\right)^2}}{\Gamma^2 L^2 - \left(\frac{\Delta k L}{2}\right)^2} \quad (2.38)$$

where I_s is the signal field intensity; L is the interaction length of nonlinear crystal; Δk is the phase-mismatch; and Γ is the gain factor which is calculated as

$$\Gamma^2 = \frac{8\pi^2 d_{eff}^2}{c\epsilon_0 n_p n_s n_i \lambda_s \lambda_i} I_p(0) \quad (2.39)$$

Here, $n_{p,s,i}$ are the refractive indices at pump (λ_p), signal (λ_s) and idler (λ_i) wavelengths respectively. $I_p(0)$ is the input pump intensity. Another method of representing the gain

factor is

$$\Gamma^2 = \frac{8\pi^2 d_{eff}^2}{c\epsilon_0 n_0^2 n_p \lambda_0^2} (1 - \delta^2) I_p(0) \quad (2.40)$$

Here, δ is the degeneracy factor which is defined as

$$1 - \delta = \frac{\lambda_0}{\lambda_s}; \quad 1 + \delta = \frac{\lambda_0}{\lambda_i} \quad (0 \leq \delta \leq 1) \quad (2.41)$$

with $\lambda_0 = 2\lambda_p$ is called as the degeneracy wavelength ($\lambda_s = \lambda_i = 2\lambda_p$) having refractive index n_0 , and δ is the degeneracy factor. Eq. 2.40 shows that the parametric gain has a maximum value when $\delta \approx 0$ *i.e.* at degeneracy and it decreases as $\delta \rightarrow 1$.

The present discussion is based on the simplified model based on plane-wave approximation. It is important to note that practical laser beams are found in Gaussian beam profile which could be modelled by slightly modifying the expression for plane-waves. The modified expression is given as

$$\Gamma^2 = \frac{8\pi^2 d_{eff}^2}{c\epsilon_0 n_0^2 n_p \lambda_0^2} (1 - \delta^2) (4w_p^2 T_{max}^2) I_p(0) \quad (2.42)$$

where $T_{max}^2 = \frac{1}{4(w_s^2 + w_i^2)} = \frac{\pi n_0}{4L\lambda_0} (1 - \delta^2)$ or the gain factor could also be written as

$$\Gamma^2 = \frac{16\pi^2 d_{eff}^2}{c\epsilon_0 n_0^2 n_p \lambda_0^2} (1 - \delta^2)^2 \frac{\pi w_p^2}{L} I_p(0) \quad (2.43)$$

here w_p, w_s, w_i are the beam-waists for the Gaussian beam for pump, signal and idler waves respectively. If we choose the phase-mismatch $\Delta k = 0$ in the Eq. 2.38 the signal gain could be given by

$$G_s(z = L) = \sinh^2(\Gamma L) \quad (2.44)$$

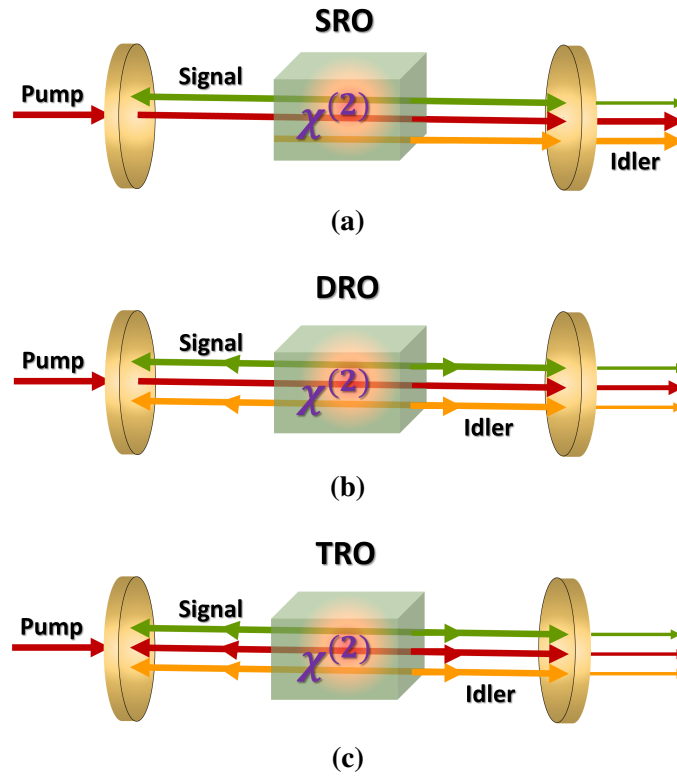


Figure 2.8 (a) Singly-resonant OPO where only one frequency i.e. signal resonates inside the cavity, (b) doubly-resonant i.e. both signal and idler resonates (c) the triply resonant OPO where all the three wavelengths resonate.

under small gain approximation i.e. $\Gamma L \ll 1$, the above equation modifies to

$$G_s(z = L) \cong \Gamma^2 L^2 \quad (2.45)$$

which shows the quadratic dependence of single-pass signal gain on the propagation length inside the medium. In case of appreciably high gain i.e. $\Gamma L \gg 1$, the expression reduces to

$$G_s(z = L) \cong \frac{1}{4} e^{2\Gamma L} \quad (2.46)$$

which suggests that the single-pass signal gain will exponentially increase with a coefficient proportional to 2Γ .

2.7 OPOs and resonance wavelengths

The very first CW OPO was demonstrated by Smith *et al.* in 1968 [39]. They have used $Ba_2NaNb_5O_{15}$ as the nonlinear medium. They deployed a high-power multimode pump and showed OPO tunability in the NIR. Later that year, a standing-wave as well as travelling wave OPO using $LiNbO_3$ crystal which operates in the visible part of the spectrum were published [40]. It is worthwhile to point out that the signal gain of parametric devices are of the order of 0.1 to 1000 for typical pump sources and standard nonlinear materials. This gain is usually insufficient to achieve macroscopic amplification of parametrically generated waves in the continuous-wave operation. The operation of an OPO needs a sufficient gain at parametric wavelengths. It is achieved by providing feedback at the generated wavelengths through various cavity configurations. There are three wavelengths in the OPO process. One is the pump and other two are the down-converted signal and idler. Either of them could resonate inside the OPO cavity. If only signal wavelength (or only one) resonates then this configuration is termed as singly resonant optical parametric oscillator (SRO). However, if signal and idler both resonates then it is known as a doubly resonant OPO (DRO). Although, the DRO has relatively low pump threshold than the SRO, it is imperative to satisfy longitudinal mode resonance condition for both the wavelengths which affect the stability as well as smooth tuning for the case of DRO. This process will be discussed later. A triply resonant OPO (TRO) is the one for which all the three wavelengths *i.e.* pump, signal and idler resonate inside the OPO cavity. A schematics of all the three configurations are given in the Fig. 2.8. A few other OPO configurations have also been reported such as pump enhanced SRO. In this configuration, apart from the resonant signal, pump beam is allowed to traverse a longer distance within the cavity for generating stronger signal/idler beam. This thesis will essentially focus only on CW SRO configurations.

2.8 Threshold of SRO and DRO

Under no pump depletion and perfect phase matching ($\Delta k = 0$), the first two coupled wave equations (2.23), (2.24) necessarily needs to be solved as E_3 will be constant. In the SRO configuration, one of the smaller frequency wave, say the signal wave, resonates inside the OPO cavity. Further, we assume a single-pass scheme which result in parametric gain in the forward (with respect to pump) direction only. Also, we assume that the loss of the signal beam (α_s) is small enough such that the coupled Eq. (2.23) for the variation of the idler beam in the nonlinear media is given by

$$\frac{\partial E_i}{\partial z} = \frac{i\omega_1 d_{eff}}{cn_1} E_p E_s^* = cont. \quad (2.47)$$

This shows that the idler wave will grow linearly along the crystal propagation direction (z) [41]. Due to absence of any back reflection for idler wave, the idler electric field is given by

$$E_i(z) = i\kappa_i E_p E_s^* z \quad (2.48)$$

By substituting this into the coupled-wave equation for the signal-wave, we obtain

$$\frac{\partial E_s}{E_s} = \frac{\kappa_s \kappa_i E_p E_p^* L^2}{2} \quad (2.49)$$

$$\Rightarrow \frac{\partial I_s}{I_s} = \kappa_s \kappa_i L^2 (E_p E_p^*) \quad (2.50)$$

Using the relation $E_p E_p^* = \frac{2(\mu_0/\epsilon_0)^{1/2} I_p}{n_p}$, the above equation could be modified as

$$\frac{\partial I_s}{I_s} = \frac{2(\mu_0/\epsilon_0)^{1/2} \kappa_s \kappa_i L^2 I_p}{n_p} \quad (2.51)$$

By equating the fractional round-trip gain in the signal to the fractional round-trip power loss (α_s), the threshold condition comes out to be

$$\frac{2(\mu_0/\varepsilon_0)^{1/2}\kappa_s\kappa_iL^2I_p}{n_p} = \alpha_s \quad (2.52)$$

$$\Rightarrow \frac{2(\mu_0/\varepsilon_0)^{1/2}\omega_s\omega_id_{eff}^2L^2I_{th}^{SRO}}{c^2n_pn_s n_i} = \alpha_s \quad (2.53)$$

$$\Rightarrow \frac{8\pi^2L^2d_{eff}^2I_{th}^{SRO}}{c\varepsilon_0n_pn_s n_i\lambda_s\lambda_i} = \alpha_s \quad (2.54)$$

Here, I_{th} is the pump threshold intensity which is required to begin the OPO oscillation. λ_s, λ_i are the signal and the idler wavelengths in the free-space. In a DRO, the analytical treatment is similar and consequently, the DRO threshold is given as [41]

$$\frac{8\pi^2L^2d_{eff}^2I_{th}^{DRO}}{c\varepsilon_0n_pn_s n_i\lambda_s\lambda_i} = \frac{\alpha_s\alpha_i}{2} \quad (2.55)$$

Further, it could be deduced from the Eq.(2.54) and (2.55) that

$$\frac{I_{th}^{SRO}}{I_{th}^{DRO}} = \frac{\alpha_i}{4} \quad (2.56)$$

This Eq. (2.56) confirms that the SRO threshold will be higher by a factor of $4\alpha_s$ as compared to the DRO. Although, experimentally the I_{th}^{DRO} is almost $100\times$ lesser than I_{th}^{SRO} but in DRO one needs to satisfy condition for resonance at signal as well as idler wavelength which is given by

$$\omega_p = \omega_s + \omega_i \quad (2.57)$$

$$\omega_p n_p = \omega_s n_s + \omega_i n_i \quad (2.58)$$

$$\omega_s = p \frac{\pi c}{n_s L}; \quad p = 1, 2, 3, \dots \quad (2.59)$$

$$\omega_s = q \frac{\pi c}{n_i L}; \quad q = 1, 2, 3, \dots \quad (2.60)$$

Table 2.1 Wavelength tunability of an SRO made of 5mol% MgO doped PPLN crystal with a pump of 1064 nm.

Temperature (20 – 200°C)			
$\Lambda_{QPM}(\mu m)$	Pump(nm)	Signal(nm)	Idler(nm)
28	1064	1410 – 1434	4300 – 4120
29	1064	1450 – 1485	4000 – 3750
30	1064	1503 – 1566	3640 – 3320
31	1064	1589 – 1732	3220 – 2760

Simultaneously satisfying both the resonant conditions along with phase-matching condition is quite challenging which adversely affects the OPO stability. However, the condition for longitudinal resonance for ω_i is relaxed for SRO which brings in high spectral as well as temporal stability.

2.9 Tuning characteristics of SRO

Wavelength tuning is the most attractive feature of OPOs. Most of the lasers operate at fixed wavelengths and lack broad spectral tunability. In an OPO, the phase-matching condition could be appropriately tailored for achieving frequency tunability *i.e.* the phase-mismatch factor $\Delta k = k_p - k_s - k_i$ could be made zero by optimally tailoring the material dispersion through altering a physical quantity such as temperature of the medium or angular orientation of a crystal. For quasi-phase-matched OPG in a periodically-poled nonlinear crystal having grating period (Λ), Δk is expressed as

$$\Delta k = 2\pi \left[\frac{n_p(\lambda_p, T)}{\lambda_p} - \frac{n_s(\lambda_s, T)}{\lambda_s} - \frac{n_i(\lambda_i, T)}{\lambda_i} - \frac{1}{\Lambda} \right] \quad (2.61)$$

As discussed before, the parametric gain maximizes when $\Delta k = 0$. By altering the crystal properties (described below), the phase-matching condition could be satisfied at various wavelengths. Consequently, we could tune the OPO output frequencies. It is important to

note that the refractive index (which determines the magnitude of wavevector) as seen by an *em*-wave could be altered through the following parameters

- Crystal angle (birefringent materials)
- QPM grating period (periodically poled material)
- Temperature of the crystal

In order to understand the point, let us consider an example of PPLN crystal. The Sellmeier's equation for 5 *mol %* MgO doped PPLN has the following form as calculated by Paul *et al.* [42]

$$n_e^2(\lambda, T) = 5.319725 + 4.753469 \times 10^{-7}[(T - 24.5)(T + 570.82)] \quad (2.62)$$

$$+ \frac{0.09147285 + 3.310965 \times 10^{-8}[(T - 24.5)(T + 570.82)]}{\lambda^2 - 0.3165008^2} \quad (2.63)$$

$$+ \frac{100.2028 + 2.760513 \times 10^{-5}[(T - 24.5)(T + 570.82)]}{\lambda^2 - 11.37639^2} \quad (2.64)$$

$$+ 0.01497046\lambda^2 \quad (2.65)$$

The wavelength λ should be in μm units and the temperature 'T' will be in $^{\circ}C$ for this equation. By numerical solving the phase-matching condition using Eq. (2.61), we obtain the phase-matched wavelengths (signal and idler) at different MgO-doped PPLN crystal temperatures for various grating periods and the wavelengths are tabulated in the table 2.1 assuming a 1064 *nm* pump source. This gives a distinct characteristic of broadband tuning from a PPLN crystal for only five grating periods satisfying the QPM. In Fig. 2.9, we have plotted the variation of the phase-matched signal and the idler wavelengths for 5 *mol %* MgO:PPLN. In this simulated graph, we have taken the grating periods 28.5, 29, 29.5, 30, 30.5, 31, 31.5 μm and used the Sellmeier's equation discussed above. It can also be observed from the Fig. 2.9 that a degeneracy point appears above 200 $^{\circ}C$ at a grating period of 31.5 μm . At this point the signal and idler wavelengths will be identical *i.e.* $\lambda_s = \lambda_i$.

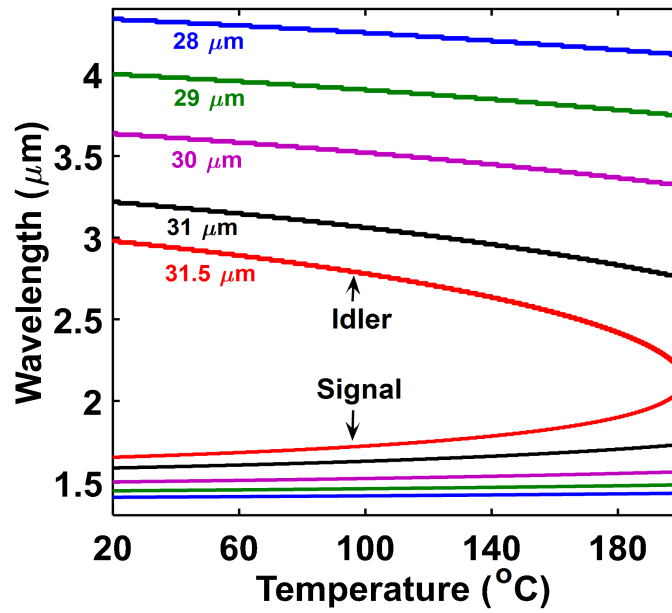


Figure 2.9 Variation of signal and Idler wavelengths at different grating periods (Λ_{QPM}) ranging from 28 – 31.5 μm at fixed pump of 1064 nm for MgO doped PPLN crystal.

2.10 Nonlinear crystals for OPO

The following properties need to be considered for choosing a nonlinear crystal for an OPO.

1. Broad transparency range
2. Possibility of phase-matching at the wavelength of interest
3. High optical damage threshold
4. Large thermal conductivity
5. Availability in long size
6. Low cost
7. High nonlinear figure of merit

The nonlinear figure of merit (FOM) is defined as [41]

$$f \equiv \frac{d_{eff}}{\sqrt{n_p n_s n_i}} \quad (2.66)$$

FOM is a physical parameter and it is totally dependent on material properties. A large value of FOM indicates a better choice for nonlinear conversion. As crystals exhibiting transparency in infrared have high refractive index values and they also exhibit high d_{eff} which in turn suggests a higher FOM. For example, $LiNbO_3$ has refractive index of ≈ 2.2 at 1064 nm and it has a d_{eff} value of 17 pm/V for QPM.

2.11 Cavity design

There are basically two kinds of cavity designs (1) standing-wave resonator and (2) ring resonator. The design of standing wave resonators are relatively simpler as compared to the ring resonator which is shown in Fig. 2.10(a). However, in the standing wave design, the fundamental wave travel in both the directions thereby, generating signal as well as the idler if PM condition is satisfied for both the directions. In this case, an important concern is backward travelling fundamental wave could provide a feedback to pump laser which may induce modulation instabilities in the fundamental beam. On other hand, the ring resonators (Fig. 2.10(b)) are insensitive to small misalignments for the mirrors in the ring plane. A ring resonator offers an important advantage in terms of possibility to insert more optical elements at the other arm. The other optical elements could be accommodated in standing-wave design through small but vital variations such as V-cavity (Fig. 2.10(c)) or X-cavity (Fig.2.10(d)). In the present thesis, we have considered the ring-cavity designs only.

2.11.1 Matrix formulation for beam propagation

The ray matrix method is utilised for the beam propagation in the ring-cavity configuration. Ray matrix method is also termed as the ABCD matrix method. Consider a light ray propagating in the z -direction from a plane at z_1 to $z_2 = z_1 + L$ with transverse displacement $r(z)$ and having a slope dr/dz . The input and output coordinates of this ray

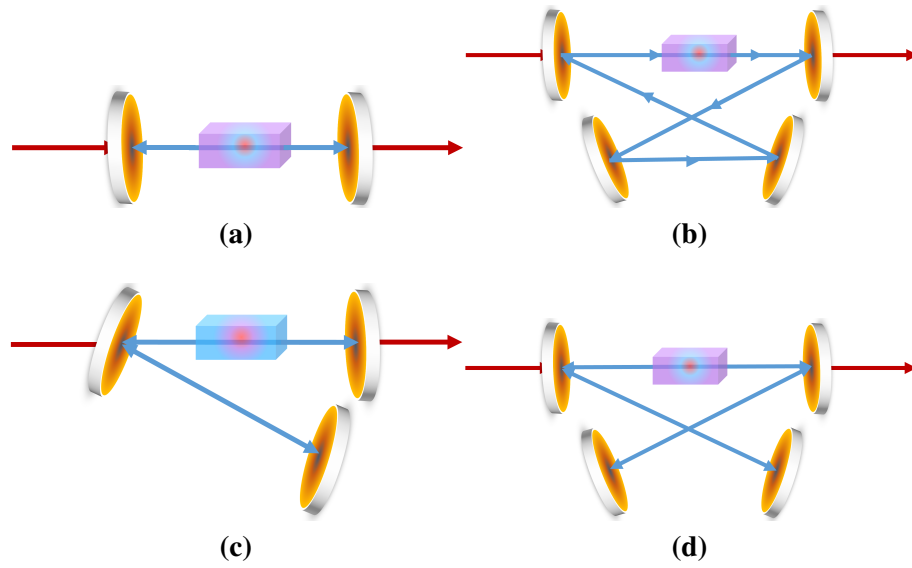


Figure 2.10 Cavity designs \Rightarrow (a) two mirror linear cavity, (b) four mirror ring cavity, (c) three mirror V-shaped cavity and (d) four mirror X-shaped cavity.

will be related through the transformation

$$r_2 = r_1 + L \frac{dr_1}{dz} \quad (2.67)$$

$$\frac{dr_2}{dz} = \frac{dr_1}{dz} \quad (2.68)$$

It is important to note that the slope of the ray in the medium will also have a refractive index dependence. Hence, the equation will be modified as $r'(z) = n(z) \frac{dr}{dz}$. Using this, one can connect the input and output displacements and slopes as

$$r_2 = Ar_1 + Br_1' \quad (2.69)$$

$$r_2' = Cr_1 + Dr_1' \quad (2.70)$$

Here, r'_1 and r'_2 are the modified ray slopes at input and output planes respectively. A, B, C and D are defined by the properties of optical element. In general,

$$r_2 \equiv \begin{bmatrix} r_2 \\ r'_2 \end{bmatrix} = \begin{bmatrix} A & B \\ C & D \end{bmatrix} \times \begin{bmatrix} r_1 \\ r'_1 \end{bmatrix} \equiv Mr_1 \quad (2.71)$$

where M is the ray matrix of an optical element. The ray matrix for various optical elements which are used in this thesis are tabulated in Table-2.2 below [43].

2.12 Gaussian Beam

Commercially available high-end lasers emit in TEM_{00} transverse-mode which resembles a Gaussian beam profile. In order to obtain an insight for the Gaussian beam propagation, let us consider the Helmholtz equation which can be written as

$$(\nabla^2 + k^2)E(x, y, z) = 0 \quad (2.72)$$

where $k = n\omega/c$ and $E(x, y, z)$ is the complex amplitude of electric field vector. Assuming, the wave-propagation to be along the z -direction, the electric field amplitude could be expressed as

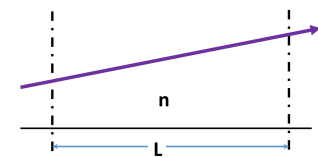
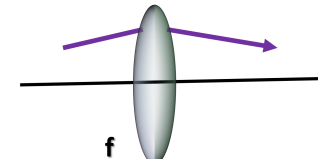
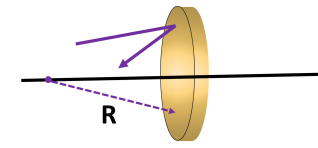
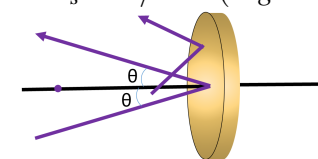
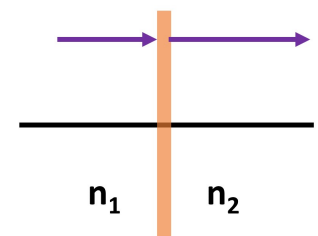
$$E(x, y, z) = u(x, y, z)e^{-ikz} \quad (2.73)$$

By considering the *paraxial wave approximation*, the electric-field amplitude is slowly varying on the scale of λ (along z -direction) as well as along the transverse direction. Therefore, one can simplify Eq. (2.72) to appear as

$$\frac{\partial^2 u}{\partial x^2} + \frac{\partial^2 u}{\partial y^2} - 2ik \frac{\partial u}{\partial z} = 0 \quad (2.74)$$

$$\Rightarrow \left(\nabla_T - 2ik \frac{\partial}{\partial z} \right) u(x, y, z) = 0 \quad (2.75)$$

Table 2.2 Ray matrix diagram of the various optical systems.

Medium of length L with refractive index n		$\begin{bmatrix} 1 & \frac{L}{n} \\ 0 & 1 \end{bmatrix}$
Thin lens with focal length $f > 0$		$\begin{bmatrix} 1 & 0 \\ -\frac{1}{f} & 1 \end{bmatrix}$
Normal incidence on curved Mirror ($R > 0$)		$\begin{bmatrix} 1 & 0 \\ -\frac{2}{R} & 1 \end{bmatrix}$
Arbitrary incidence on curved Mirror	<ul style="list-style-type: none"> • $R_t = R \cos \theta$ (tangential) • $R_s = R / \cos \theta$ (sagittal) 	$\begin{bmatrix} 1 & 0 \\ -\frac{2}{R_s(R_t)} & 1 \end{bmatrix}$
Refraction from normal incidence		$\begin{bmatrix} 1 & 0 \\ 0 & \frac{n_1}{n_2} \end{bmatrix}$

The above equation is known as the "Partial Wave Equation". In cylindrical coordinates, Eq. (2.75) could be expressed as

$$\frac{1}{r} \frac{\partial}{\partial r} \left(r \frac{\partial u}{\partial r} \right) - 2ik \frac{\partial u}{\partial z} = 0 \quad (2.76)$$

Assuming a solution of the form

$$u_0 \propto \exp\left(-i\left[P(z) + \frac{kr^2}{2q(z)}\right]\right) \quad (2.77)$$

Here, '0' indicates the lowest order (TEM_{00}) mode which has Gaussian profile. By plugging the trial solution in the paraxial wave-equation, we could arrive at

$$\frac{k^2}{q^2(z)} \left[\frac{dq(z)}{dz} - 1 \right] r^2 - 2k \left[\frac{dP(z)}{dz} + \frac{i}{q(z)} \right] r^0 = 0 \quad (2.78)$$

The solution has to hold for all values of 'r' and therefore, by separating the coefficients of r^2 and r^0 , we obtain

$$\frac{dq(z)}{dz} = 1 \quad (2.79)$$

$$\frac{dP(z)}{dz} = -\frac{i}{q(z)} \quad (2.80)$$

The solution of the Eq. (2.79) is

$$q(z) = q_0 + z \quad (2.81)$$

where q_0 is the value of q at $z = 0$. It is apparent from the above equation that q_0 has the same dimensions as z . However, it is a complex quantity. Let us consider $q_0 = iz_R$ (to be a purely imaginary quantity) then

$$q(z) = z + iz_R \quad (2.82)$$

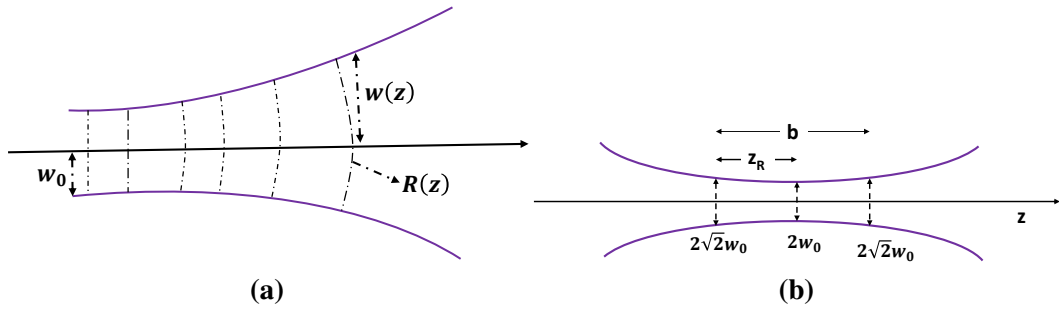


Figure 2.11 (a) Propagation of a Gaussian beam along z direction with a initial beam-waist w_0 which will eventually modify to $w(z)$ and the radius of curvature will be $R(z)$. (b) Illustration of the Rayleigh range (z_R) and the confocal parameter (b) of the focused Gaussian beam a spot size of w_0 .

Here, $q(z)$ is known as the complex radius of curvature and z_R (known as Rayleigh length) will be defined subsequently. Eq. (2.82) could also be expressed as

$$\frac{1}{q(z)} = \frac{1}{z + iz_R} = \frac{z}{z^2 + z_R^2} - i \frac{z_R}{z^2 + z_R^2} \quad (2.83)$$

Therefore, the expression representing total electric field for the Gaussian beam resembles

$$\begin{aligned} \frac{E(x, y, z)}{E_0} = & \frac{1}{[1 + (\frac{z}{z_R})^2]^{1/2}} \exp\left[-\frac{kz_R r^2}{2(z^2 + z_R^2)}\right] \exp\left[-i \frac{kzr^2}{2(z + z_R)^2}\right] \\ & \exp\left[i \tan^{-1}\left(\frac{z}{z_R}\right)\right] \exp(-ikz) \end{aligned} \quad (2.84)$$

In order to simplify this equation, we define a few terms such as

- Spot-size $w_z = w_0 \sqrt{1 + (\frac{z}{z_R})^2}$; here $w_0 = \sqrt{\frac{2z_R}{k}}$ is the minimum spot size or the beam waist.
- Radius of curvature $R(z) = z[1 + (\frac{z_R}{z})^2]$
- Gouy phase shift $\phi(z) = \tan^{-1}(\frac{z}{z_R})$

Using the above parameters, Eq. (2.84) could be re-grouped as

$$\frac{E(x, y, z)}{E_0} = \frac{w_0}{w(z)} \exp\left[-\frac{r^2}{w^2(z)}\right] \exp\left[-i \frac{kr^2}{2R(z)}\right] \exp(-i[kz - \phi(z)]) \quad (2.85)$$

This equation is the lowest order *i.e.* TEM_{00} (Gaussian) mode. At the origin *i.e.* $z = 0$, the spot-size of the Gaussian beam is known as the beam waist $w(0) = w_0$ and it has radius of curvature $R = \infty$. A graphical representation of beam-waist and radius of curvature is shown in Fig. 2.11(a). When $R = \infty \Rightarrow q(0) = i\frac{\pi n w_0^2}{\lambda_0}$. The imaginary part of $q(0)$ is known as the Rayleigh range which is denoted as

$$z_R = \frac{\pi n w_0^2}{\lambda_0} \quad (2.86)$$

In order to understand the physical implications of Rayleigh range (z_R), let us observe the spot size at $z = z_R$ such that

$$w(z) = w_0 \sqrt{1 + \left(\frac{z}{z_R}\right)^2} = \sqrt{2} w_0 \quad (2.87)$$

This shows that size of the Gaussian beam expands by a factor of $\sqrt{2}$ at $z = z_R$. Therefore, z_R is the measure of the collimation (or spatial extent) of the beam. Usually $b = 2z_R$ is termed as the *confocal parameter*. A graphical representation for defining the same is shown in Fig. 2.11(b). In Fig. 2.12(a) and 2.12(b), a simulated and experimentally measured profiles of a Gaussian beam in the TEM_{00} mode is plotted respectively. The experimentally measured profile is a beam-intensity that for Yb-doped fiber laser source which will be discussed in the present thesis (chapter 3 onwards). The measurement has been carried out using a CCD camera (GRAS 2.0, Grasshopper Inc., USA).

2.13 Gaussian beam propagation in the OPO ring cavity

The variation in the spot size and the radius of curvature of the Gaussian beam is described in the above section. It is worthwhile to note that the complex radius of curvature ($q(z)$) is an important quantity in terms of determining the variation in phase of propagating Gaussian beam. As per the definition in the Eq. (2.83), if we plug-in the values of $z_R, R(z)$

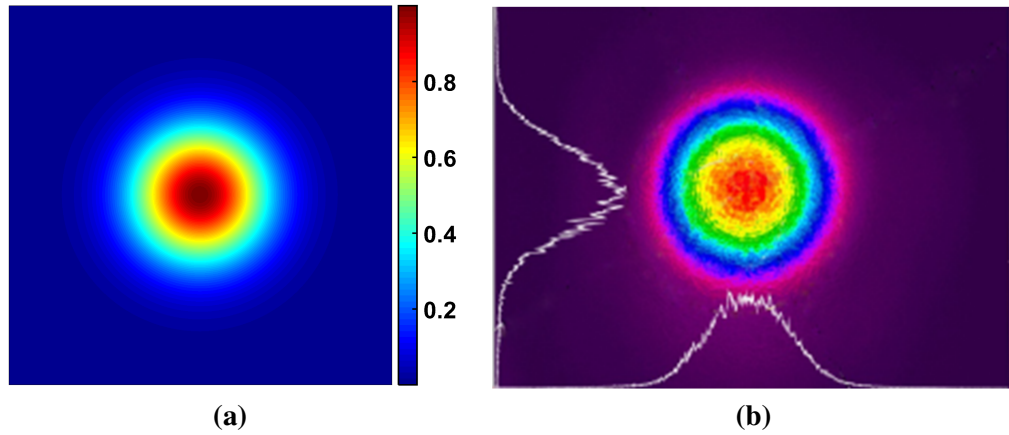


Figure 2.12 (a) A simulated temporal profile a Gaussian beam in TEM_{00} mode and (b) beam profile of Yb-fiber laser operating at 1064 nm.

and $w(z)$, then we obtain

$$\frac{1}{q(z)} = \frac{1}{R(z)} - i \frac{\lambda_0}{\pi n w^2(z)} \quad (2.88)$$

It is apparent from the above equation that if $q(0)$ is specified at an initial spot-size ($w_0(z)$) and then the radius of curvature ($R(z)$) could be directly estimated. Subsequently, complete information about the propagating Gaussian could be obtained if $q(z)$ could be evaluated at all z -planes. The ABCD matrices which have been defined earlier could be employed to ascertain $q(z)$. In order to understand this, let us consider an example of free-space propagation of a Gaussian beam. If $q(z_1) = q_1$ then at a position $z_2 = z_1 + p$

$$q_2(z_2) = q_2 = q_1 + p \quad (2.89)$$

This equation could also be written as

$$q_2 = \frac{Aq_1 + B}{Cq_1 + D} \quad (2.90)$$

where

$$\begin{pmatrix} A & B \\ C & D \end{pmatrix} = \begin{pmatrix} 1 & p \\ 0 & 1 \end{pmatrix} \quad (2.91)$$

This represents a free-space propagation using ray-matrix approach .

In the present thesis, the operation of OPO has two variants in ring-cavity configuration as mentioned below.

- four-mirror ring cavity
- six-mirror ring cavity

In order to begin the OPO design, we calculated the beam-waist as a function of position within the cavity. This is necessary for carrying out the mode-matching of oscillating signal and idler beam which has a direct consequence on the efficiency of parametric generation in the OPO. A schematic for four-mirror ring-cavity is shown in the Fig. 2.13(a). It is assumed that the Gaussian beam is focused at the center of the nonlinear crystal ($z = 0$) placed within the cavity. Here, $R(0) = \infty$ and $w(0) = w_0$. As pointed out in Eq. (2.88), q_0 could be evaluated through $q_0 = i\frac{\pi n_2 w_0^2}{\lambda_0} = iz_R$. The beam-waist at any z could be calculated using

$$w(z) = \sqrt{\frac{\lambda_s}{n\pi} \left(\frac{A^2 z_0^2 + B^2}{(AD - BC)z_R} \right)} \quad (2.92)$$

where n is the refractive index of the medium (air or nonlinear crystal) and λ_0 is the wavelength. A, B, C and D are the matrix elements of the optical element under consideration. The beam-waist at the plane $z = 0$ is given by $w_{z=0} = \sqrt{\lambda_s / (n_2 \pi) z_R}$. Therefore, the matrix at the point Lc_1 (in Fig. 2.13(a)) could then be expressed as

$$M_{Lc_1} = \begin{pmatrix} 1 & 0 \\ 0 & n_2 \end{pmatrix} \begin{pmatrix} 1 & d_1 \\ 0 & 1 \end{pmatrix} \quad (2.93)$$

Similarly, the beam-waist could be calculated with help of Eq. (2.92). In Fig. 2.13(a), we have plotted a four-mirror ring cavity by taking all the practical values. Two mirrors (M_1 and M_4) are curved with $R = -200 \text{ mm}$ and the other two mirrors (M_2 and M_3) are plane. The nonlinear medium is an 80 mm long MgO-doped PPLN crystal. The

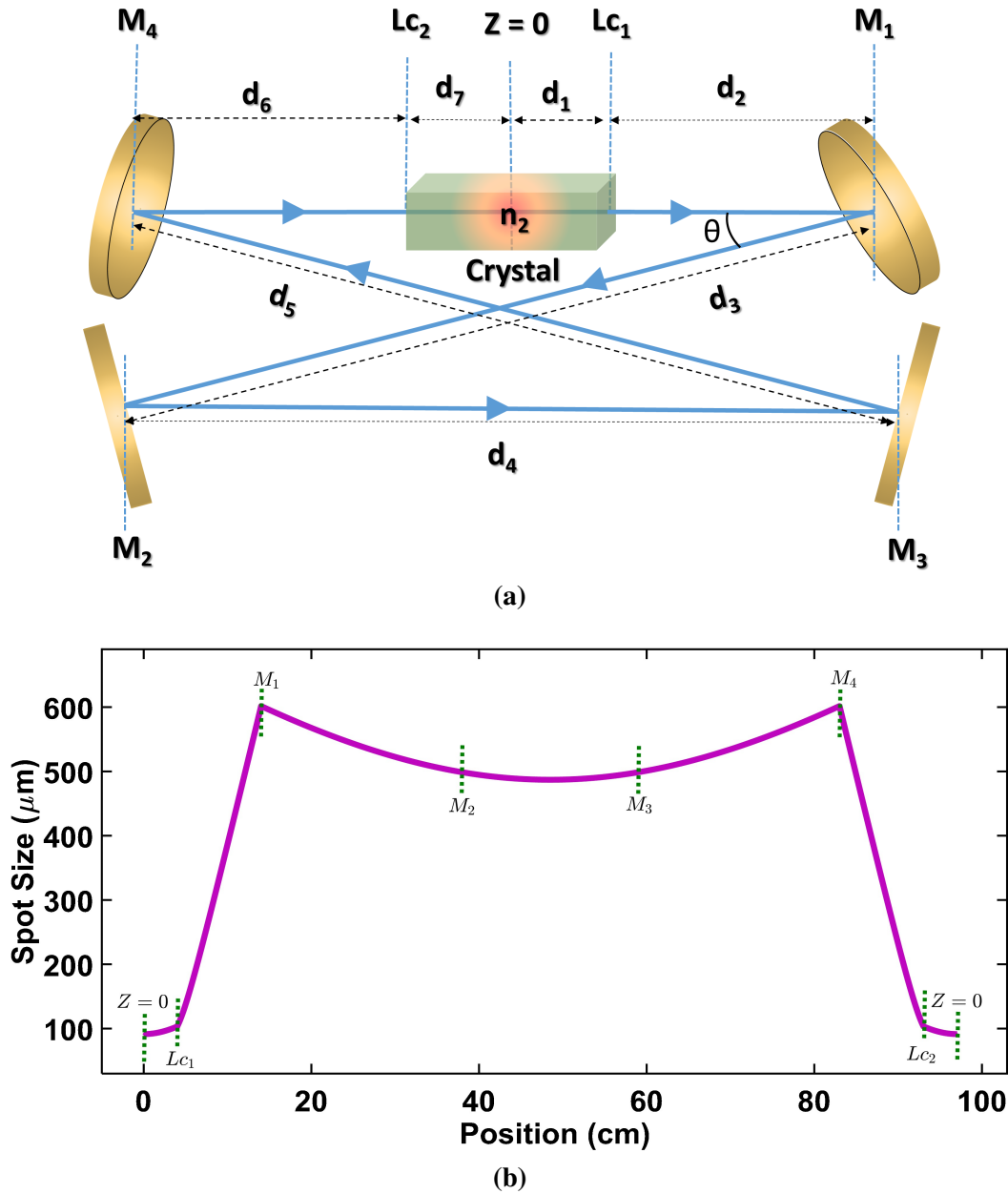


Figure 2.13 Four mirror ring cavity SRO \Rightarrow (a) The center of the crystal is designated as $z = 0$. $M_{1,2,3,4}$ are four mirrors where $M_{1,4}$ has radius of curvature 200 mm and the mirrors $M_{2,3}$ are plane. (b) the pump beam has a beam waist $w_0 = 75 \mu\text{m}$ and originates from $z = 0$ which results in a signal waist of $w_s = 94 \mu\text{m}$. The exiting signal comes out of the crystal at Lc_1 with a small divergence. At a distance d_2 , the beam diverges fast and when it reaches M_1 , it tends to focus. The beam focuses to $w(z)$ at the center of the two mirrors ($M_{1,4}$) before diverging again.

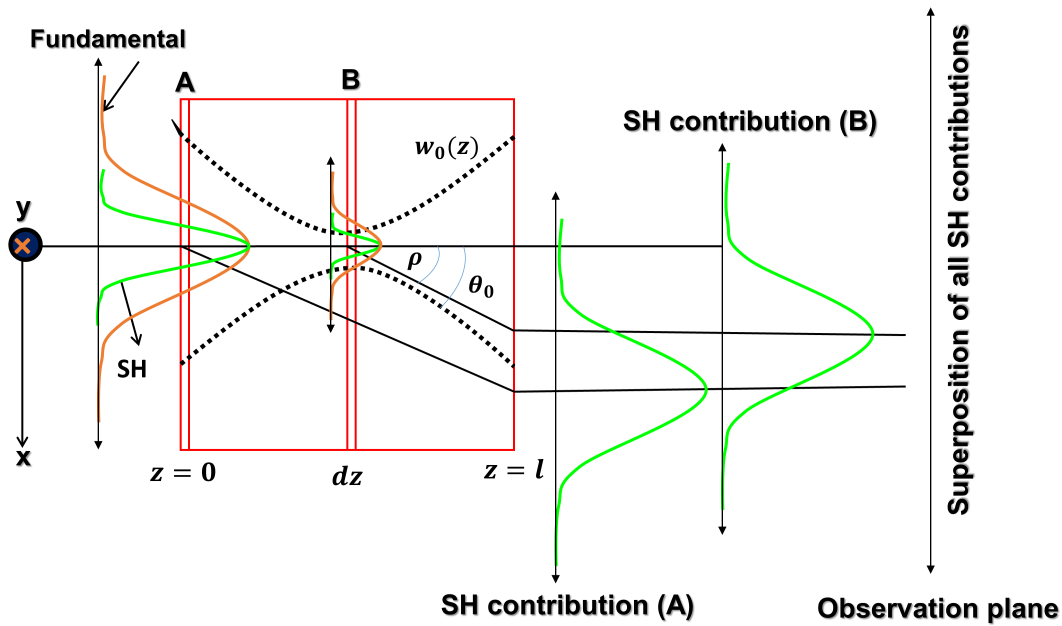


Figure 2.14 Illustration of the Boyd-Kleinman theory of SHG [33]

mode matching is realised at the center of nonlinear crystal. The other parameters are $d_1 = 40 \text{ mm}$, $d_2 = 100 \text{ mm}$, $d_3 = 240 \text{ mm}$, $d_4 = 210 \text{ mm}$, $d_5 = d_3$, $d_6 = d_2$. The pump wavelength is assumed to 1064 nm and the PPLN crystal is assumed to be at a temperature of 100°C . At $z = 0$, the pump beam-waist is considered to be $w_0 = 75 \mu\text{m}$. The Fig. 2.13(b) suggests that the signal beam waist at the center of the crystal is $94 \mu\text{m}$ and it is gradually increases and reaches a maximum at mirror M_1 . Subsequently, it reaches a local minima in the return trip before diverging further to a maximum value at M_4 . After reflection from the curved mirror M_4 , it returns to initial beam waist of $94 \mu\text{m}$ which assures a stable OPO cavity for the signal wavelength.

2.14 Boyd-Kleinman Theory of SHG of Gaussian beam

In 1968, Boyd and Kleinman proposed a heuristic approach for optimizing the generation of SH beam in the nonlinear process. They studied Type-I SHG as well as the OPG process [44]. However, we will restrict the discussion to the SHG process. Let us assume a Gaussian beam in TEM_{00} mode profile having a radial (transverse) distribution e^{-r^2/w_0^2}

and the confocal parameter of the beam is $b = 2\pi n w_0^2 / \lambda$ with w_0 as the beam spot-size and n is the refractive index of the crystal at wavelength λ . The BK theory is illustrated in the Fig. 2.14. The insight of the BK-theory has been explained through a simple model by Risk *et al.* in [33]. In the BK-theory, the crystal has been divided in many infinitesimal widths and every width generates a SH beam while interacting with the pump beam. All the generated SH beam will arrive at a observation plane as described in the Fig. 2.14. The total second-harmonic (SH) will be the sum of all the SH field produced by the crystal and hence, all the contributions will be added by considering their relative phases. The pump beam is focused so that the SH intensity for each width will be different. In the case of anisotropic media, the generated SH will experience walk off relative to the pump at an angle ρ . This in-turn will result in the spatial displacement in the SH generated at the $z = 0$ and $z = L$ (crystal length). Hence, this will adversely affect Gaussian beam profile for the SH beam. Taking such factors into account, BK-theory derived the following expression describing the generated SH power as

$$P_{2\omega} = \frac{16\pi^2 d_{eff}^2}{\epsilon_0 c \lambda_1^3 n_2 \omega n_\omega} P_\omega^2 e^{-\alpha l} h(\sigma, \beta, \kappa, \xi, \mu) \quad (2.94)$$

The term $h(\sigma, \beta, \kappa, \xi, \mu)$ is known as the ‘‘Boyd-Klienman focusing factor’’. The parameters which determine h are defined as

$$\begin{aligned} \sigma &= \frac{1}{2} b \Delta k & \beta &= \rho / \theta_0 & \kappa &= \alpha b / 2 \\ \xi &= l / b & \mu &= \frac{l - 2f}{l} \end{aligned}$$

where α is absorption for both the wavelengths and f is the position of the focus. The parameters, which needs to be optimised are σ , μ , ξ which essentially depends on phase-mismatch (Δk), point of focus of pump beam and beam-waist at the focal point respectively. Also, h -parameter depends on β which is a measure of birefringence and κ is determined by material absorption at pump frequency. In case of SHG, if we

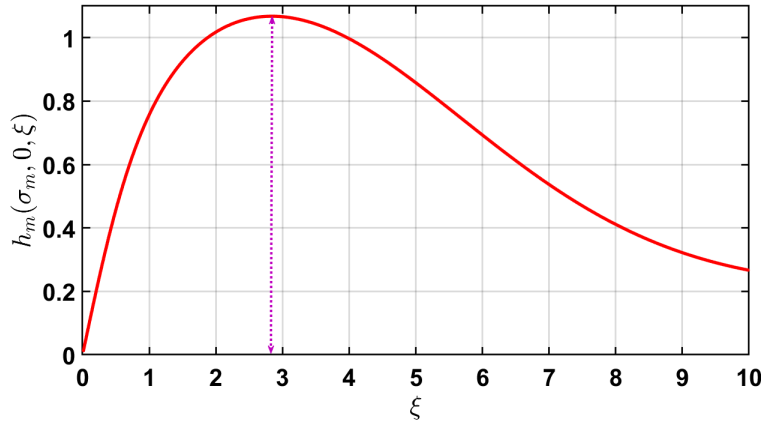


Figure 2.15 Boyd-Klienman focusing parameter as a function of focusing. Theoretically, the maximum value of h parameter is 1.068 at $\xi = 2.84$.

consider absorption to be equal to zero and set the focus at crystal center *i.e.* at $z = 0$, *i.e.* $\kappa = \mu = 0$ which makes $h \equiv h(\sigma, \beta, 0, \xi, 0)$. In order to maximise h , let us define a parameter $B = \rho\sqrt{l k_\omega}/2 = \beta\sqrt{\xi}$ and hence, the expression turns into $h(\sigma, B, \xi) = h(\sigma, B\xi^{-1/2}, 0, \xi, 0)$. In an experiment, B could be controlled through the operating wavelength λ_ω , propagation direction ρ and interaction length l . Let us consider a value of $\sigma = \sigma_m$ at which h maximises for a given B and ξ . Therefore, σ_m would be a function of B and ξ which could be represented as $\sigma_m(B, \xi)$. Therefore, h parameter would be expressed as $h(\sigma_m(B, \xi), \beta\sqrt{\xi}, 0, \xi, 0)$. By appropriately choosing $\xi = l/b$ and Δk , one could maximize the SH output. If there is no spatial walk-off due to birefringence *i.e.* $B = 0$ and the maximum value of Boyd-Klienman focusing parameter would be $h_m = 1.068$ with optimum $\xi_m = 2.84$ (Fig. 2.15). It implies that $b = l/2.84$ and hence, the optimum confocal parameter could be a factor of 2.84 times shorter than the crystal length (l). In this case, Eq. (2.94) could be written as

$$P_\omega = 1.068 \frac{16\pi^2 d_{eff}^2}{\epsilon_0 c \lambda_\omega^3 n_{2\omega} n_\omega} P_\omega^2 l \quad (2.95)$$

2.15 Stimulated polariton scattering in $LiNbO_3$

Lithium niobate is a uniaxial ferroelectric crystal with chemical formula $LiNbO_3$. It is a transparent crystal and usually grown with Czochralski method. The lattice constants are $a = 5.142\text{\AA}$ and $c = 13.863\text{\AA}$ [45]. Below the curie temperature, it belongs to space group $R3c$ and point-group $3m$. A unit cell of $LiNbO_3$ is drawn in the Fig. 2.16.

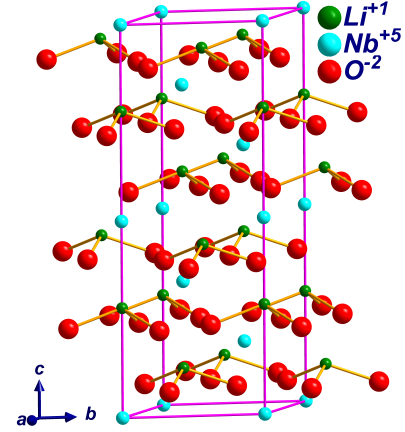


Figure 2.16 Crystal diagram of $LiNbO_3$

$LiNbO_3$ has a trigonal lattice structure with ten atoms per unit cell which gives thirty vibrational degrees of freedom and consequently, 30 phonon branches. From the spectroscopic analysis, it could be inferred that out of 30 – phonon branches, 27 are optical and the remaining three acoustical. The unit cell of $LiNbO_3$ experiences spontaneous polarization due to displaced equilibrium positions of Li^+ and Nb^{5+} ions with respect to the point which could be a centre of inversion symmetry [46]. Due to this, $LiNbO_3$ exhibits several $\chi^{(2)}$ -based nonlinear optical effects such as SHG, OPO, DFG. The d -tensor for $LiNbO_3$ is represented as

$$d_{ijk} = \begin{pmatrix} 0 & 0 & 0 & 0 & d_{15} & -2d_{22} \\ -d_{22} & d_{22} & 0 & d_{15} & 0 & 0 \\ d_{31} & d_{31} & d_{33} & 0 & 0 & 0 \end{pmatrix} \quad (2.96)$$

In this case, d_{33} component has the highest value of $\approx 25.6 \text{ pm/V}$ (at $\lambda = 1064 \text{ nm}$) [19]. The work discussed in the thesis essentially involves d_{33} component primarily. $LiNbO_3$ is a Raman-active as well as infrared-active crystal. The zone-centre of various optical phonon modes of $LiNbO_3$ could be classified on the basis of irreducible representations *i.e.* into $4A_1 \oplus 5A_2 \oplus 9E$. The A_1 – modes are polarized along z -direction whereas the doubly-degenerate E – modes polarised in the $x - y$ plane. Both the modes are Raman and infrared active whereas the A_2 – modes are silent. Conventionally, a phonon mode could

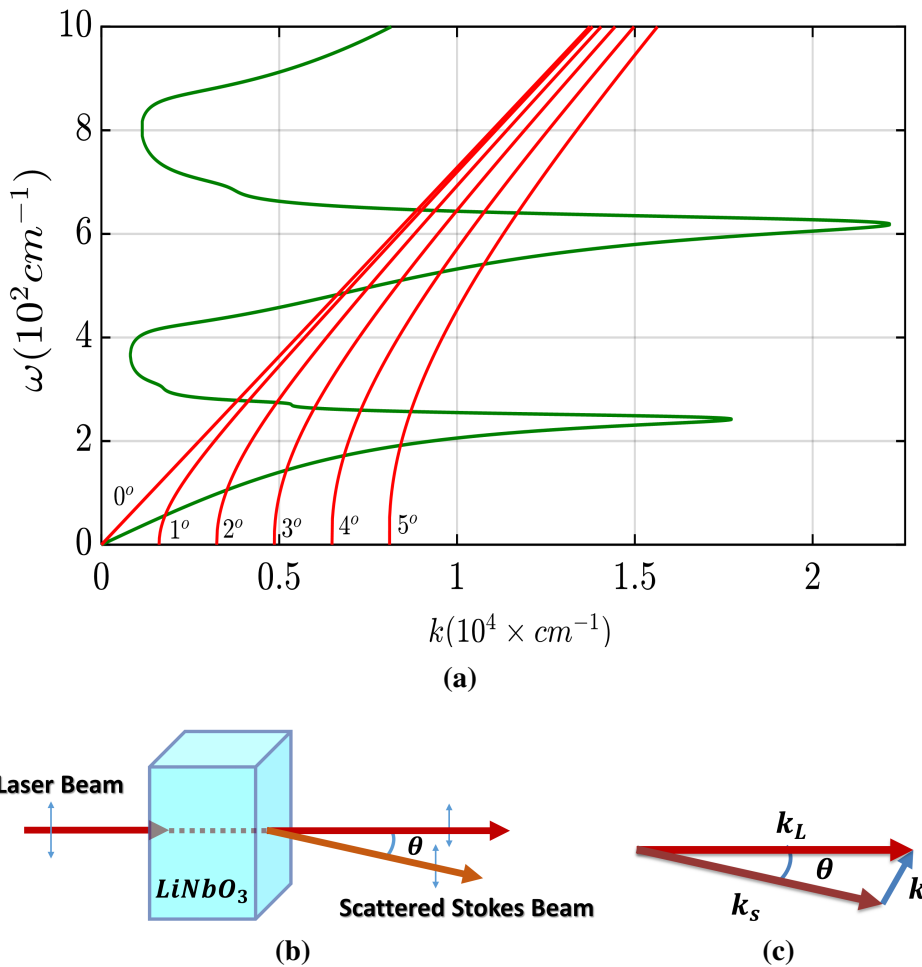


Figure 2.17 (a) Dispersion curve of LiNbO_3 (Green solid line). The red lines are phase matching angles for the pump beam and the Stokes beams. (b) Stokes generation in LiNbO_3 . (c) Wavevectors in Stokes generation.)

be longitudinally optical or transversally optical. A phonon mode is called longitudinal when the polarization vector is parallel to the phonon wavevector k and similarly, it is called transverse when the polarization vector is perpendicular to the phonon wave vector k . LiNbO_3 has several transverse optical modes. Polariton modes are generated when the transverse phonon dispersion and photon (or em) mode dispersion intersect which results in energy being distributed in both mechanical form as well as electromagnetic form. The possibility of generating polariton modes in LiNbO_3 have been utilised for the THz generation [47, 48]. This polariton mode gives rise to cascaded generation by exploiting the $\chi^{(3)}$ nonlinearities. Stimulated polariton scattering (SPS) is a result of this

third order cascaded interaction. In the SPS a stokes radiation gets generated from the interaction of pump photon and the polariton mode which can be represented by

$$\nu_s = \nu_L - \nu_{pol} \quad (2.97)$$

where ν_s , ν_L and ν_{pol} are the stokes, pump and polariton frequencies respectively. In order to achieve the stokes frequencies (ν_s) the polariton frequency (ν_{pol}) must be on the material dispersion curve. The material dispersion can be calculated using [49]

$$\varepsilon = \varepsilon_\infty + \sum_j \frac{S_j \nu_j^2}{\nu_j^2 - \nu^2 + i\nu\gamma_j} \quad (2.98)$$

where ε , ε_∞ are the frequency dependent and independent dielectric constants respectively. And S_j , ν_j , γ_j are oscillator strengths, frequency and the line-width of the j^{th} infrared active mode. As $LiNbO_3$ is uniaxial hence Eq. 2.98 will have two forms corresponding to propagation for $E \perp c$ (ordinary) and for $E \parallel c$ (extraordinary) [50]. For E-symmetry modes the dielectric function will be evaluated from $E \perp c$ whereas with $E \parallel c$ the A_1 -symmetry modes will be evaluated. Considering the values of these parameters from Barker *et al.* [49] we have plotted the dispersion relation for A_1 -symmetric modes which is shown in the Fig. 2.17(a) and represented with the solid green lines. The solid red lines are drawn with help of the phase-matching angle between the incident wavevector and stokes wavevector. This can be understood as follows. When a CW laser beam passes through the $LiNbO_3$ crystal then spontaneous Raman scattering takes place thereby generating stokes beam at an angle of θ . A pictorial representation is given in the Fig. 2.17(b) and 2.17(c) [49–51]. If the incident laser beam has the wave vector k_L and the stokes has k_s then

$$k^2 = k_L^2 + k_s^2 - 2k_L k_s \cos\theta \quad (2.99)$$

here θ is the angle between the pump and the scattered stokes. We have observed the polariton scattering in the $LiNbO_3$ crystal for the generated signal beam. With Eq. (2.99)

a family of curves for various angles can be drawn which intersect the dispersion curve as shown in the Fig. [2.17\(a\)](#).

Chapter 3

High power Mid-IR optical parametric oscillator

This Chapter constitutes the following journal publication:

- **Mukesh Kumar Shukla**, and Ritwick Das, “High-Power single-frequency source in the Mid-Infrared using a singly resonant optical parametric oscillator pumped by Yb-fiber laser”, *IEEE Journal of Selected Topics in Quantum Electronics*, vol. 24, pp. 1-6, Sep. 2018.

3.1 Motivation

Electromagnetic (*em*) spectrum contains huge possibility of procuring the various applications, ranging from meteorology to medicine and communications to entertainment, by offering more and more spectrum. Typically, the *em* frequencies cover lower frequencies ($\approx 3Hz$) to higher frequencies such as Gamma rays ($\approx 300EHz$). This spectrum covers various frequency bands such as radio waves, far infrared (FIR) waves, mid-infrared (MIR) waves, near-infrared (NIR) waves, visible, ultraviolet, x-rays, γ -rays in their ascending order [52, 53]. Mid-infrared and far-infrared frequencies are of prime importance due to the fact that quite a few organic species exhibit strong absorption in these bands.

Conventionally, 2 – 5 μm band of the *em* spectrum is known as the mid-infrared (MIR). The MIR is very useful to characterise the organic as well as gaseous molecules as they show their detectable spectroscopic features within this band [54]. This enhances the demand of tunable MIR laser sources. However, in order to perform quantitative measurements as per described by Tittle *et al.* [55], an ideal MIR tunable laser source needs to have the following features,

- Enough optical power
- Narrow line-width
- Single longitudinal mode operation
- Rapid wavelength tunability

All the above-mentioned features in the laser source affect the spectroscopic measurements in some way or the other. For example, narrow linewidth with a single longitudinal mode operation, is essential for high selectivity and sensitivity. In addition, fast wavelength tunability is required for fast response and high data acquisition. These kind of sources are of great importance for the remote sensing as well as optical metrology. They are useful in these scientific areas as they did not interact with the ambient conditions [56, 41, 57]. From end-user perspective, laser diodes are most widely available and practical coherent sources used for spectroscopic applications. In the MIR there is complete lack of presence of high power diode lasers which is basically due to the high gain material unavailability. Still the laser makers are clueless in this area and a lot of efforts are going on. There are primarily two diode laser sources for MIR which are listed below

- Quantum cascade lasers (QCLs)
- Lead salt diode lasers (LSDL)

The QCLs generate coherent mid-IR radiation using intra-band transitions. Their average output power are of the order of few *milliWatts* resulting in very low wall-plug efficiency. Such low average power limits their use as potential candidate for few spectroscopic

experiments [58, 59]. However, they cover a wide range in the MIR band *i.e.* $3.5 - 17\mu m$. Also, the tunable wavelength is limited by a few cm^{-1} for one device. LSDLs also cover $3 - 30\mu m$ *em* spectrum band. They are usually called lead salt as many of the compounds contains lead. Mainly they belongs to the IV-VI alloys of the modern periodic table. Butler *et al.* were the first to demonstrate the LSDL from lead telluride (PbTe) [60]. LSDLs usually provide a mode-hop-free tuning which is limited by $\approx 1cm^{-1}$ [54, 61, 62]. Their main drawback lies in the fact that for CW operation cryogenic cooling is required which makes them costly. The average power of LSDLs are typically limited to around $0.1mW$ [55, 54].

Although, there has been tremendous impetus on the development of modern generation lasing materials, the *em* spectrum band $2.8 - 4\mu m$ has still remained broadly inaccessible. In addition, the lasing medium with high gain cross-sections for the MIR band region $2.8 - 4\mu m$ exhibit poor optimal thermal stability [63, 64]. However, non-linear optical crystal based optical parametric oscillators (OPOs) provide a plausible platform to harness this gap of the *em* band with appreciable tunability and throughput power. Periodically poled $LiNbO_3$ (PPLN), which has wide transparency range and high thermal stability in MIR band, is a promising candidate for an OPO design. As discussed in chapter 2, the beam quality and the output power of OPO depends on the pump laser. In conjunction with modern generation robust fiber lasers as pumping systems, the PPLN based OPOs are a highly reliable coherent source in the MIR. The PPLN based OPOs can cover $3.0 - 5.5\mu m$ band by virtue of wide transparency range and temperature dependent refractive index [65].

The absorption in the PPLN increases substantially above $3.8\mu m$ wavelength [66]. This is the main challenge for the PPLN OPOs to generate high power CW MIR. Herpen *et al.* were the first to report a high power MIR of $1.2W$ at wavelength of $3.9\mu m$. And this was the maximum in ring cavity OPO. They have utilised a $50mm$ long PPLN crystal which in turn limits the maximum generation of the idler. Also they did not apply any thermal management schemes to overcome the thermal-loading in the PPLN crystal. A

rapid tuning in the wavelength band $2.67 - 4.34 \mu\text{m}$ is shown by Silva *et al.* with a tunable pump source which is master-oscillator power-amplifier (MOPA) based on Yb-doped fiber [67]. On the average power scale the power in the MIR is not appreciable by them. With a titanium sapphire ($Ti : Al_2O_3$) laser as pump source which is tunable across 775 to 860 nm Siltanen *et al.* has demonstrated a maximum of 0.8 W source in the MIR [68]. They have used the PPLN crystal for their study in a ring cavity configuration. With a series of experimental demonstrations Henderson *et al.* have shown the applications of the PPLN OPOs in trace gas detection as well as in absorption spectroscopy [69–71]. Their OPO is tunable in the $2.4 - 3.5 \mu\text{m}$ range. At $2.6 \mu\text{m}$ they have achieved a idler power of 4.5 W by pumping it at 15 W. The observed idler is of good beam quality. However, they did not venture deeper into the MIR band which is a fingerprint region for quite a few organic molecules. In an attempt for the spectroscopic sensing Vanio *et al.* has reported the phenomenon of optical bi-stability as well as thermal self locking [72]. They have also utilised a PPLN based CW OPO at low pump powers. A 4.1 W of average power at $3.2 \mu\text{m}$ is reported by Devi *et al.* with a 48 mm long PPLN crystal [73]. They have utilised a 6-mirror cavity in the ring configuration. They have not attempted the higher tuning in the MIR as they have mainly focused on making a signal beam frequency doubled SRO. In another attempt to find maximum idler power Sowade *et al.* has iterated that parametric gain and cavity losses need to be adjusted for optimized generation [74]. They observed that with an optimized cavity 1.5 W of idler power at $3.2 \mu\text{m}$ can be achieved even with a 25 mm long PPLN rather than using a 50 mm long PPLN. They have reported that the idler gets saturated in 50 mm long crystal providing only 0.5 W idler power. There have been also some attempts with different crystals such as chalcopyrite *e.g.* $ZnGeP_2$ to generate high power CW radiation around $4 \mu\text{m}$ but their conversion efficiencies are relatively too low in comparison with the PPLN SROs [75]. An intra-cavity MIR generation has been reported by Sheng *et al.* [76]. For this they kept the PPLN crystal inside a $Nd:YVO_4$ laser cavity and generated 1.43 W power at $3.6 \mu\text{m}$. The cavity in this work is a shape of ‘ Λ ’. However, the quality of the generated idler is

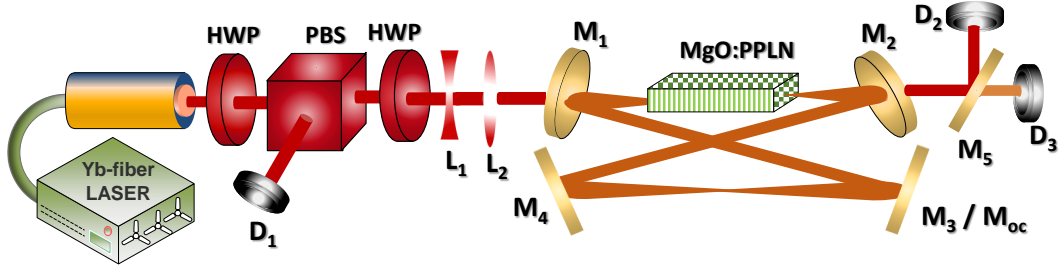


Figure 3.1 Experimental set-up of 4-mirror SRO in ring cavity configuration \Rightarrow HWP: half-wave-plate, PBS: polarizing-beam-splitter, L_1 : diverging lens ($f = -75$ mm), L_2 : converging lens ($f = 100$ mm), $M_{1,2}$: concave mirrors with radius of curvature $R = -200$ mm, $M_{3,4,5}$: plane mirrors, M_{oc} : out-coupling mirror, and $D_{1,2,3}$: Thermal detectors.

relatively poor as it exhibit a $M^2 \approx 4$ which basically because of the pump beam quality and the cavity configuration.

In this chapter, we discuss and describe our demonstration of a SRO. The fundamental pump source for this SRO is a Yb-fiber laser and the crystal is a 8 cm long MgO:PPLN which is kept symmetrically in a 4-mirror ring cavity. We have demonstrated high spectral and spacial quality idler beam which is tunable MIR above $> 3.8 \mu m$.

3.2 Experimental Set-up

3.2.1 Laser and beam focusing

In the experiment, we have used a 40 W CW Yb – fiber laser (IPG Photonics, YLR-40-1064-SF). The laser is linearly polarized with a nominal line-width of $\approx 100 kHz$ and $M^2 = 1.05$. A schematic of the set-up is shown in the Fig. 3.1. A variable attenuator which is made up of a combination of half-wave-plate (HWP) and polarizing-beam-splitter (PBS) is employed for managing the power incident on the nonlinear crystal. A second HWP is utilised to get the appropriate polarization of pump beam for the phase-matching of interacting waves within the nonlinear crystal. In order to obtain maximum efficiency of frequency conversion, we adopt the recipe prescribed by Boyd and Kleinman for attaining optimum beam waist. According to their theoretical prediction, the optimum

Table 3.1 Reflectivity and transmission characteristics of mirrors used in the SRO

Mirrors	Reflectivity	Transmission
$M_{1,2,3,4}$	$\geq 99.5\%$ (1350 – 1650 nm)	$\geq 99.7\%$ (1064 nm) $\geq 95\%$ (2900 – 4500 nm)
M_5	$\geq 99.7\%$ (1064 nm) AOI* : 45°	$\geq 90\%$ (2500 – 4500 nm) AOI* : 45°
M_{oc}	$\geq 95\%$ (1350 – 1650 nm)	-

*Angle of incidence

beam waist is achieved when the focusing parameter is $\xi = 2.84$. Here, $\xi = \frac{L}{kw_0^2}$ where L is the length of the nonlinear crystal, k is the propagation vector and w_0 is the pump beam waist at the centre of nonlinear crystal. For achieving $\xi = 2.84$ in 80 mm long MgO:PPLN crystal at $\lambda = 1064$ nm pump wavelength, the beam waist should be 47 μm . At such small beam waist, a possible thermally induced breakdown in the crystal is anticipated at high pump powers [44]. In order to avoid the thermal manifestations as well as catastrophic damage to the nonlinear crystal, we have chosen a broader beam-waist of 75 μm for the pump beam and accordingly $\xi \approx 1$ [77, 71]. This is achieved using a combination of concave and convex lens of focal lengths $f = -100$ mm and $f = 100$ mm respectively.

3.2.2 Cavity

The SRO cavity is a ring cavity of four mirrors where two inline mirrors are concave and the other two are plane. All the mirror specifications are given in Table 3.1. The 4-mirror ring cavity is 886 mm long and it has a finesse of 311. In order to separate the pump beam from the idler we have used the a dichroic mirror M_5 whose specification is also mentioned in the Table 3.1.

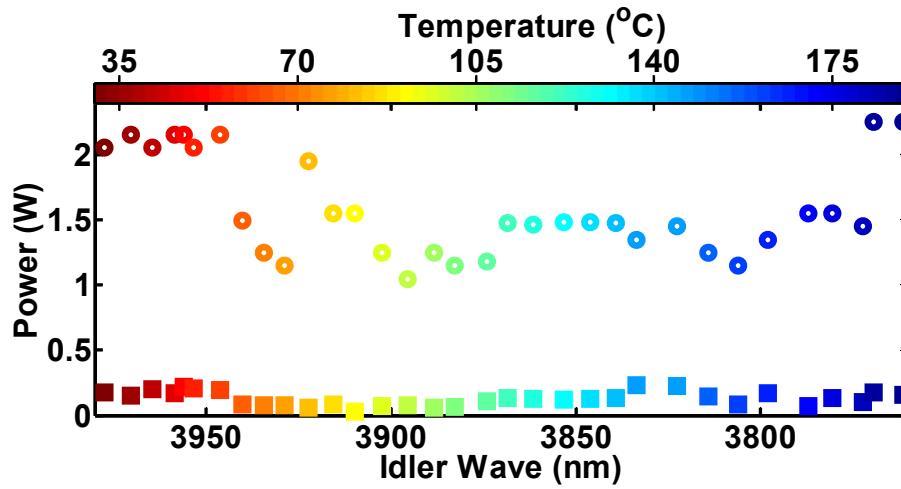


Figure 3.2 Variation of threshold power (circle) and idler power (square) with idler wavelength when the temperature of the PPLN crystal is varied from 30°C – 190°C.

3.2.3 Nonlinear Crystal

The nonlinear crystal utilised in this work is $LiNbO_3$. In order to avoid photo-refractive damage the crystal is 5 mol% magnesium oxide (MgO) doped and for satisfying the QPM condition it is periodically poled. The crystal is 80 mm long 6.9 mm wide and 1 mm thick. This crystal is popularly abbreviated as MgO:PPLN. This has multiple grating-periods (Λ). All the gratings are for the MIR generation so they are in the range $\Lambda = 28.5 - 31 \mu m$ with steps of $0.5 \mu m$ with total 7 QPM periods. It is made from HC-Photonics, Taiwan. The crystal is kept on an oven in order to vary its temperature. The temperature of the oven can be varied from 20°C to 200°C in precision of 0.1°C. For an efficient heat extraction the crystal faces are in direct contact from three-sides with a home-made brass heat sink [78]. The two faces of the crystal which is exposed with laser are anti-reflection coated for the pump beam 1064 nm ($R < 3\%$), signal band which is 1350 – 1700 nm ($R < 0.5\%$) and for the idler band 2500 – 4500 nm ($R < 10\%$).

3.3 Results and Discussion

3.3.1 Signal and idler tuning

For MIR generation in SRO, we have used the $\Lambda = 29 \mu m$ grating-period of the MgO:PPLN. We have performed a near threshold temperature tuning of the SRO. The threshold along with the generated idler power as a function of temperature and wavelength is shown in the Fig. 3.2. It is interesting to note that we obtained a minimum threshold of $\approx 1 W$ at $T = 100^\circ C$. This corresponds to an idler wavelength of $3895 nm$. The SRO provides idler power in the range of $26 - 200 mW$ at this near threshold temperature tuning. This much of idler, in such tuning window is varying in the range of $\lambda_i = 3760 - 3970 nm$. This much idler power is sufficient for spectroscopic as well as some bio-photonic applications. The abrupt variation in threshold pump power with the temperature along tuning range is a consequence of three main wavelength dependent factors which are listed below:

- Absorption in the crystal
- Reflectivity of crystal AR coatings
- Reflectivity of the mirrors

Vanio *et.al.* have measured the transmission of a $50 mm$ long MgO:PPLN crystal using FTIR spectrometer [72]. This data shows that the crystal transmission varies from 0.81 to 0.62 for $3760 nm$ to $3970 nm$. Such a significant drop in the transmission increases the threshold power close to $3970 nm$ wavelengths which we have also observed as shown in the Fig. 3.2. However we have also observed two high threshold data points close to $3760 nm$ which can not be explained by this transmission plot. The crystal AR coatings as well the mirror reflectivities plays a crucial part here as they do not show uniform variation over the signal and idler wavelength band.

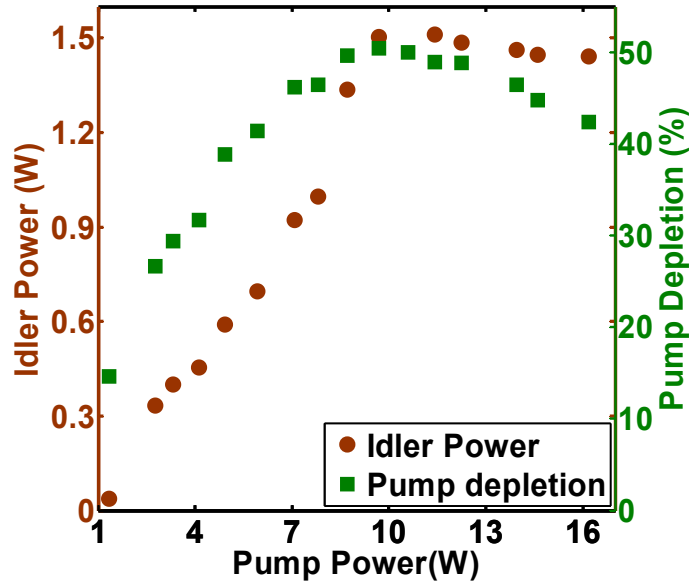


Figure 3.3 Measurement of the idler power (P_{idler}) and corresponding pump depletion with variation of the pump (P_{pump}). A maximum $P_{idler} \approx 1.6$ W was observed at $P_{pump} \approx 10$ W and maximum pump depletion was $\approx 50\%$.

3.3.2 Power scaling at $T = 100^{\circ}C$ and $P_p = 16$ W

These factors mentioned above turn more critical at higher pump powers (P_{pump}). In order to perform the power scaling we fixed the pump at 16 W of power. And then by continuously changing the temperature of the crystal oven from $30^{\circ}C$ to $190^{\circ}C$ we measured the corresponding idler power. This in turn provide us a wide high power tunability in the idler. We observed that the idler power maximizes at a PPLN crystal oven temperature of $100^{\circ}C$ and giving $P_{idler} = 1.6$ W. At this temperature, the wavelength of the idler was $\lambda_i = 3895$ nm. We observed the same variation in the idler power (P_{idler}) with the change in the temperature as the threshold which is plotted in the Fig. 3.2. In order to verify this much of P_{idler} at 16 W P_{pump} and at $100^{\circ}C$ temperature we performed the power scaling by changing the pump power from the threshold to 16 W. It is plotted in the Fig. 3.3. We found that the maximum idler $P_{idler} = 1.6$ W was observed even at a low power $P_{pump} \approx 10.6$ W. And a further enhancement in the P_{pump} results in the reduction of the generated idler (P_{idler}). In order to verify it we have plotted the pump depletion along with the fundamental P_{pump} . Pump depletion (P_{dep}) is usually represented

in %. It is the ratio of the left-out P_{pump} to the incident pump power. Left-out or residual pump power is the measured pump power at the idler and pump separating mirror M_5 with the detector D_3 as shown in the Fig. 3.1. The variation in the P_{dep} in the Fig. 3.3 is in complete agreement of the idler saturation at high pump powers. It can be observed from this figure that at 9.7 W of P_{pump} the P_{dep} starts to decrease. We attribute this kind of behaviour of the idler (P_{idler}) to the high intra-cavity signal power. The high reflecting mirrors of the cavity enhances the Q of the SRO. This in turn increases the thermal loading at the nonlinear crystal and it is mostly affected by the oscillating high power signal. At such high cw pump powers, the nonlinear crystal has temperature gradient in the propagation direction as well as transverse direction which could be attributed to linear as well nonlinear absorption by $LiNbO_3$. Such a temperature gradient profile within the crystal adversely affects the phase-matching. Therefore, a theoretical model to describe the observed results would essentially comprise of the solution of three-dimensional scalar wave equation in conjunction with heat-diffusion equation taking appropriate boundary conditions dictated by oven boundaries and ambient temperature. This would essentially provide a temperature profile which would eventually, govern the nonlinear optical interaction via the phase-matching condition. It is apparent that this process of providing a theoretical model is computationally intensive and hence, it is beyond the scope of present thesis.

3.3.3 Signal Spectrum

The signal spectrum recorded at a $P_{pump} = 16$ W is accompanied by a few additional peaks instead of having only signal. This is shown in Fig. 3.4(a). This spectrum is measured at a crystal temperature of $100^\circ C$ ($\lambda_i = 3895$ nm). Such peaks have been observed previously for idler wavelengths of ≤ 3.5 μm and their origin is attributed to the stimulated Raman scattering in $LiNbO_3$ [79–81, 30] owing to the smaller number of sidebands. However, as we described in the chapter 2 (2.15) that the $LiNbO_3$ is both Raman and infrared active.

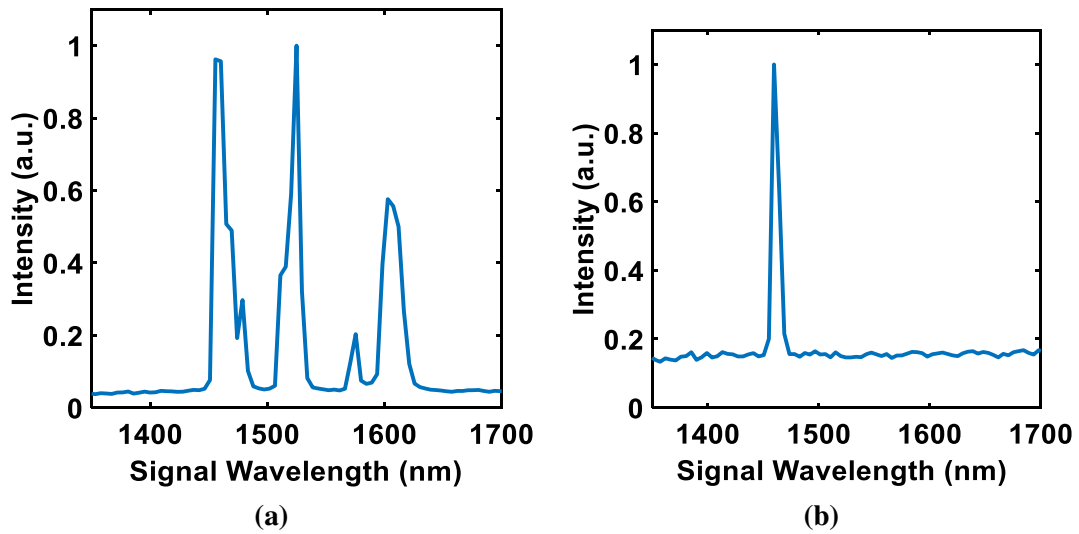


Figure 3.4 (a) Measured spectra of the oscillating signal in the high Q 4-mirror ring SRO. The generated modes (side-bands) are attributed as the stimulated polariton scattering. (b) Signal spectra measured for the low Q -cavity (OC-SRO).

The observed extra side bands in the signal spectra can not be explained by the stimulated Raman scattering as depicted by the Mills *et al.* [51]. We attribute this observation of multiple side bands to the stimulated polariton scattering (SPS) in MgO:PPLN. These polariton modes arise as a consequence of interaction of high power signal with the Raman and *IR*-active modes of MgO:PPLN [50, 82]. This could be appreciated by noting the dispersion curve of $LiNbO_3$ which is plotted in chapter 2 (Fig. 2.17a). When the dispersion curve intersects the phase-matching curve for $LiNbO_3$, polariton modes could be generated at moderate pump powers. The direction of propagation of polariton modes is dictated by the respective phase-matching condition. In order to appreciate the origin of such modes, we have measured the frequency shifts with respect to the signal peak. In our case, as shown in the Fig. 3.4(a) we attribute the frequency shifts to stimulated polariton scattering (SPS). The polariton modes are shifted by 86 cm^{-1} , 291 cm^{-1} , 501 cm^{-1} , and 610 cm^{-1} with respect to generated fundamental signal. The 86 cm^{-1} , 501 cm^{-1} , and 610 cm^{-1} shifts corresponds to the phase-matching angles (between signal-mode and stokes-mode) of 1.6° , 3.5° , and 12.8° respectively which could be ascertained using Fig. 3.5a. However, the shift of 291 cm^{-1} does not satisfy any phase matching angle and

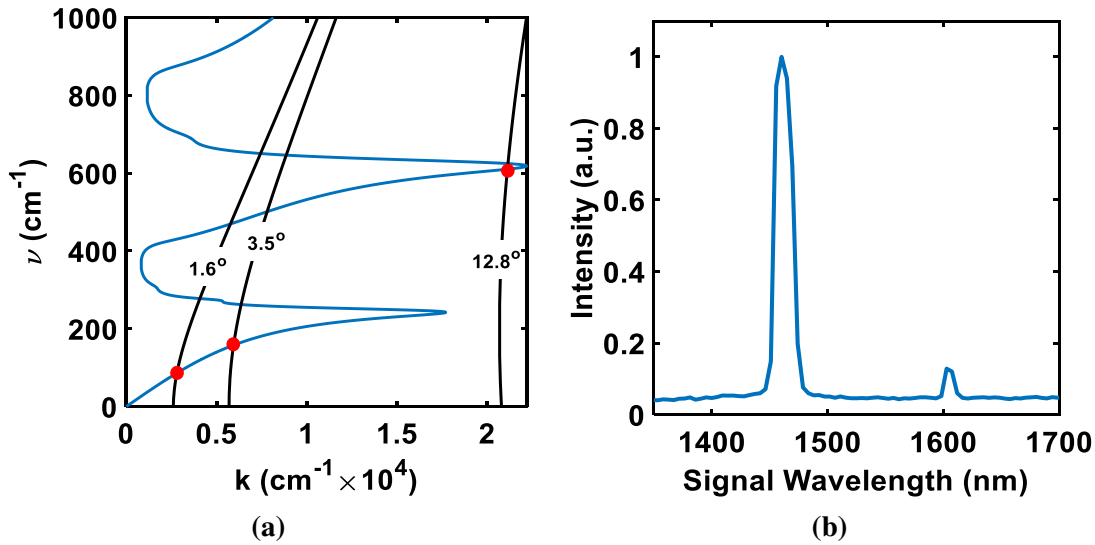


Figure 3.5 The solid blue line indicates dispersion i.e. wavevector (k) vs frequency plot of LiNbO_3 crystal. The black are the phase-matching curves having angles 1.6° , 3.5° , and 12.8° respectively. The red dots indicate the generated polariton modes for corresponding wavelength shifts from signal.

hence it can not be explained by this process. It can also be noted here that the shifted peak at 291 cm^{-1} could not be attributed to Raman scattering as per the Raman spectrum (for LiNbO_3) provided by Barker *et al.* [49]. Interestingly we also observe that these SPS modes are able to oscillate even at low pump powers such as $\approx 3.5 - 4 \text{ W}$ which is shown in the Fig. 3.5b. It means that the gain of the crystal for these modes overcome the losses of the cavity at such power levels. Further, as we increase the pump power, the number of side-bands increase e.g. at $\approx 7 \text{ W}$ pump power, we observe two modes which escalates to four at $\approx 16 \text{ W}$ of pump power. Also, it is worthwhile to note that the side-band intensities increase as the incident pump power goes above 4 W . Although we could not measure the spectra of the idler, it is straightforward to infer that the presence of the SPS will also lead to the multimode idler spectrum.

3.3.4 Signal out-coupling in SRO and temperature tuning

The motive of this work was to generate high power single frequency MIR radiation. In order to generate single-frequency signal and hence, the idler, we replaced the plane

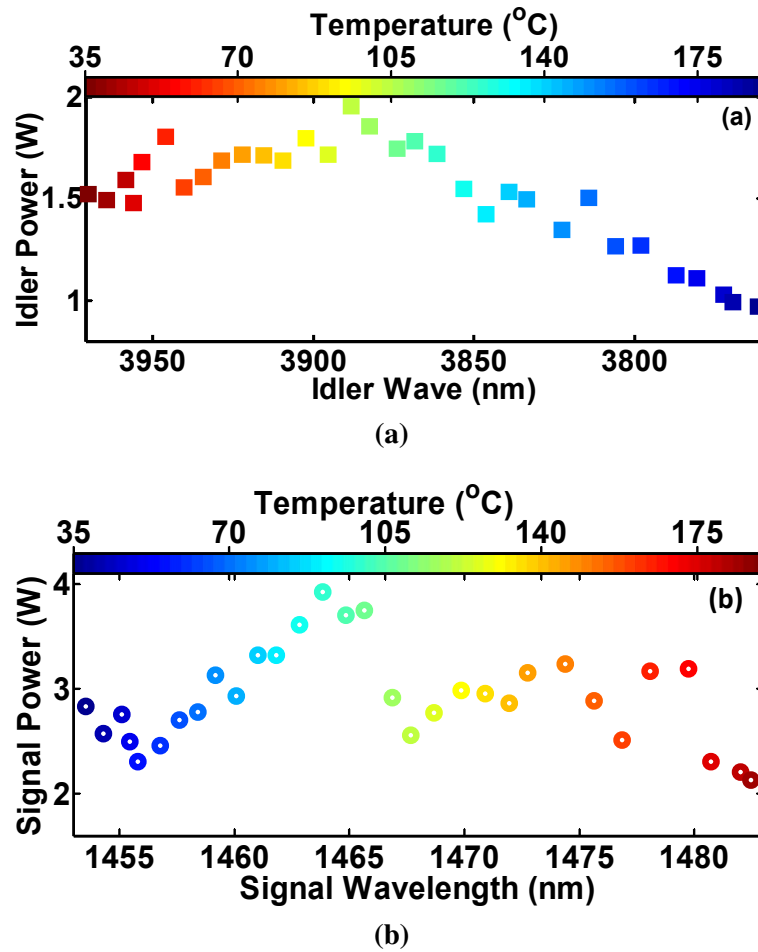


Figure 3.6 In OC-SRO case (a) the idler power (P_{idler}) and the (b) signal power (P_{signal}) along with their respective wavelengths when the temperature of the crystal-oven is continuously changed from 35°C to 190°C at $P_{pump} = 16\text{ W}$.

mirror M_3 as depicted in the Fig. 3.1 with another plane mirror M_{oc} . The mirror M_{oc} is a out-coupling mirror for the signal *i.e.* for the wavelength band $1350 - 1650\text{ nm}$. Its reflectivity is only 95% for this signal band and hence, it transmits the rest 5% intra-cavity signal. Due to 5% out-coupling of the signal, the overall pump threshold power for out-coupled SRO (OC-SRO) increased to 7 W . This additional loss (5% out-coupling) also lowers the finesse for the OC-SRO cavity at the signal wavelength. Consequently, the polariton modes are unable to survive within the cavity. The signal spectrum in this case does not contain any side bands as shown in the Fig. 3.4(b). This also manifests into a significant signal power leaking out of M_3 . Further, at $P_{pump} = 16\text{ W}$ we performed the temperature tuning of the OC-SRO. The crystal oven temperature was varied from

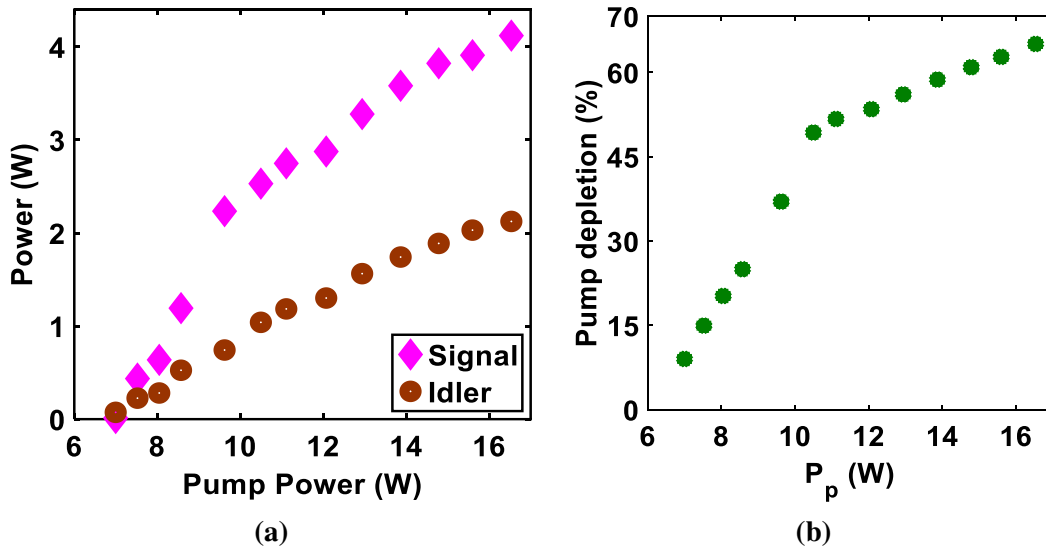


Figure 3.7 (a) Measurement of the idler and signal powers along with the variation of the pump power in OC-SRO design at a temperature of 100°C . (b) Measured pump depletion along with the change in the pump power (P_p).

35°C to 190°C . This in turn provided us a continuous wavelength tunability of the idler band as well as in the signal band. The signal is tunable from 1453 nm to 1484 nm and correspondingly, the idler gets tuned from 3970 nm to 3761 nm . This tunability of the idler and the signal is represented in the Fig. 3.6(a) and 3.6(b) separately. We observed a maximum idler power of $P_{idler} = 2\text{ W}$ at a idler wavelength 3895 nm . At this point the temperature of the crystal is 100°C . This much of idler power in the MIR close to this wavelength is the maximum till now from a PPLN based ring cavity CW SRO. However, because of the out-coupling we observed a maximum signal $P_{signal} = 4\text{ W}$. This is at a signal wavelength $\lambda_s = 1464\text{ nm}$ and the temperature is the same 100°C . In order to recheck it we have performed the power scaling of the OC-SRO at a temperature of 100°C . It can be seen in the Fig. 3.7(a) that the threshold is close to 7 W for the OC-SRO configuration. And at high pump powers the signal and idler powers both tend to saturate. It can be inferred from this behaviour that at this much of P_{pump} thermal dephasing is taking place resulting in a lesser parametric gain.

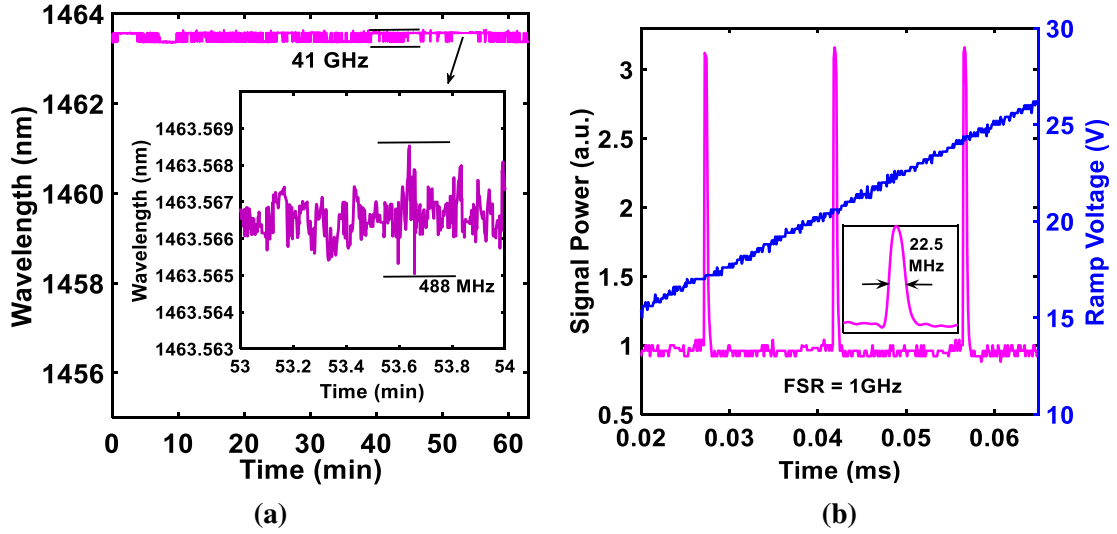


Figure 3.8 (a) Wavelength fluctuation measured with wavemeter (HighFinesse). The peak-to-peak fluctuation in the signal beam was 41 GHz for ≈ 1 – hour. And for one minute it is 488 MHz. (b) FPI measurement confirms the single frequency operation and the measured line-width is 22.5 MHz.

3.3.5 Signal frequency characteristics

In order to measure the wavelength fluctuation in the OC-SRO case we have utilized a wavemeter made of Angstrom (HighFinesse, Russia). The resolution of this wavemeter is ≤ 30 MHz. We recorded the leaked out signal from the mirror M_3 in this wavemeter when the SRO is 16 W of pump. The fluctuation in the frequency is plotted for 1 – hour in the Fig. 3.8(a). It can be seen in this figure that the peak-to-peak fluctuation in the wavelength is ≈ 41 GHz for this much time. In the inset of the Fig. 3.8(a) we have extracted out one minute of data from the same graph. We found that between 53 – 54 min the frequency fluctuation of the SRO is 488 MHz. These frequency fluctuation can be actively improved if some locking mechanisms such as the techniques used by Mhibik *et al.* [83] be utilised. Mode-hopping can be easily controlled through inserting an etalon. However this will increase the threshold a bit more. The signal frequency fluctuation can also be improved by controlling the ambient conditions and isolating the total system.

We have also measured the line-width of the signal of the OC-SRO at $P_{pump} = 16$ W. We utilized a scanning Fabry-Perot etalon (FPI) (FPI-100, Toptica) for this measurement.

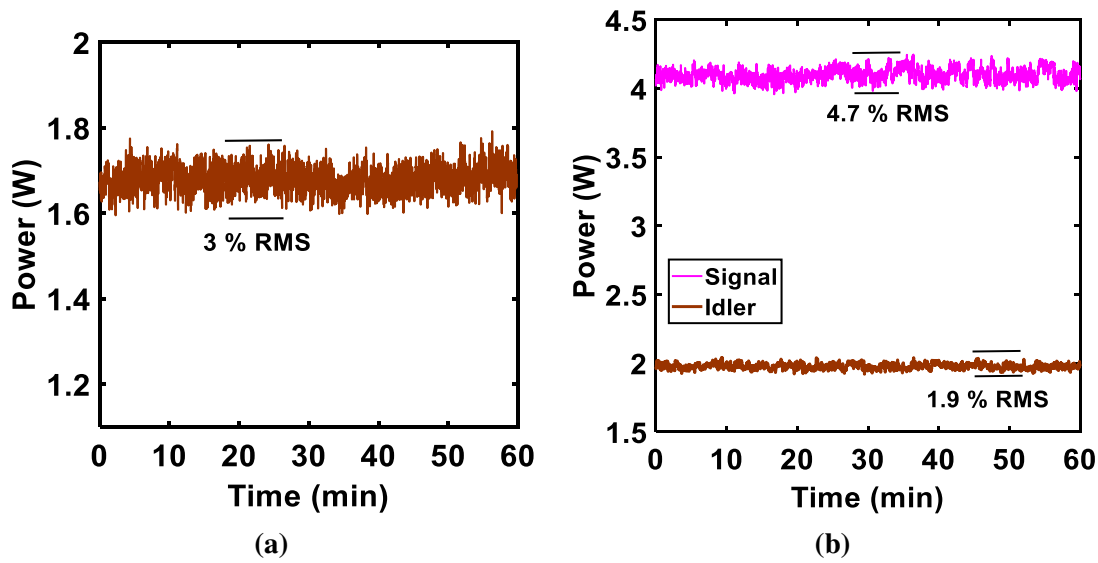


Figure 3.9 Peak-to-peak fluctuation, which is given in the RMS (root mean square), in the power of the (a) idler in the SRO and (b) signal as well as idler in OC-SRO design for ≈ 1 – hour.

The free spectral range (FSR) of this FPI is 1GHz and its finesse ≥ 400 for the entire signal band. The measured spectra of the FPI is shown in the Fig. 3.8(b). It can be seen that all the FPI peaks are equidistant and of equal height. This is the confirmation of the single mode operation. We have calculated the linewidth of one of the peaks by taking Lorentzian lineshape into consideration. It is shown in the inset of the Fig. 3.8(b). This measurement yielded a line-width of $\approx 23\text{MHz}$. The signal linewidth is much larger as compared to the pump linewidth which is $\approx 100\text{kHz}$. This is primarily due to lower finesse of the OC-SRO cavity which is ≈ 95 .

3.3.6 Power-stability

In order to demonstrate a high power laser source its power has to be stable over time. For this we recorded the MIR idler power in SRO as well as in the OC-SRO configuration. And also measured the peak-to-peak variation of the out-coupled signal in the OC-SRO case. We recorded both for 1 – hour when the crystal oven temperature was 100°C and the pump power $P_{\text{pump}} = 16\text{W}$. In Fig. 3.9a we have plotted the signal and idler power for SRO case whereas in Fig. 3.9b the OC-SRO case. For the SRO it can be seen that

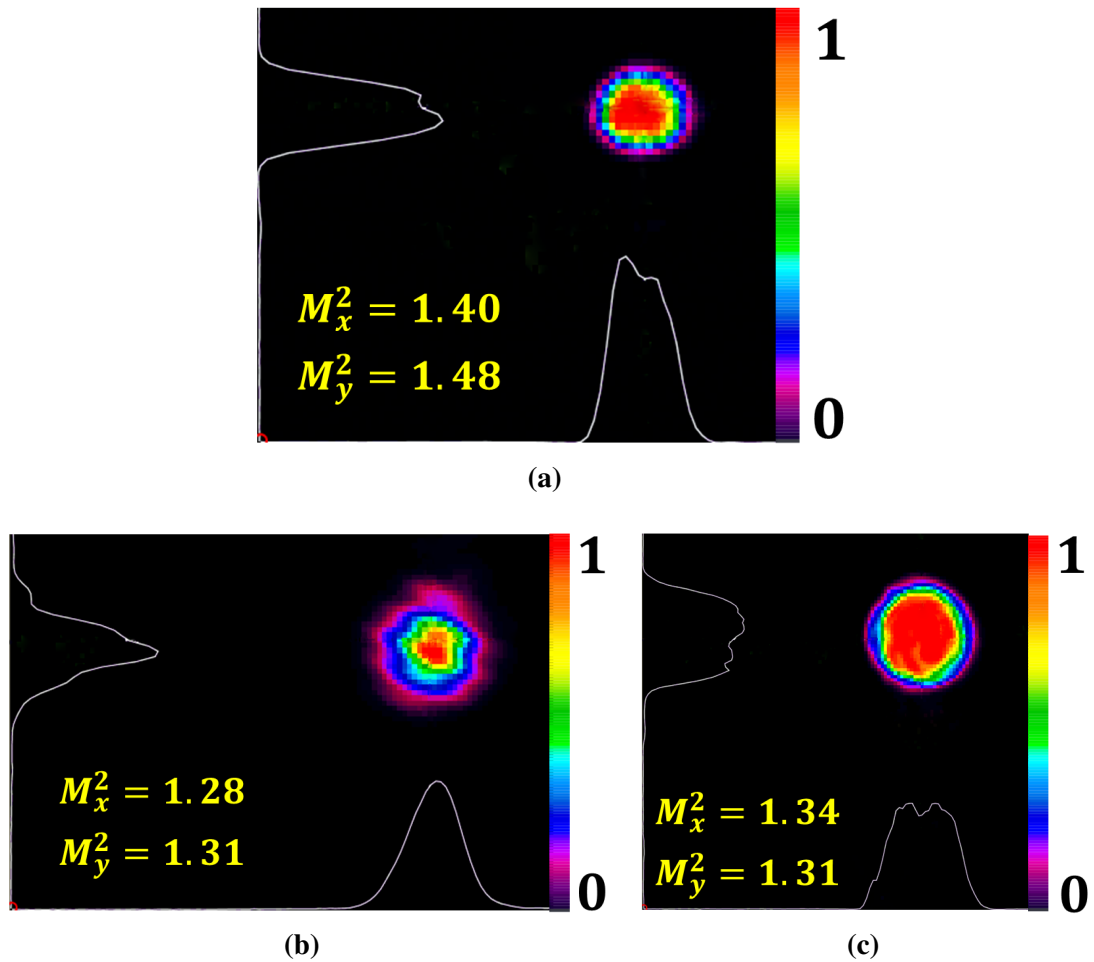


Figure 3.10 Transverse intensity beam profiles depicting the Gaussian TEM_{00} mode. (a) The idler beam profile in SRO. (b) The signal beam in the OC-SRO. (c) The idler beam in the OC-SRO configuration. The respective M^2 values are shown on the figures.

the idler power has a peak-to-peak fluctuation of 3% RMS for ≈ 1 – hour. Similarly in the case of OC-SRO the peak-to-peak variation in the signal and idler powers are $\approx 4.7\%RMS$ and $\approx 1.9\%RMS$ respectively. This indicates an improvement of $\approx 60\%$ in the idler power variation in the OC-SRO case. We attribute this to the out-coupling mirror which lowers the thermal loading on PPLN crystal and thereby increases the power stability in the MIR which has immense applications in the remote sensing.

3.3.7 M^2 and beam profile

By utilizing a thermal imaging camera (PYROCAM-III, Spiricon, USA) we have measured the transverse beam profiles of the signal and idler. For the idler we recorded its profile for both the configurations namely SRO and OC-SRO. Fig. 3.10(a) indicates the idler profile for the SRO configuration. This profile of the Gaussian beam confirms its TEM_{00} mode profile. The M^2 measurement was performed with the scanning beam profiler (NanoScan, Ophir, USA) and its method is given in the Appendix B. We measured the $M_x^2 \leq 1.40$ and $M_y^2 \leq 1.48$ for the idler beam in SRO configuration. The Fig. 3.10(b) represents the beam profile of the signal in the OC-SRO design. It is also a Gaussian beam in the TEM_{00} mode. M^2 values for the signal in this design are $M_x^2 \leq 1.28$ and $M_y^2 \leq 1.31$. And Fig. 3.10(c) is the temporal beam profile of the idler in the OC-SRO design. In this configuration the idler has $M_x^2 \leq 1.34$ and $M_y^2 \leq 1.31$. An improvement in the M^2 values of the idler beam can be easily observed. We attribute this to the design of the OC-SRO. This configuration allows efficient thermal management in terms of the out-coupling mirror. Although it can be noted that the absorption in PPLN increases close to $4 \mu m$.

3.4 Conclusion

In conclusion, this chapter describes the demonstration of a CW high-power NIR and MIR source. The SRO is pumped by high power Yb-fiber laser. It is single-frequency and can be tuned over signal as well as idler bands by varying the temperature of the crystal. Initially we observed multimodal signal which we attributed to the stimulated polariton scattering in the $LiNbO_3$. In order to suppress these additional modes we utilised the OC-SRO configuration by replacing one of the cavity mirror with a out-coupling one. In the OC-SRO design, we have reported a maximum idler power of $P_{idler} = 2 W$ at $3895 nm$ and a maximum signal power of $P_{signal} = 4 W$ at $1464 nm$. Additionally, this

configuration expands the frequency tunable range of SRO along with improved spatial as well as spectral qualities of output beam. The tunability of the SRO can be further expanded in the MIR by utilizing the other grating periods of the same crystal such as $28.5 \mu\text{m}$, $29.5 \mu\text{m}$. These observations suggests that in the OC-SRO design a better MIR idler beam can be recorded. This is primarily due to lesser thermal loading in the OC-SRO than the SRO design. Of course the MIR idler beam quality can be made better by optimal design of the crystal oven. This in turn will lower the thermal load on the nonlinear crystal.

Chapter 4

Intra-cavity tunable SHG from Yb-fiber laser pumped PPLN SRO

This Chapter constitutes the following journal publication:

- **Mukesh K Shukla**, Partha S Maji, and Ritwick Das, “Yb-Fiber laser pumped high-power, broadly-tunable, single-frequency red-source based on singly-resonant optical parametric oscillator”, *Optics Letters*, vol. 41, pp. 3033-3036, Jun. 2016.

4.1 Introduction

High-power, CW, selectively tunable and spectrally-pure light sources in the visible spectrum of red region are important for various applications in bio-photonics such as confocal microscopy, flow cytometry, selective fluorophore activation and excitation[22–24, 84]. Such light sources form crucial ingredient as excitation sources in various spectroscopic techniques including Raman spectroscopy and coherent anti-stokes Raman spectroscopy (CARS). For example, a conventional green (532nm or 514nm) excitation results in a fluorescence spectrum extending over a broad spectral band and thus, tends to eclipse the Raman signal. In order to retrieve the Raman stokes spectrum, sophisticated detection schemes needs to be invoked. On the other hand, an excitation source in

$\approx 700 - 800 \text{ nm}$ band would result in exclusive Raman signal which would eventually lead to simpler detector configuration [25, 85]. Tunable red and NIR sources are also excellent candidates for selectively exciting molecular species where the intrinsic absorption is minimum [86]. To this end, most reliable and popular optical sources generating tunable coherent radiation in $700 - 800 \text{ nm}$ band is *Ti:sapphire* laser which necessarily requires complex and expensive high-power green pump sources with optimum beam quality [87, 88]. *Ti:sapphire* laser offers continuous tunability in $700 - 1100 \text{ nm}$ band with desirable spectral and spatial features of NIR beam. However, red/NIR output power is primarily limited by thermal loading of *Ti:sapphire* crystal at high pump powers [89]. In addition, the deployment of green pump source reduces the wall-plug efficiency substantially. Periodically-poled *LiTaO₃* (PPLT) based SROs form a plausible alternative to *Ti:sapphire* lasers delivering excellent spectral beam quality [90, 91]. However, PPLT-based SROs also require a high-power pump in green (532 nm) with relatively good beam quality which increases the system complexity and adversely affects overall efficiency. The red laser diode bars deliver high-power red/NIR radiation with improved wall-plug efficiency. However, diode-laser based configurations exhibit poor spatial beam quality as well as noisy temporal behaviour. In order to improve the output features of red/NIR diode laser panels, active stabilization techniques in conjunction with beam reshaping schemes have been deployed which renders such systems technologically as well as economically expensive [92].

Recently, a few novel configurations based on intra-cavity frequency-doubling of *LiNbO₃* based SROs or *LiTaO₃* based SROs have emerged as potential competitors for generating high-power tunable radiation in any desirable band by virtue of extremely wide bandwidth offered by parametric generation process. Such schemes have proven to deliver excellent spatial beam quality with high spectral purity. In conjunction with the deployment of high-power NIR fiber-laser based pump sources, intra-cavity frequency-doubled SROs significantly increase the overall efficiency and thus reduce the operational cost. Amongst periodically-poled crystals for continuous-wave high-power SRO, *LiNbO₃*

is the most preferred choice when pumped by NIR sources [93]. Primarily, this is derived from its high effective nonlinear coefficient ($d_{eff} \approx 27 \text{ pm/V}$). On the other hand, $LiTaO_3$ is a promising candidate when pump source lies in the visible band. However, $PPLT$ possesses lower d_{eff} ($\approx 16 \text{ pm/V}$), and shorter length $L \approx 40 \text{ mm}$), thus exhibits lower parametric conversion efficiency. It is worthwhile to note that high radiation damage threshold is a quintessential pre-requisite for an intra-cavity frequency doubling crystal. Borate crystals are well-suited for the purpose due to their birefringence properties, high thermal conductivity, small thermo-optic coefficient, small inherent absorption and cost-effectiveness. Amongst the commonly available crystals in borate family (a) $\beta - BaB_2O_4$ or BBO and (b) BiB_3O_6 ($BiBO$) are most widely used in frequency conversion as a consequence of their high effective nonlinear coefficients (d_{eff}) and long available length ($\geq 10 \text{ mm}$). $BiBO$ exhibits marginally higher d_{eff} , higher thermal conductivity (K) and improved radiation damage threshold ($> 5 \text{ GW/cm}^2$) as compared to BBO [19]. However, being a recent addition to the family, $BiBO$ is comparatively less investigated and more expensive than BBO . It is important to note that intra-cavity frequency-doubling is subjected to resonant signal power exceeding 200 W within the SRO cavity and therefore, the thermo-optic coefficient ($\frac{dn}{dT}$) as well as thermal conductivity (K) of a particular borate crystal plays a crucial role in determining conversion efficiency in addition to d_{eff} . In fact, the ratio between the thermo-optic coefficient to thermal conductivity *i.e.* $\frac{dn/dT}{K}$ provides an estimation of the impact of thermal manifestations on the generated beam [94]. This ratio was found out to be smaller in case of $BiBO$ as compared to BBO which indicates that, possibly $BiBO$ would exhibit a better performance in an intra-cavity configuration [30]. Here, we present a novel configuration for generating tunable NIR radiation in an intra-cavity Yb-fiber laser pumped periodically-poled $LiNbO_3$ or $PPLN$ based SRO. In addition, we present a comparison on the performance between $BiBO$ and BBO as a frequency-doubling element for generating single-frequency NIR radiation in $750 - 780 \text{ nm}$ band.

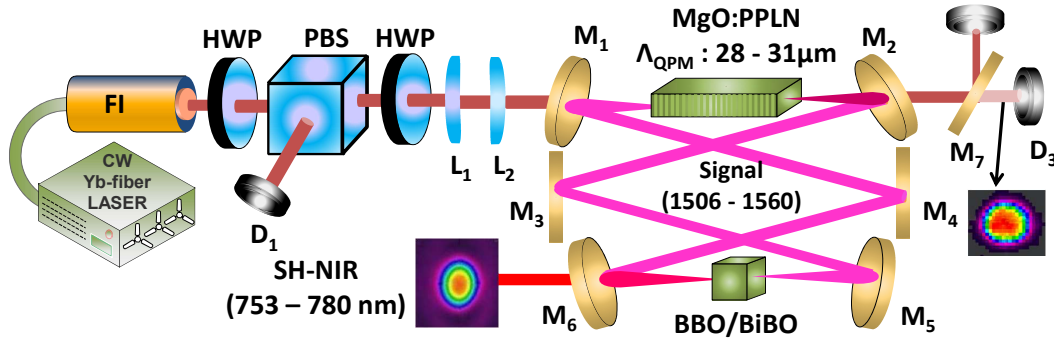


Figure 4.1 Schematic of intra-cavity second-harmonic-generation (IC-SHG) in SRO \Rightarrow FI: Faraday isolator; HWP: half wave plate; PBS: polarizing beam splitter; L_1 and L_2 : lenses; $M_{1,2}$: mirrors with radius of curvature (ROC) -200 mm; $M_{3,4,7}$: plane mirrors; $M_{5,6}$: mirrors with ROC -150 mm.

4.2 Experimental Set-up

4.2.1 Laser and beam focusing

The experimental set-up for intra-cavity frequency-doubling of SRO signal is shown in Fig. 4.1. Here, the pump source is a CW Yb-fiber laser delivering linearly polarized output of 40.0 W at 1064 nm wavelength (IPG Photonics: YLR-40-1064-LP-SF) which exhibits a nominal line-width of < 100 kHz with an excellent beam-quality ($M^2 < 1.05$) in TEM_{00} mode-profile. In order to vary the pump power, we employed a combination of HWP and a PBS. A second HWP is employed for obtaining appropriate pump polarization so as to facilitate phase-matching in nonlinear crystal. A combination of concave ($f = -100$ mm) and convex lenses ($f = 75$ mm) results in a pump beam-waist of $w_{0p} = 75$ μ m which ensures a confocal parameter $\xi = L/b = L/kw_{0p}^2 = 1.12$ at the pump frequency, where L is crystal length and k is propagation vector of pump beam [44].

4.2.2 Nonlinear crystals

The nonlinear crystal is a 5 – mol% MgO-doped PPLN (MgO:PPLN) crystal which is 80 mm long, 6.9 mm wide and 1 mm thick (HC-Photonics, Taiwan). It has six grating periods (Λ) ranging from 28.5 to 31 μ m in steps of 0.5 μ m. The front and back surfaces of

MgO:PPLN crystal is anti-reflection (AR) coated for 1064 nm ($R < 3\%$), $1400 - 1750\text{ nm}$ ($R < 0.5\%$) and $2500 - 4500\text{ nm}$ ($R < 10\%$) wavelengths. MgO:PPLN crystal is housed in an oven whose temperature can be varied from room temperature to 200°C with a resolution of 0.1°C . MgO:PPLN crystal mount is designed in such a way that its three faces are in contact with brass based heat sink. Such heat-sink design is discussed in detail in chapter-5 (of the present thesis) and the design ensures efficient heat extraction from the MgO:PPLN crystal at high pump powers [78, 31]. In order to carry out intra-cavity second-harmonic-generation (IC-SHG), we use 10 mm long (i) BBO and (ii) BiBO crystal in separate experiments. Both the crystals have $5\text{ mm} \times 5\text{ mm}$ rectangular aperture and AR coated in $1500 - 1600\text{ nm}$ as well as $750 - 800\text{ nm}$ band. In order to facilitate IC-SHG of $1500\text{ nm} + 1500\text{ nm} \rightarrow 750\text{ nm}$ ($o + o \rightarrow e$), BBO crystal has crystal-cut at $\theta = 19.84^\circ$ whereas BiBO has crystal-cut of $\theta = 10.7^\circ$, $\phi = 0.0^\circ$ for phase-matching in XZ-plane [18]. BBO as well as BiBO crystals are housed in a home-made crystal mount which facilitates crystal rotation so as to achieve phase-matching for IC-SHG. In addition, the crystal mount configuration serves to efficiently radiate out the generated heat through Aluminum contacts surrounding the crystal from three lateral directions.

4.2.3 Cavity mirrors

The SRO cavity consists of six mirrors amongst which four are plano-concave and the other two are plane mirrors as shown in Fig. 4.1. The motivation behind the choice of six-mirror configuration is described in the next paragraph. The mirrors $M_{1,2}$ have radius of curvature (ROC) of -200 mm whereas mirrors $M_{5,6}$ have the ROC of -150 mm and $M_{3,4}$ are plane mirrors. All the mirrors have high reflection ($R > 99.5\%$) in $1350 - 1650\text{ nm}$ and high transmission ($T > 95\%$) in $2900 - 4500\text{ nm}$ wavelength band. The back surface of all the mirrors are AR coated for 1064 nm and in $2900 - 4500\text{ nm}$ band. Transmission of the mirrors M_5 and M_6 vary from 50% to 80% in $750 - 800\text{ nm}$ band. A characterization of these mirrors in $750 - 780\text{ nm}$ is provided in the appendix (Fig. A.2). Total length of

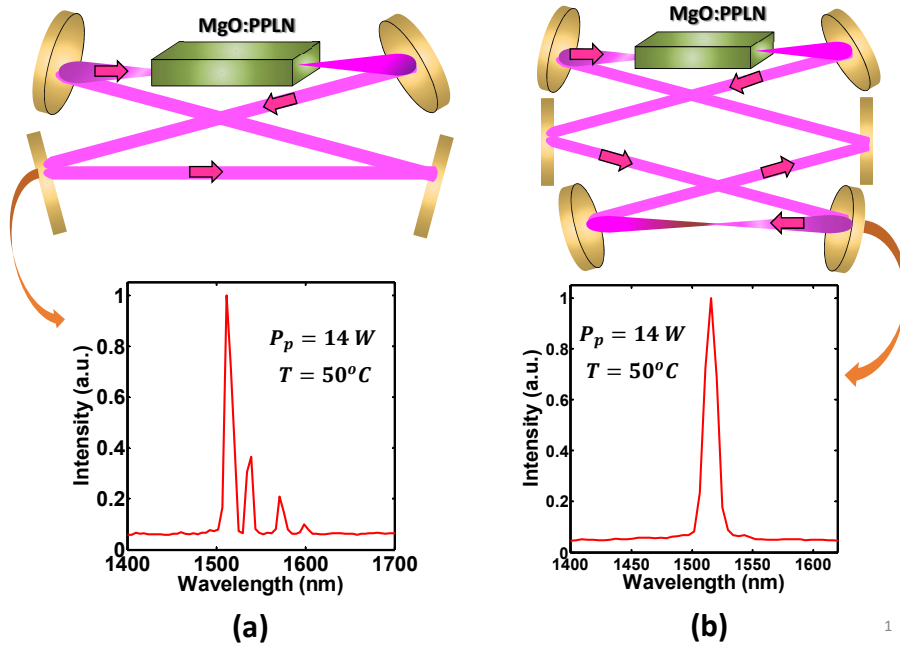


Figure 4.2 (a) Four-mirror and (b) Six-mirror cavity along with the corresponding Signal spectrum

the cavity is measured to be 1396 mm . Dichroic mirror M_7 is deployed to separate the pump beam from the generated idler beam.

4.3 Cavity design

The initial SRO cavity-design was realised with four-mirror ring-cavity configuration using two curved mirrors ($ROC = -200\text{ mm}$ each) and two plane mirrors with the specifications identical to mirrors M_1 and M_2 mentioned before. The SRO threshold, in this case, was measured to be $P_{th} \approx 3.0\text{ W}$ for a grating period $\Lambda = 30\ \mu\text{m}$. However, at higher pump powers ($P_p \geq 4.5\text{ W}$), the signal spectrum exhibited multiple peaks as shown in Fig. 4.2. Such additional peaks are essentially a consequence of low oscillation threshold of SPS for LiNbO_3 in the high-finesse SRO cavity [30, 79, 80, 95, 49] as described in chapter 2 and 3. It is worthwhile to recall that the cavity finesse in signal band ($1350 - 1750\text{ nm}$) is ≈ 250 . Therefore, it is straightforward to infer that polariton-mode oscillations would have adverse impact on single-mode signal oscillation which would, in turn, result into multiple peaks in frequency-doubled output. In order to retain the single-mode feature of

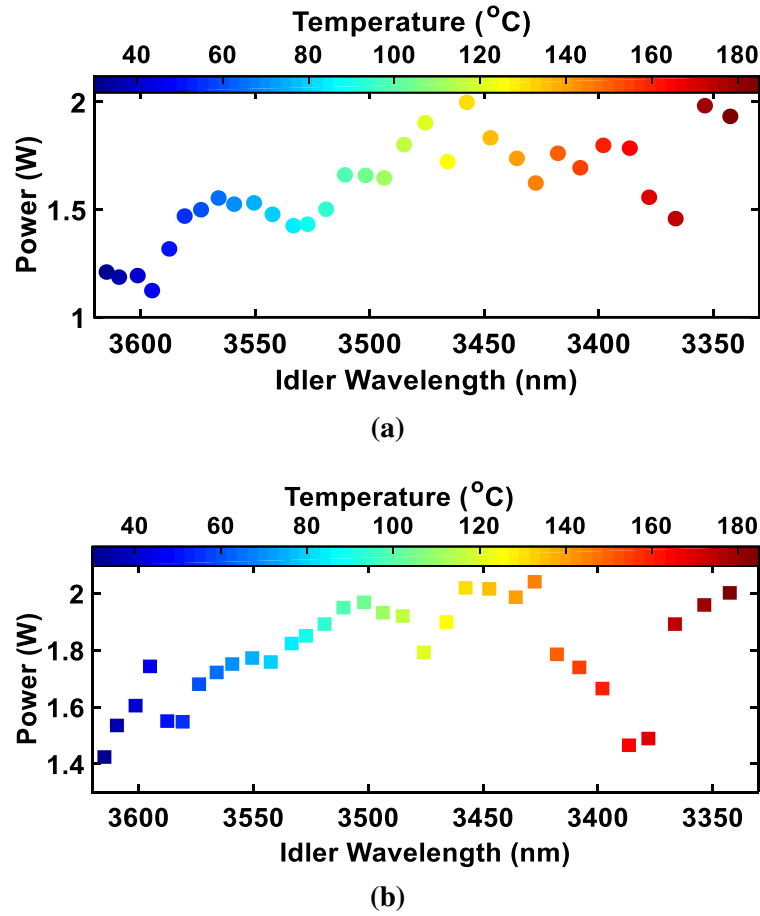


Figure 4.3 Variation of generated idler power as a function of idler wavelength when *MgO:PPLN* crystal temperature was varied from 30 – 185°C (in step of 5°C) at $P_p = 14$ W and $\Lambda = 30$ μm in case of (a) BBO-based SRO and (b) BiBO-based SRO.

resonant signal, we introduce two additional curved mirrors (M_5 and M_6) in the cavity as shown in Fig. 4.1. Such an alteration serves two purpose simultaneously (i) Stokes oscillations are inhibited due to additional cavity loss (ii) small beam-waist $w_{0s} \approx 65$ μm for signal beam at the centre of borate crystals which is primarily due to optimum six-mirror cavity design. Consequently, pump threshold for the BBO based six-mirror ring-cavity SRO is $P_{th(BBO)} \approx 5.8$ W whereas it reduces to $P_{th(BiBO)} \approx 4.3$ W for BiBO based SRO for $\Lambda = 30$ μm of *MgO:PPLN* [30]. All the measurements described hereafter have been carried out in six-mirror ring-cavity configuration as shown in Fig. 4.1.

4.4 Temperature tuning

In order to achieve SRO signal and idler tuning, *MgO:PPLN* crystal temperature is varied from room temperature to 185°C keeping the pump power fixed at $P_p \approx 14\text{ W}$ and $\Lambda = 30\ \mu\text{m}$. The choice of maximum $P_p \approx 14\text{ W}$ is essentially governed by the observation that the idler output tends to saturate for $P_p \geq 14.0\text{ W}$ in case of BBO based SRO. Through this scheme, we obtained continuous idler tuning from $3343 - 3615\text{ nm}$ as shown in Fig 4.3(a). In case of BBO based SRO, we obtain maximum idler power of $P_{i(\text{BBO})} \approx 2\text{ W}$ at 3447 nm (*MgO:PPLN* crystal temperature $\approx 130^\circ\text{C}$) resulting in 14.3% conversion efficiency for the idler. Average power for the idler is $\approx 1.6\text{ W}$ over the entire tuning range as shown in Fig. 4.3(a). On a similar note, BiBO based SRO results in maximum idler power of $P_{i(\text{BiBO})} \approx 2.05\text{ W}$ at idler wavelength of 3417.5 nm when the temperature of *MgO:PPLN* crystal temperature is 145°C (see Fig. 4.3(b)) [30]. The average idler power for BiBO based SRO across the tuning range remains similar to that for BBO based SRO.

4.5 Single-frequency intra-cavity SHG

In the first configuration, BBO crystal is placed between mirrors M_5 and M_6 of the SRO cavity as shown in Fig. 4.1. As a consequence, second-harmonic NIR (SH-NIR) wavelength tunable from $753 - 780\text{ nm}$, is generated when *MgO:PPLN* crystal temperature is varied from $30 - 185^\circ\text{C}$ for $\Lambda = 30\ \mu\text{m}$. It was observed that power in the red beam maximizes when *MgO:PPLN* crystal temperature is 60°C i.e. $P_r \approx 2\text{ W}$ at a wavelength $\lambda_r = 758\text{ nm}$. Across the entire tuning range, average power in BBO based SRO is measured to be $P_{r(\text{avg})} \approx 1\text{ W}$ as can be seen in Fig. 4.4(a). It could also be observed that $P_r \geq P_{r(\text{avg})}$ in the wavelength range of $755 - 768\text{ nm}$ and IC-SHG output tends to reduce at longer wavelengths. It is worthwhile to point out that the BBO crystal was adjusted marginally for maximizing the power in red-beam while carrying out the

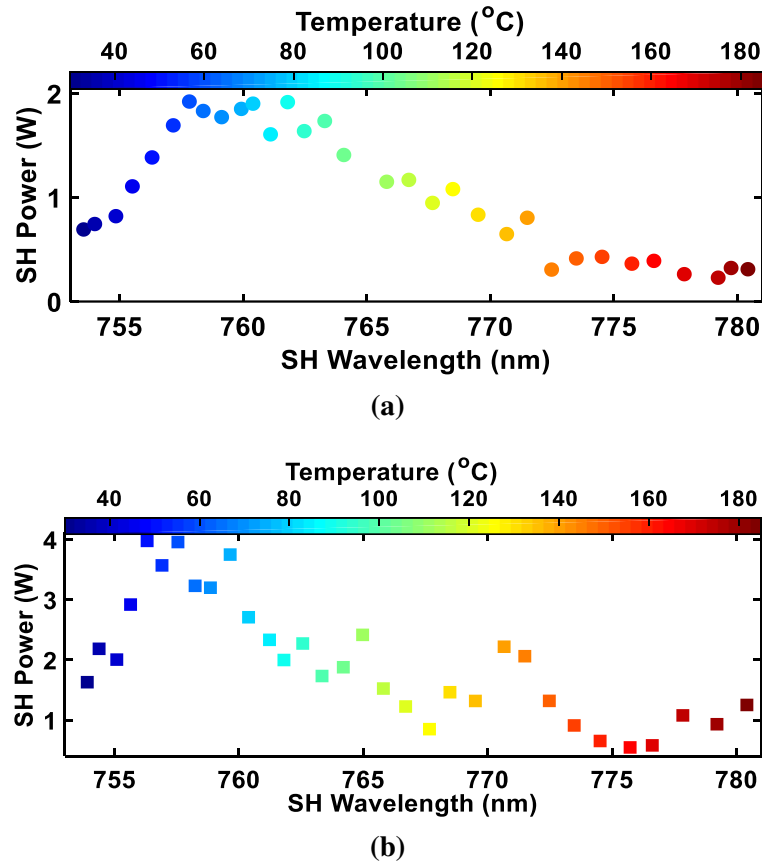


Figure 4.4 Variation of generated SH-NIR power as a function of SH-NIR wavelength when *MgO:PPLN* crystal temperature was varied from 30 – 185°C at $P_p = 14$ W and $\Lambda = 30$ μ m in case of (a) BBO-based SRO and (b) BIBO-based SRO.

temperature tuning of *MgO:PPLN* crystal. On the other hand, in the second configuration, BIBO crystal is placed between mirrors M_5 and M_6 of the SRO cavity. It was observed that BIBO based SRO delivers a maximum power in the red-beam $P_{r(BIBO)} \approx 4$ W at $\lambda_r = 756$ nm for $P_p \approx 14$ W which could be seen in Fig. 4.4b. The average red-power in BIBO based SRO is ≈ 1.9 W across the entire tuning range (753 – 780 nm). Similar to BBO-based SRO, it is evident that the power in red-beam reduces at longer wavelengths for BiBO-based SRO. Overall, from Fig. 4.4, it is straightforward to note that the variation of intra-cavity frequency-doubled power or SH power in red for BBO-based as well as BiBO-based SRO is non-uniform across the entire tuning range. Such an irregular variation could be attributed to the following factors (i) non-uniform AR-coating on the faces of the BBO/BiBO crystal within the signal band (1500 – 1600 nm) as well

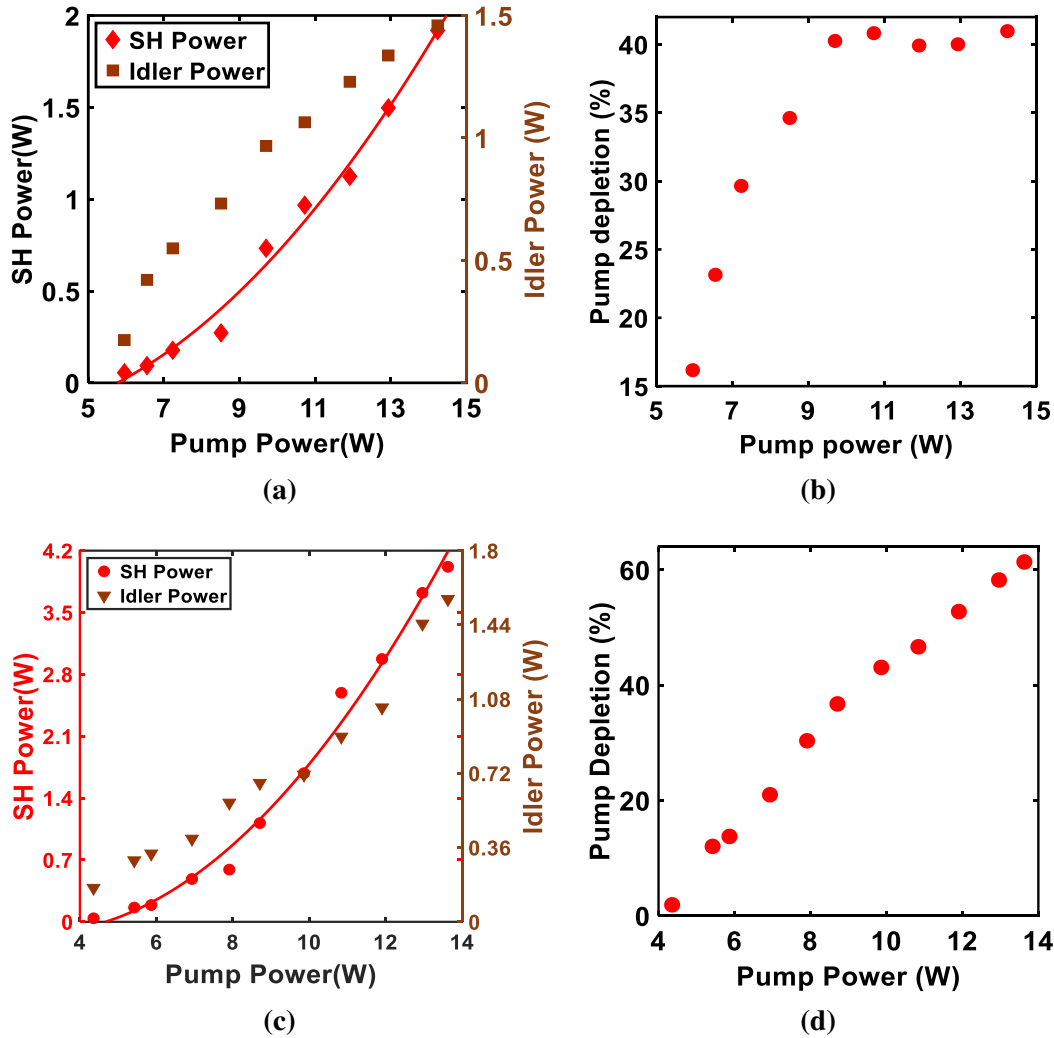


Figure 4.5 Variation of generated SH-NIR power and corresponding idler power as a function of pump power for (a) BBO-based SRO and (c) BIBO-based SRO. Variation of pump-depletion (in %) as a function of pump power for (b) BBO-based SRO and (d) BIBO-based SRO.

as visible band (750 – 800 nm) (ii) mirror reflectivity as well as *MgO:PPLN* crystal AR-coating of the mirrors within the SRO cavity. Overall photon conversion efficiency for generation of tunable red-radiation in case of both the configuration is estimated using $\eta = \frac{\lambda_r P_r + \lambda_i P_i}{\lambda_p P_p}$. For BBO-based SRO, maximum value of η is estimated to be $\eta_{max} \approx 46\%$ when $\lambda_r = 758 \text{ nm}$ whereas $\eta_{max} \approx 59\%$ for BiBO based SRO at $\lambda_r = 756 \text{ nm}$.

In order to ascertain the dependence of SH-NIR power generation on incident pump power, the growth of SH-NIR power as a function of pump power (P_p) is recorded at a fixed *MgO:PPLN* crystal temperature and $\Lambda = 30 \mu\text{m}$. In case of IC-SHG in BBO-based

SRO, the variation in SH-NIR power with the pump power when $MgO:PPLN$ crystal temperature is held at $60^\circ C$ ($\lambda_r = 758\text{ nm}$), is shown in Fig. 4.5(a). It could be observed from the figure that the idler power (P_i) tends to saturate for $P_p \geq 10\text{ W}$ which is evident in the variation of pump depletion as a function of P_p (Fig. 4.5(b)). Saturation in the idler power and consequently a linear growth in SH-NIR power (for $P_p \geq 11\text{ W}$) is primarily due to excess thermal loading on $MgO:PPLN$ crystal when the intra-cavity signal power is high. On the other hand, the SH-NIR power scales quadratically with respect to P_p up to $P_p = 14.0\text{ W}$ in case of BiBO-based SRO at $MgO:PPLN$ crystal temperature of $50^\circ C$ ($\lambda_r = 756\text{ nm}$) as shown in Fig. 4.5(c) [30]. Consequently, we did not observe saturation in idler power as well as pump depletion (Fig. 4.5(d)) up to $P_p = 14\text{ W}$. Such an observation could be appreciated by noting the fact that BiBO exhibits a higher d_{eff} and lower absorption as compared to BBO which results in higher signal to SH-NIR conversion. Additionally, a higher thermal conductivity of BiBO with respect to BBO plays a crucial role by rapid removal of thermal energy into the metallic (aluminium-based) crystal mount. Consequently, a higher signal to SH-NIR conversion results in reduced thermal loading on $MgO:PPLN$ crystal in the SRO at higher pump powers.

4.6 Line-width and M^2 measurement

The single-frequency signal oscillation and subsequent generation of single-frequency SH-NIR is confirmed using scanning Fabry-Perot interferometer (FPI-100, Toptica Photonics, Germany) with $FSR = 1\text{ GHz}$ and finesse > 400 . The SH-NIR spectrum for BBO-based SRO is shown in Fig. 4.6(a) which shows equidistant transmission peaks with the separation of 1 GHz which is same as the FSR of the FPI. The measurement have been carried out when $\lambda_r = 758\text{ nm}$ at pump power of $P_p = 14\text{ W}$. Additionally, linewidth of transmission peaks is estimated to be $\approx 2.3\text{ MHz}$. Under identical conditions, the SH-NIR spectrum of BiBO-based SRO at $\lambda = 756\text{ nm}$, shown in Fig. 4.6(b), exhibits equidistant transmission peaks with a spacing of 1 GHz between consecutive peaks. The

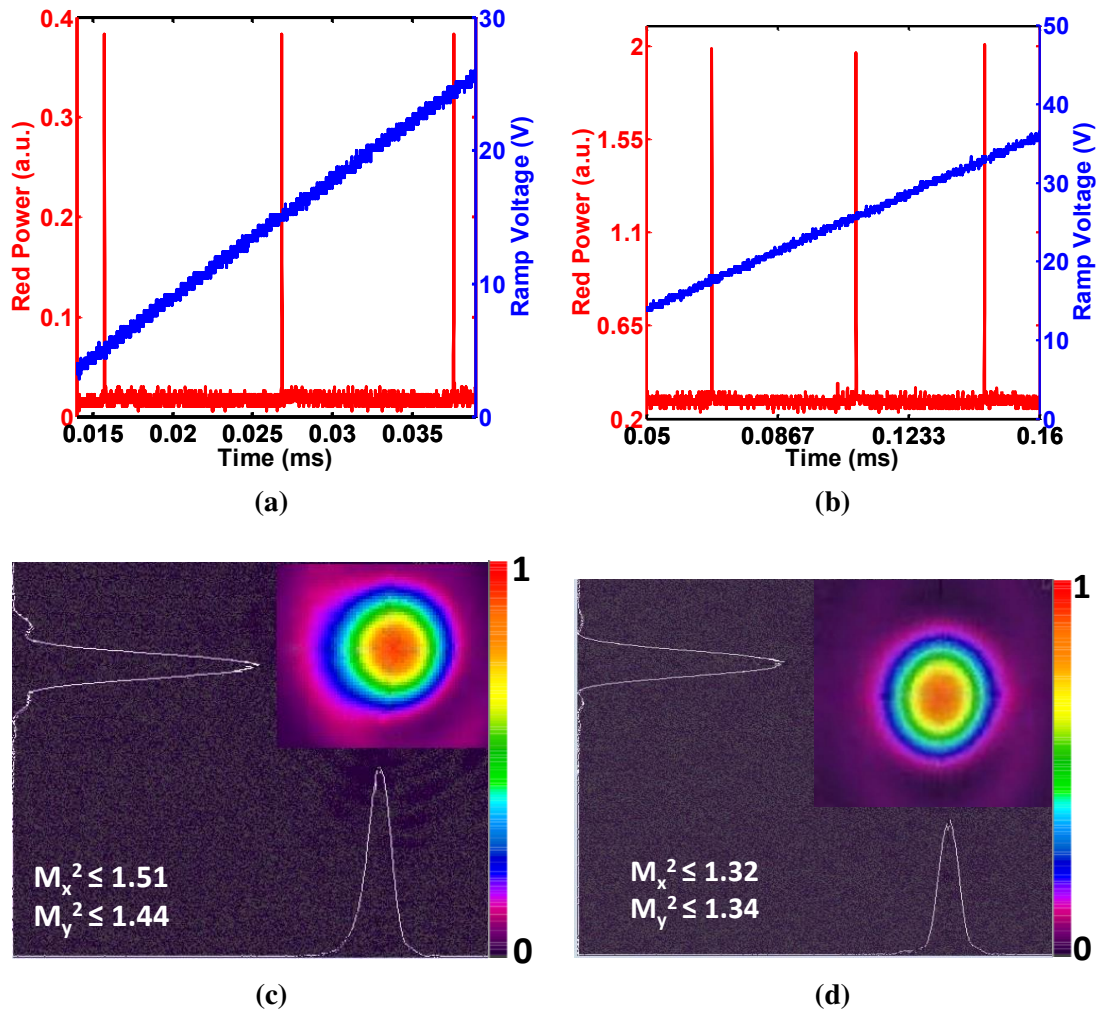


Figure 4.6 Fabry-Perot interferometer (FPI) spectrum of SH-NIR in (a) BBO-based SRO and (b) BiBO-based SRO. Recorded beam-intensity-profiles with measured M^2 values of SH-NIR beam for (c) BBO-based SRO and (d) BiBO-based SRO.

linewidth of transmission peaks is estimated to be ≈ 3 MHz in case of BiBO-based SRO. Here, it is to be noted that the measurements are essentially limited by the resolution of scanning FPI and we expect smaller linewidth of generated SH-NIR radiation as the pump source Yb-fiber laser has a nominal line-width of $\Delta\nu \approx 100$ kHz.

The spatial beam quality of SH-NIR beam is characterized by capturing intensity beam-profile of BBO-based as well as BiBO-based SRO output using CCD camera (GRAS 2.0, Point Grey Inc.) for incident $P_p = 14$ W (see Fig. 4.6(c) and 4.6(d)). The recorded beam profiles confirm Gaussian TEM_{00} mode for the SH-NIR beam for both

the cases. Using a scanning beam-profiler (NanoScan, Ophir Optronics), beam quality parameter (M^2) of the SH-NIR beam is measured. The SH-NIR beam from BBO-based SRO exhibits $M_x^2 \leq 1.51$, $M_y^2 \leq 1.44$ ($\lambda_r = 758 \text{ nm}$) whereas BiBO-based SRO shows an $M_x^2 \leq 1.32$, $M_y^2 \leq 1.34$ ($\lambda_r = 756 \text{ nm}$). As a reference, it could be noted that the pump beam exhibits a nominal $M^2 \leq 1.05$. The distortion in spatial beam-quality could be primarily attributed to significant spatial walk-off in BBO and BiBO crystal for given crystal-cut so as to achieve SH phase-matching.

4.7 Frequency and Power fluctuations

Additionally, we have recorded the long-term frequency fluctuation of SH-NIR beam for BBO-based as well as BiBO-based SROs using a UV-visible wavelength-meter (WS/7 UV, HighFinesse GmbH, Germany) of resolution $< 60 \text{ MHz}$ under free-running conditions. The recorded stability measurements are shown in Fig. 4.7(a). For an incident pump power of $\approx 14 \text{ W}$, BBO-based SRO exhibits a peak-to-peak frequency fluctuation of $\approx 21 \text{ GHz}$ about the mean frequency of $\nu_r = 395.5045 \text{ THz}$ over *one*-hour duration. Interestingly, peak-to-peak frequency fluctuation of SH-NIR beam in case of BiBO-based SRO is $\approx 3.3 \text{ GHz}$ about the mean $\nu_r = 396.5508 \text{ THz}$ for an identical time period. It is to be noted that the peak-to-peak frequency fluctuation in BiBO-based SRO is ≈ 7 -times lesser than that for BBO-based SRO. This, again, is primarily a consequence of better thermal management in BiBO crystal by virtue of its lower $\frac{dn/dT}{K}$ as compared to BBO. Nevertheless, active stabilisation techniques could significantly improve the stability of SH-NIR frequency [83]. The long-term power fluctuation for SH-NIR beam for BBO-based SRO as well as BiBO-based SRO have been recorded over an hour at maximum pump power of 14 W and is shown in Fig. 4.7(b). The measurements show peak-to-peak SH-NIR power fluctuation of $\approx 19\%$ about the mean in case of BBO-based SRO. On the other hand, BiBO-based SRO exhibits $\approx 13\%$ peak-to-peak fluctuation about the mean SH-NIR power. By employing improved thermal management schemes as well as

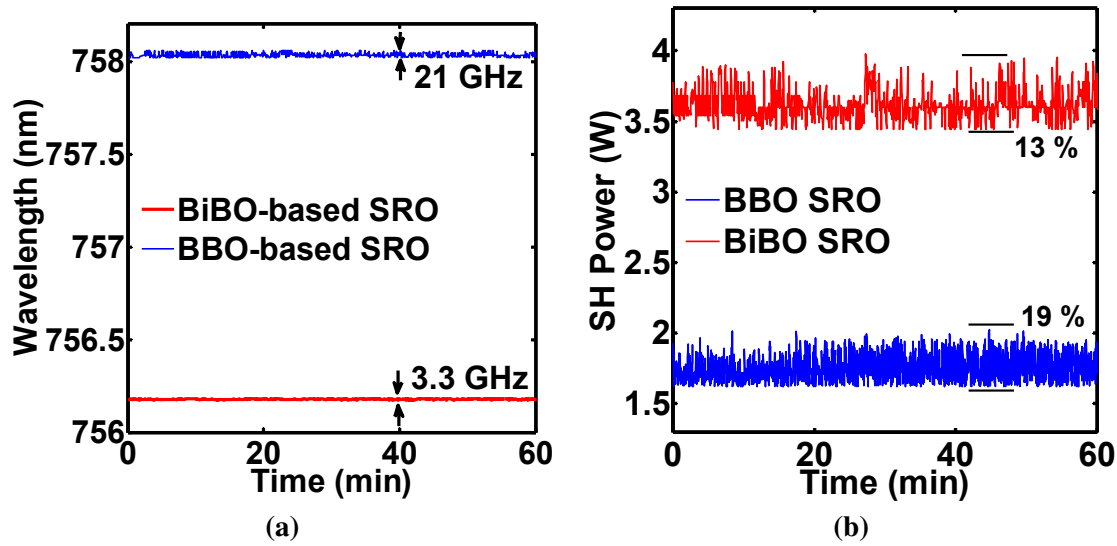


Figure 4.7 (a) Frequency and (b) power fluctuations in SH-NIR beam over an hour for BBO-based SRO (red) and BiBO-based SRO (blue) when $P_p = 14$ W and $\Lambda = 30\mu\text{m}$.

appropriate isolation, the stability in SH-NIR output power could be improved further for both the SRO configurations. Hereby, we have summarized the SH-NIR characteristics of BBO-based SRO as well as BiBO-based SRO in Table 4.1.

Table 4.1 Comparison chart of both the intra-cavity SROs

OPO Properties	BBO-SRO	BiBO-SRO
Threshold (W)	5.8	4.3
Max Power (W)	2 (758 nm)	4 (756 nm)
Power fluctuation (%)	19	11
Wavelength tunable range (nm)	753-781 (SH) 3343-3619(idler)	753-781(SH) 3343-3619(idler)
Frequency fluctuation (GHz)	21 (1-hour)	3.3 (1-hour)
Line-width (MHz)	2.3	3
Beam-shape	Gaussian (TEM_{00})	Gaussian (TEM_{00})
M^2 -factor	$M_x^2 = 1.51$ $M_y^2 = 1.44$	$M_x^2 = 1.32$ $M_y^2 = 1.34$

4.8 Conclusion

We have presented a comprehensive investigation and comparison on the performance of two high-power, single-frequency sources generating tunable radiation in the NIR band using an intra-cavity frequency-doubled SRO. An 80mm-long *MgO:PPLN* has been used as SRO crystal for both the configurations. One of the configurations deploy a 10mm-long *BBO* crystal for carrying out IC-SHG whereas the second configuration uses a 10mm-long *BiBO* as an intra-cavity frequency-doubling element. Both the sources have been found to be widely tunable from 753 – 780 nm in the NIR band and from 3343 – 3619 nm in the MIR band by varying *MgO:PPLN* crystal oven temperature from room temperature to 185°C. *BBO*-based SRO generates maximum NIR power of 2 W at 758 nm wavelength whereas *BiBO*-based SRO delivers ≈ 4 W at 756 nm. The power-scaling measurements as well as power-stability measurement indicates better thermal management in *BiBO*-based SRO as compared to *BBO*-based SRO. Such an improvement could be attributed to higher thermal conductivity of *BiBO* with respect to *BBO* in addition to smaller thermo-optic coefficient for *BiBO*. The six-mirror ring cavity configuration of SRO enhances the threshold for oscillation of Raman stokes modes of *MgO:PPLN* thereby, maintaining single-frequency signal oscillation across the entire tuning range at pump power ≤ 15 W. This has been confirmed using scanning FPI spectrum. The measurements of spatial beam quality for both the SRO configurations show moderate distortion as compared to the pump beam which is primarily a consequence of anisotropic behaviour exhibited by *BBO* and *BiBO*. It would be worthwhile to note that the SRO tunability could be further enhanced by using other available grating periods of *MgO:PPLN* crystal. Such systems could be appropriately designed to operate near the threshold with optimum temporal and spatial beam qualities for carrying out quantum optics based experiments [96, 97]. It is important to note that the present proof of the concept could be necessarily extended to various spectral bands and this scheme could be an useful addition to the

contemporary schemes for potential applications in tissue imaging techniques such as confocal microscopy and Raman microscopy [98, 99].

Chapter 5

Frequency-doubling of high power

Yb-fiber laser

This Chapter constitutes the following journal publication:

- **Mukesh Kumar Shukla**, Samir Kumar, and Ritwick Das, “Single-pass, multi-watt second-harmonic-generation in congruent and stoichiometric $LiTaO_3$ ”, *IEEE Photonics Technology Letters*, vol. 27, pp. 1379-1382, Jul. 2015.

5.1 Motivation

Continuous wave (cw) red-blue-green coherent light sources have found many applications in material science and technology as well as in basic sciences [8, 9]. From the beginning of 21st century there has been enormous development in the fabrication of micro-nano sized semiconducting systems which have led to the development of high power diode lasers. The high power diode lasers are widely available for red and blue band of the electromagnetic spectrum. This is because of the availability of suitable semiconductor materials for this region. However, high power green diode lasers are still a challenge to the manufactures. On the other hand, the applications in display technology and medical sciences also require spectrally pure green lasers with high luminosity and

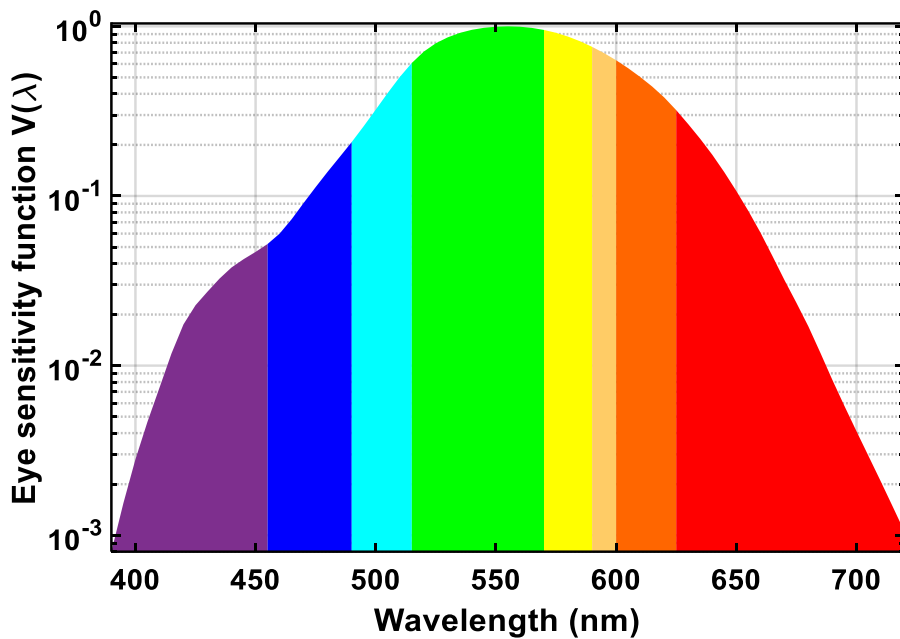


Figure 5.1 The variation of eye sensitivity function with wavelength as per recommendation of CIE 1978.

efficiency. In laser technology, green lasers are crucial for functioning of Titanium Sapphire laser systems which, in turn, form the backbone for the studies related to ultrafast atomic and molecular dynamics. In addition, it forms a crucial part of many display devices. The view-graph in Fig. 5.1 shows eye sensitivity function ($V(\lambda)$) as a function of visible wavelength (nm) [100, 101]. It is evident that human eye is highly sensitive to entire green spectrum and the sensitivity reaches maximum at $\lambda = 555\text{ nm}$. Amongst the available green laser sources, the *argon ion* ($Ar^+ - ion$) gas laser emitting multi-watt optical power at $\lambda = 514.5\text{ nm}$ is most widely available commercially. However, the operating wavelength ($\lambda = 514.5\text{ nm}$) is less sensitive to human eye ($\approx 400\text{ lumen/watt}$) [102]. Additionally, the $Ar^+ - ion$ laser systems exhibit poor wall-plug efficiency and exhibit quite complicated architecture. On the other hand, gas lasers such as He-Ne lasers emit green light (at $\lambda = 523\text{ nm}$) in milli-Watt (mW) levels which is insufficient for many applications. And the thermal effects adversely affect the operation of *III - V* semiconductor (GaN and $InGaN$) based green diode lasers at high pump powers. From Fig. 5.1, it is worthwhile to note that the frequency-doubled NIR lasers operating at

$\lambda = 532 \text{ nm}$ are most sensitive ($\approx 603 \text{ lumen/watt}$) to human eye amongst the green laser sources available commercially. In addition to high wall-plug efficiency, the frequency-doubled laser systems are easy to operate and generate multi-watt power at $\lambda = 532 \text{ nm}$. The commercially available frequency-doubled laser sources operate on the principle of internal SHG of Neodymium-doped Yttrium-Aluminum-Garnet (YAG) lasers using nonlinear crystals such as LBO (LiB_3O_5) and KDP (KH_2PO_4). However, the intra-cavity configuration requires the cavity to be actively stabilized for requisite spectral features which inevitably enhances the system complexity and cost. Also, such systems require water-based cooling mechanism for optimum performance which adversely affect the system portability [103]. The present generation of laser technology is driven by compact, high-power fiber lasers which exhibit an important advantage of long amplifying medium (rare-earth doped optical fibers). Due to optical fiber based beam guidance, we obtain excellent spatial characteristics of the laser beam. However, the architecture of NIR fiber lasers limits the generation of high-power coherent green radiation in an internal SHG configuration. Therefore, in this research problem, we adopt a straightforward route to generate multiple watts of spectrally-pure green radiation using single-pass SHG of NIR fiber laser using commercially available long length ($\geq 3 \text{ cm}$) ferroelectric nonlinear crystals such as LiNbO_3 , LiTaO_3 , KTiOPO_4 . The choice of such nonlinear crystals for our experiments is essentially governed by the possibility of periodically altering the ferroelectric domains which, in turn, facilitates long interaction lengths for green and NIR beams.

From the application viewpoint, congruently-grown LiNbO_3 exhibits maximum nonlinear coefficient ($d_{33} \approx 25.4 \text{ pm/V}$) amongst the nonlinear crystals with appreciably high transparency window ($\approx 0.35 - 5.5 \mu\text{m}$) [19]. However, it has significantly low photorefractive damage threshold at visible frequencies. In addition, the absorption of visible and NIR radiation in congruently-grown LiNbO_3 is quite high which is primarily due to high green-induced infra-red absorption (GRIIRA). These factors renders LiNbO_3 as a non-preferred candidate in frequency conversion devices at visible frequencies, es-

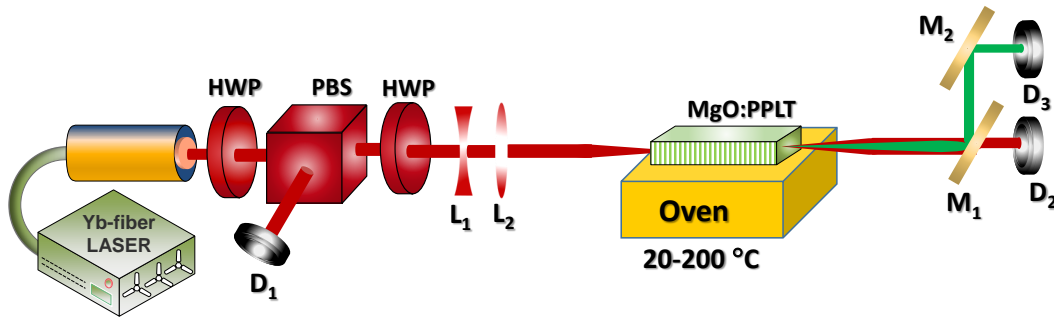


Figure 5.2 Single-pass SHG experimental schematics \Rightarrow HWP: half wave plate; PBS: polarizing beam splitter; L_1 and L_2 : lenses; M_1 and M_2 : dichroic mirrors.

pecially at high-power applications. Surprisingly, a crystal with similar structural and morphological appearance, namely, $LiTaO_3$, exhibits improved features for high-power applications. It has high thermal conductivity ($\geq 8 W/m-K$) in addition to extremely high photorefractive damage threshold. Also, it does not exhibit GRIIRA in frequency conversion experiments involving visible frequencies.

In this chapter, we have presented our investigations on the generation of single-frequency green radiation by frequency-doubling of Ytterbium (Yb)-fiber laser ($\lambda_p = 1064 nm$) using two different nonlinear crystals in a single-pass configuration. Here, we explore two variants of periodically-poled $LiTaO_3$ (PPLT) crystals. One is congruently grown and the other is stoichiometrically grown. The congruently grown crystal provides a maximum of 8 W of green power with moderate beam qualities. On the other hand, the stoichiometrically grown PPLT crystal facilitates in generation of 14.5 W with a conversion efficiency of 37 % with excellent spectral and spatial features in the beam. We also present a comprehensive analysis and comparison of the spatial as well as temporal characteristics of the generated SH in case of both the crystals.

5.2 Experimental Set-up

The experimental configuration is shown in Fig. 5.2. The fundamental pump source is a cw Yb-fiber pump laser delivering 40.0 W output power at 1064 nm wavelength (IPG

Photonics: YLR-40-1064-LP-SF) with linear polarization. The nominal linewidth ($\Delta\nu$) of the pump is $< 100\text{ kHz}$. M^2 of the pump beam is 1.05 and it is operating in TEM_{00} mode profile which is a Gaussian. We have always operated the pump source at its maximum output power so as to achieve stable performance. In order to control the pump power being incident on the nonlinear crystal, we have utilised a combination half-wave-plate (HWP) and a polarizing beam splitter (PBS). A 2nd HWP is inserted to get the correct polarization of the pump in the periodically-poled nonlinear material for satisfying the phase-matching condition. A plano-concave lens with a focal length $f_1 = -100\text{ mm}$ and a plano-convex lens having a focal length $f_2 = 100\text{ mm}$ is employed to get optimum focusing condition at the center of the nonlinear crystal. This combination of lenses is also useful to vary the focused beam-waist of the pump by changing the separation (d) between the two lenses. And hence the effective focal length $f_{eff} = \frac{f_1 f_2}{f_1 + f_2 - d}$ which results in $w_0 = \frac{\lambda_p f_{eff}}{\pi w_p}$ where λ_p is pump wavelength and w_p is the beam waist before L_1 . The nonlinear crystals for this study are

- MgO:sPPLT ($l = 30\text{ mm}$ long)
- MgO:cPPLT ($l = 50\text{ mm}$ long)

The length of the crystals are limited by their availability with manufacturers. It is important to note that the maximum wafer size for stoichiometric $LiTaO_3$ is approximately 1.5 inch diameter, where congruent forms of $LiTaO_3$ is available with 2 inch diameter wafers. Based on their dispersion properties, MgO:sPPLT has a grating period $\Lambda = 7.97\ \mu\text{m}$ and MgO:cPPLT have $\Lambda = 7.91\ \mu\text{m}$. These grating periods are chosen to satisfy the exact phase-matching as per the theoretical calculations [37]. The crystals are housed in a resistive heating oven (HC-Photonics). The oven temperature could be varied from 20°C to 200°C with a resolution of 0.1°C . The usual oven design is such that the crystal is heated from the bottom and one side whereas one teflon bar is used for holding the crystal from the other side. It is open from the top for radiating out the generated heat. In order to get a better thermal stability, we re-designed the oven by replacing the teflon

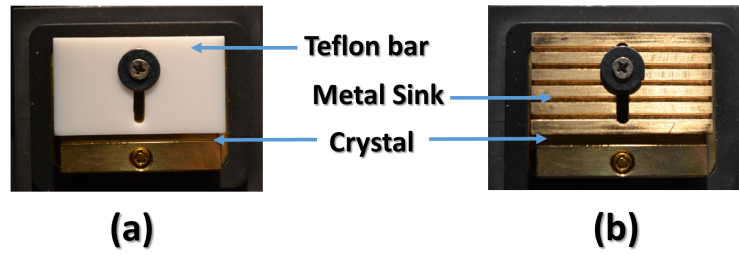


Figure 5.3 (a) Teflon supported crystal oven, (b) Metal sink supported crystal oven.

(non-conducting) bar with a corrugated-brass plate for efficiently extracting the generated heat from the crystal at high pump powers. An image of modified oven design is shown in Fig. 5.3.

The pump beam waist at the center of the MgO:cPPLT crystal is $36 \mu\text{m}$ which gives a focusing parameter $\xi = 2.6$. Similarly the beam waist at MgO:sPPLT is $30 \mu\text{m}$ with $\xi = 2.7$. Here the beam radius corresponds to the $1/e^2$ intensity. Mirrors M_1 and M_2 are plane. They are used for separating the fundamental laser beam from the SH beam. They are highly reflecting ($R > 99.4\%$) for 1064 nm and highly transmissive ($T > 98.2\%$) for 532 nm . Thermal detectors are utilised to measure the power (Ophir).

5.3 Phase-matching temperature and tolerance

The measurement of the phase matching temperature (T_{pm}) is performed at low pump power ($P_{pump} \sim 1 \text{ W}$). This is taken into consideration as at low P_{pump} the thermal effects are negligible. So by changing the temperature of the crystal's oven and keeping the ($P_{pump} \sim 1 \text{ W}$) we noted the generated SH power (P_{SH}). And further we plotted the P_{SH} as a function of crystal oven temperature for both the PPLT variants which is shown in the Fig. 5.4. In the Fig. 5.4(a) the variation of P_{SH} with the temperature is plotted for the MgO:cPPLT crystal. It can be observed from this Fig. that the maximum SH power is obtained at the temperature of 33.5°C and hence it is the PM temperature of the MgO:cPPLT crystal *i.e.* $T_{pm}^{exp} = 33.5^\circ\text{C}$. Similarly the PM temperature for the MgO:sPPLT crystal is $T_{pm}^{exp} = 47.2^\circ\text{C}$ which is calculated from Fig. 5.4(b). Considering the PM

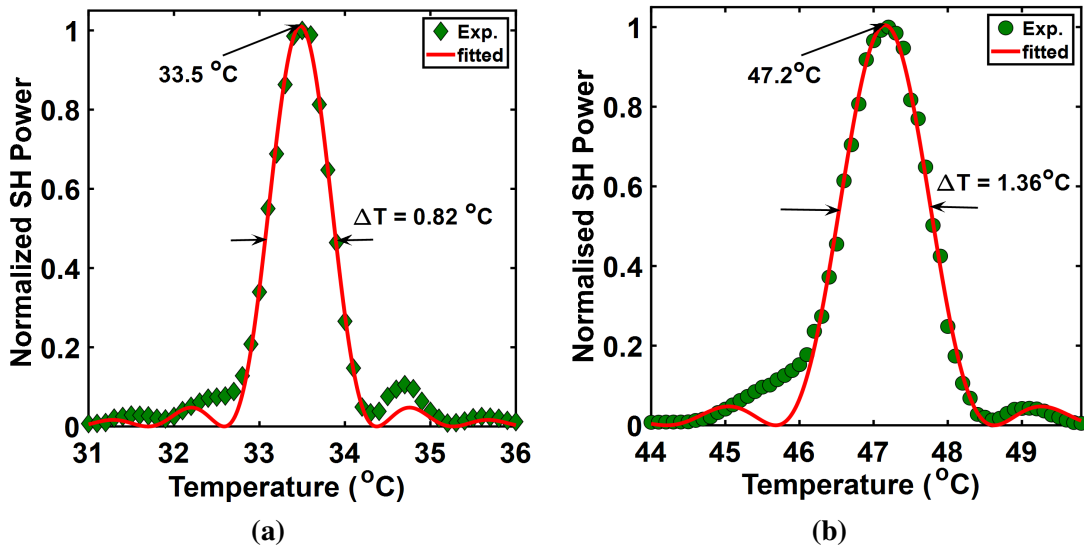


Figure 5.4 Measurement of phase matching temperature of (a) MgO:cPPLT and (b) MgO:sPPLT at $P_{pump} = 1$ W.

condition for the QPM interaction *i.e.* $\Delta k = k_{2\omega} - 2k_{\omega} - K_m = 0$ and using the Sellmeier equations for both the crystals we have theoretically calculated the PM temperature for both the crystals [104, 105]. The theoretically calculated value of the PM temperature for the crystal MgO:cPPLT is $T_{pm}^{th} = 37^{\circ}C$. Similarly for the crystal MgO:sPPLT it is $T_{pm}^{th} = 57^{\circ}C$. Theoretical PM values suggests that the experimentally observed values are lower than the theoretically calculated ones. This deviation is attributed to the small imperfection in the grating period (Λ) of the crystals at the time of manufacturing. In order to calculate the tolerance band-width of temperature (ΔT) we have fitted these plots with the $sinc^2$ curve. ΔT is the FWHM of the fitted $sinc^2$ curve. This fit provides $\Delta T_{exp} = 0.82^{\circ}C$ for MgO:cPPLT and $\Delta T_{exp} = 1.36^{\circ}C$ for the MgO:sPPLT crystals. The lower ΔT value for the MgO:cPPLT is because of its longer length than the MgO:sPPLT crystal. Considering the same experimental conditions and employing the Sellmeier's equations for the respective crystals, we have also calculated the theoretical temperature tolerance bandwidth. The theoretically calculated value for MgO:cPPLT crystal is $\Delta T_{theo} = 0.69^{\circ}C$ whereas it is $\Delta T_{theo} = 1.06^{\circ}C$ for the MgO:sPPLT crystal. The effective interaction length of the nonlinear crystals can be calculated from the theoretical

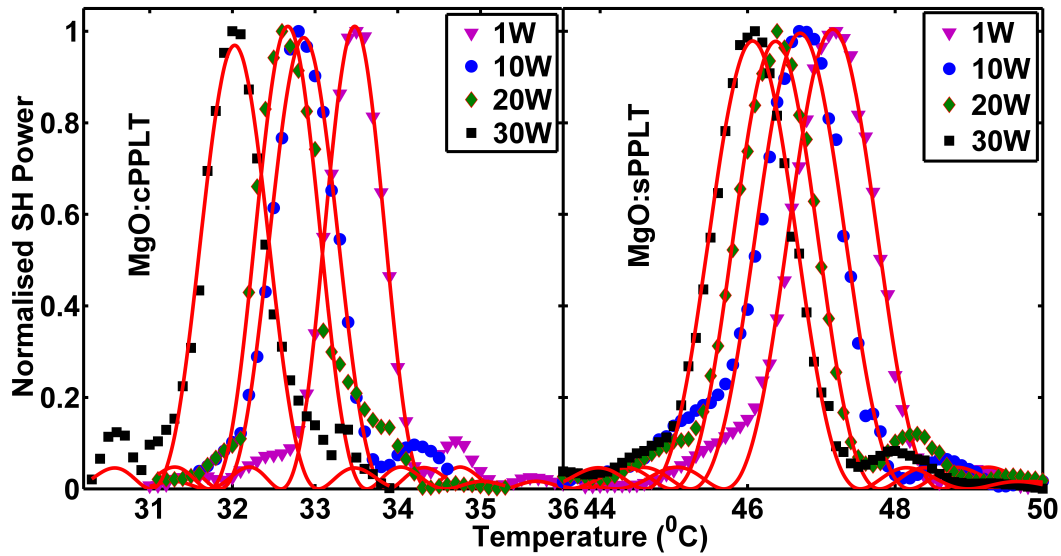


Figure 5.5 Phase matching at high pump powers. (a) At $P_{pump} = 10, 20, 30$ W the crystal oven temperature and the generated SH power for MgO:cPPLT crystal. And (b) is the same for MgO:sPPLT.

and experimental ΔT values from the following equation

$$L_{eff} = \frac{\Delta T_{theo}}{\Delta T_{exp}} \times L \quad (5.1)$$

where L is the crystal length. Using this equation the calculated effective interaction length for the MgO:cPPLT crystal is 37 mm and for MgO:sPPLT it is 28 mm. The deviation in the physical length from the effective interaction length is due to the non-uniform grating and the non-ideal focusing of the pump beam [106]. We have also calculated the value of d_{eff} by considering the $P_{pump} = 1$ W and measuring the corresponding SH power. For MgO:cPPLT its values is $d_{eff} = 10.1$ pm/V and for MgO:sPPLT it is $d_{eff} = 12.0$ pm/V.

5.4 Phase-matching at higher powers

At high pump powers such as $P_{pump} = 10$ W, $P_{pump} = 20$ W and $P_{pump} = 30$ W the phase-matching is maintained by reducing crystal-oven temperature T_{ov} appropriately in case of

both the crystals which could be seen in Fig. 5.5. This kind of behaviour is attributed to the increase in crystal absorption at high pump powers (P_p). As a consequence, the internal heat generation in the crystal requires lower temperatures for achieving phase-matching. In Fig. 5.6(a), we have plotted the variation of crystal oven temperature T_{ov} as a function of pump power upto $P_p \leq 32W$. In case of the $MgO : cPPLT$ the slope of the curve in the Fig. 5.6(a) is $\frac{dT_{pm}}{dP_p} = -0.21^\circ C/W$. In case of $MgO : sPPLT$, this slope is $\frac{dT_{pm}}{dP_p} = -0.12^\circ C/W$. These values shows that the curve is steeper for $MgO:cPPLT$. This result is primarily a consequence of low thermal conductivity of the $MgO:cPPLT$ than $MgO:sPPLT$. Due of the low thermal conductivity of $MgO : cPPLT$, the heat extraction through the conducting oven plates are weaker in comparison with the $MgO:sPPLT$.

In Table-5.6(b) we have tabulated the phase matching temperature (T_{pm}) and temperature tolerance bandwidth (ΔT) at certain higher pump powers such as $P_{pump} = 1W$, $P_{pump} = 10W$, $P_{pump} = 20W$ and $P_{pump} = 30W$. The ΔT values decrease as the increase in pump power P_p . This is contrary to our anticipation that ΔT will increase in when thermal-dephasing is significant. This is essentially due to the fact that the effective interaction length between fundamental and SH will reduce. However, the reduction in the ΔT values at high pump powers indicates that the steeper variation of the refractive index with temperature at SH wavelength as compared to that at pump wavelength, is a more dominant factor at high pump power. This plays the most dominant role in reducing ΔT at high pump power [37].

5.5 Optimally focused SHG power-scaling

In order to get the maximum SHG conversion efficiency (η_{max}) we have focused the pump beam at center of the crystal such that the focusing parameter ($\xi = \frac{l}{b}$), as defined by Boyd and Kleinman, is ~ 2.8 [44]. Here, b is the the confocal parameter and defined as $b = (2\pi/\lambda_p)w_0^2$ where w_0 is the pump beam waist at crystal center. We have optimised the distance between the two lenses L_1 and L_2 for obtaining a pump beam waist $w_0 \approx 36\mu m$

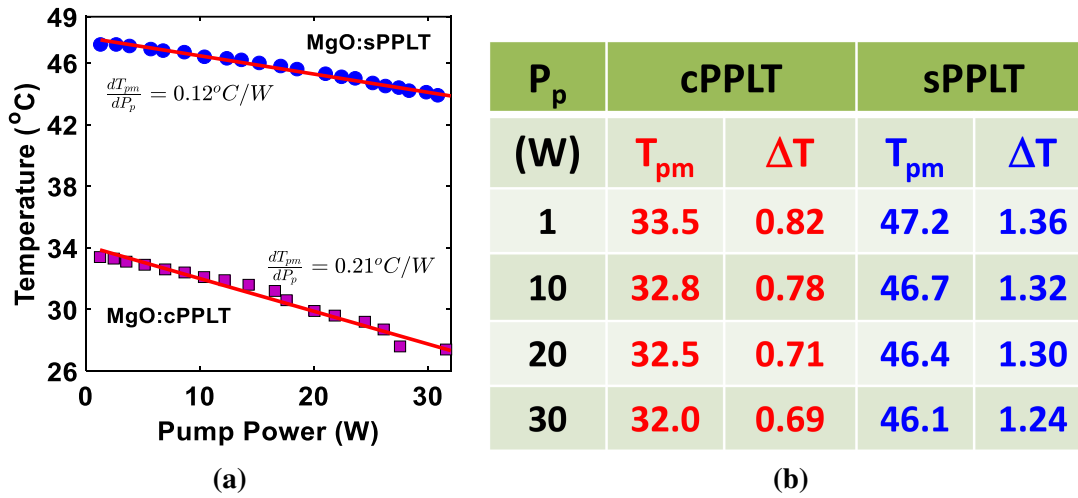


Figure 5.6 (a) The change in the crystal oven temperature along with the increase in the pump power for MgO:cPPLT and MgO:sPPLT. (b) Thermal characteristics for MgO:cPPLT and MgO:sPPLT.

for MgO:cPPLT and $w_0 \approx 29 \mu\text{m}$ for MgO:sPPLT crystal. As the MgO:cPPLT crystal has a length (l) of 50 mm so $w_0 \approx 36 \mu\text{m}$ will give a focusing parameter of $\xi \approx 2.9$. Similarly for MgO:sPPLT $l = 30 \text{ mm}$ provides $\xi \approx 2.7$. These ξ values are in close agreement with the theoretically predicted value of $\xi = 2.84$ by Boyd and Kleinman [44]. With $w_0 = 36 \mu\text{m}$ and varying the incident pump power on MgO : cPPLT crystal, we observed the variation in SH power as shown in Fig. 5.7. It could be noted that the maximum SH power $P_{SH} = 8.5 \text{ W}$ is obtained at a maximum available input pump power *i.e.* $P_{pump} = 40 \text{ W}$. This gives a maximum efficiency of $\eta = 24\%$. On the other hand, an identical exercise with MgO : sPPLT crystal results in maximum SH power $P_{SH} = 14.5 \text{ W}$ with a maximum conversion efficiency of $\eta = 36\%$ at a input pump power of $P_{pump} = 40 \text{ W}$.

It can be observed from the Fig. 5.7 that the variation of the SH power (P_{SH}) upto a $P_p \approx 17 \text{ W}$ is similar for both the crystals. In fact, for MgO:cPPLT the behaviour is quadratic up-to $P_p \approx 17 \text{ W}$ after that the behaviour turns linear. Similarly, the conversion efficiency which is defined as $\eta = \frac{P_{SH}}{P_p}$ remains linear up to $P_p \approx 17 \text{ W}$. And with further increase in the pump power after it rolls-off and tends to saturate. As evident from the Fig. its value decreases to 22% at the highest pump power of 40 W from its

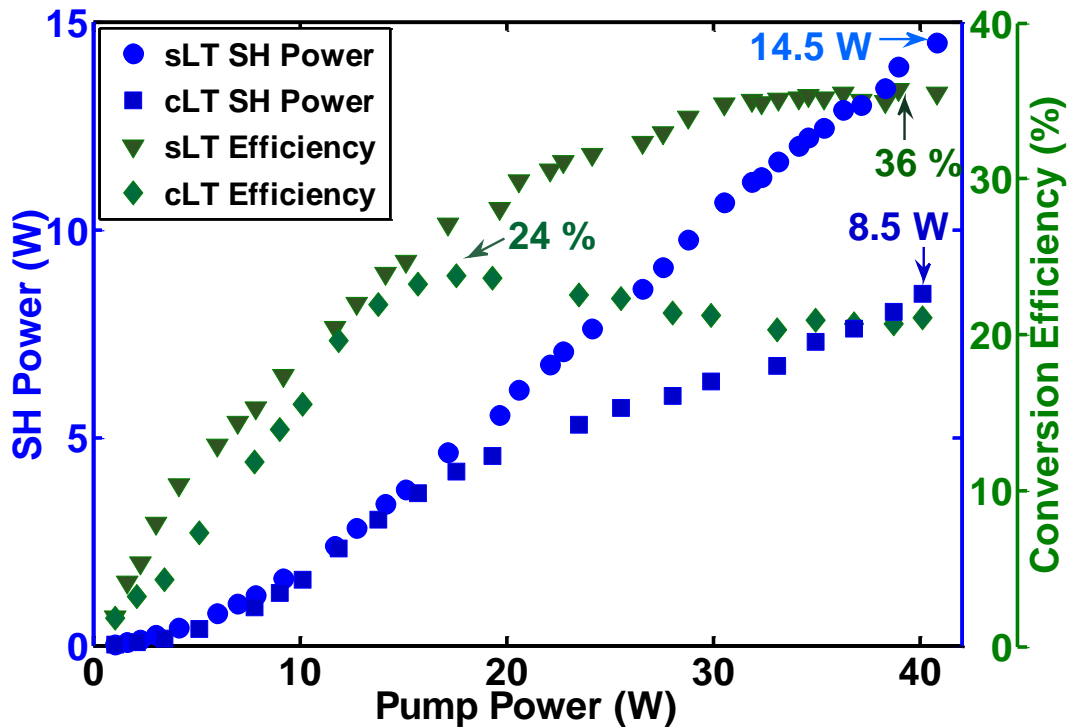


Figure 5.7 The generated SH power or P_{SH} (at 532 nm) along with the change in pump power for both the crystals indicated with the blue dots. The green dots indicates the experimentally observed conversion efficiency by continuously varying pump power for $MgO:cPPLT$ and $MgO:sPPLT$ crystals.

maximum value of 24% at $P_{pump} \approx 17$ W. On the other hand, P_{SH} for $MgO:sPPLT$ crystal maintains quadratic increase up to $P_p \approx 30$ W and subsequently, varies linearly. The conversion efficiency η , in this case, tends to saturate to $\approx 36\%$ at much higher pump power ($P_{pump} \geq 30$ W) in comparison to $MgO:cPPLT$ crystal. In general, this kind of saturation in conversion efficiency (η) as well as such non-identical variation of SH power for both the crystals could be basically due to the following physical mechanisms

- Back-conversion
- Thermally-induced dephasing
- Green induced infrared absorption (GRIIRA)

In order to claim an appropriate mechanism described above, we first examined the role of back-conversion. For this we used a chopper to make pulses of it. The chopper was operating at a frequency of 520 Hz with a duty cycle 5.5 %. We measured input pump

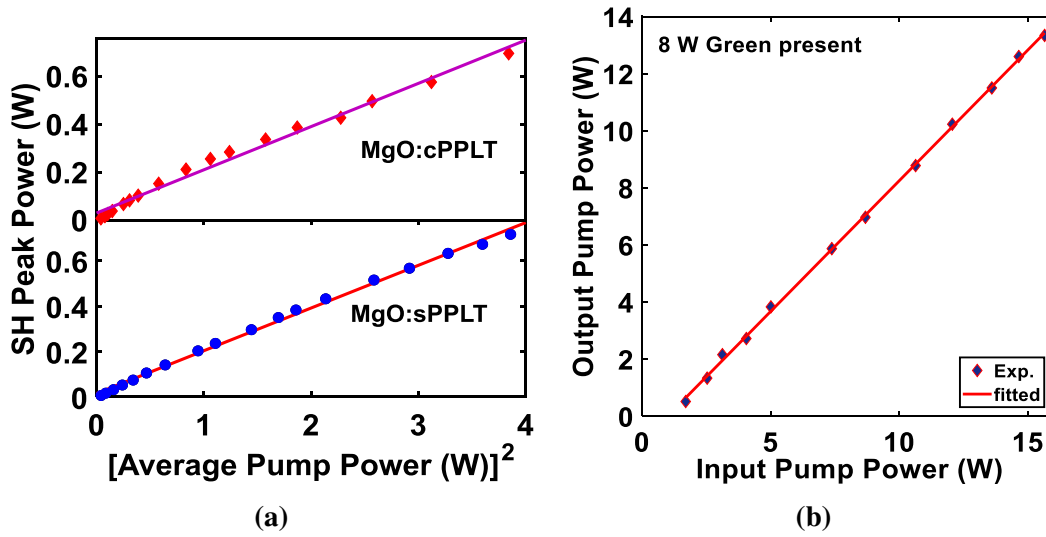


Figure 5.8 (a) Plot of the square of the average pump power along with the generated SH power MgO:cPPLT and MgO:sPPLT crystals. (b) In presence of 8 W green power generated from the MgO:sPPLT crystal the variation of the input pump power and the output pump in the MgO:cPPLT crystal.

and the generated SH power after the chopper. The variation of average SH power (P_{SH}) with square of the pump power (P_{pump}^2) is plotted in 5.8(a). It can be clearly observed from this figure that P_{SH} has a linear dependence with P_{pump}^2 i.e. $P_{SH} \propto P_{pump}^2$. This linear behaviour confirms that there is no back-conversion present in both nonlinear crystals. Further we investigated the absorption of the nonlinear crystals for 1064 nm and for 532 nm. For this we measured the transmitted power from both the crystal at 1064 nm as well as 532 nm. The plot between the input and the output powers exhibit linear variation. And for the calculation we utilised the Beer's and Lambert law which is $I_t = I_0 e^{-\alpha L} \Rightarrow \alpha = -\frac{\ln(I_t/I_0)}{L}$ where I_t is the transmitted intensity, I_0 is the incident intensity, α is the linear absorption coefficient and L is the crystal length. For MgO:cPPLT crystal we measured the linear absorption $\alpha = 1.05\%/cm$ at 1064 nm whereas $\alpha = 4.40\%/cm$ at 532 nm. And for MgO:sPPLT $\alpha = 0.38\%/cm$ at 1064 nm and $\alpha = 1.70\%/cm$ at 532 nm. The greater value of the absorption in MgO:cPPLT at pump as well as SH wavelengths is primary reason for subsequent thermal dephasing and early saturation in crystal. Here, it is also important to note that the thickness of

the MgO:cPPLT crystal was only 0.5 mm. This inhibits the heat distribution thereby escalating the impact of thermal dephasing. In order to get to know the impact of the third point *i.e.* GRIIRA which is green induced infrared absorption we performed another measurement. In this we have first generated 8 W green power from the MgO:sPPLT crystal. And further in presence of this green power we observed the transmittance of the pump power which is plotted in the Fig. 5.8(b). As can be seen in the Fig. 5.8(b) there is no nonlinear behaviour in the pump transmittance in presence of the green power. This measurement confirms the absence of GRIIRA in the MgO:cPPLT crystal. We could not observe the GRIIRA in the MgO:sPPLT crystal. However it is already reported that GRIIRA does not have any significant contribution in MgO:sPPLT at these power levels [91].

5.5.1 Power stability

Power stability test is the key measurement of a laser system. In this the performance of the laser will be tested over time. In order to realize this, we recorded the generated SH power from both the crystals over time at the maximum pump power. The MgO:cPPLT and MgO:sPPLT is operated at the focusing parameters of $\xi = 2.7$ and $\xi = 2.9$ and the pump power was 40 W. For about 4 hours we have recorded their performance over time which is shown in the Fig. 5.9. As can be seen in the Fig. 5.9, the frequency doubled green power shows a peak-to-peak variation of $\approx 11.4\%$ with its average power of 8.5 W for MgO:cPPLT. And it can also be observed from the Fig. 5.9(a) that the stability in the green power generated from MgO:cPPLT deteriorate rapidly after 3 hours of continuous operation. This is attributed to the accumulated thermal effects (ATE) which is due to the increased absorption at NIR and visible wavelengths in the MgO:cPPLT crystal. In order to understand this degradation we have also measured the generated SH power at relatively low pump power such as $P_{pump} = 10\text{ W}$ and $P_{pump} = 20\text{ W}$. It can be seen in the Fig. 5.9(a) that there is no such degradation happens in the case of low pump powers.

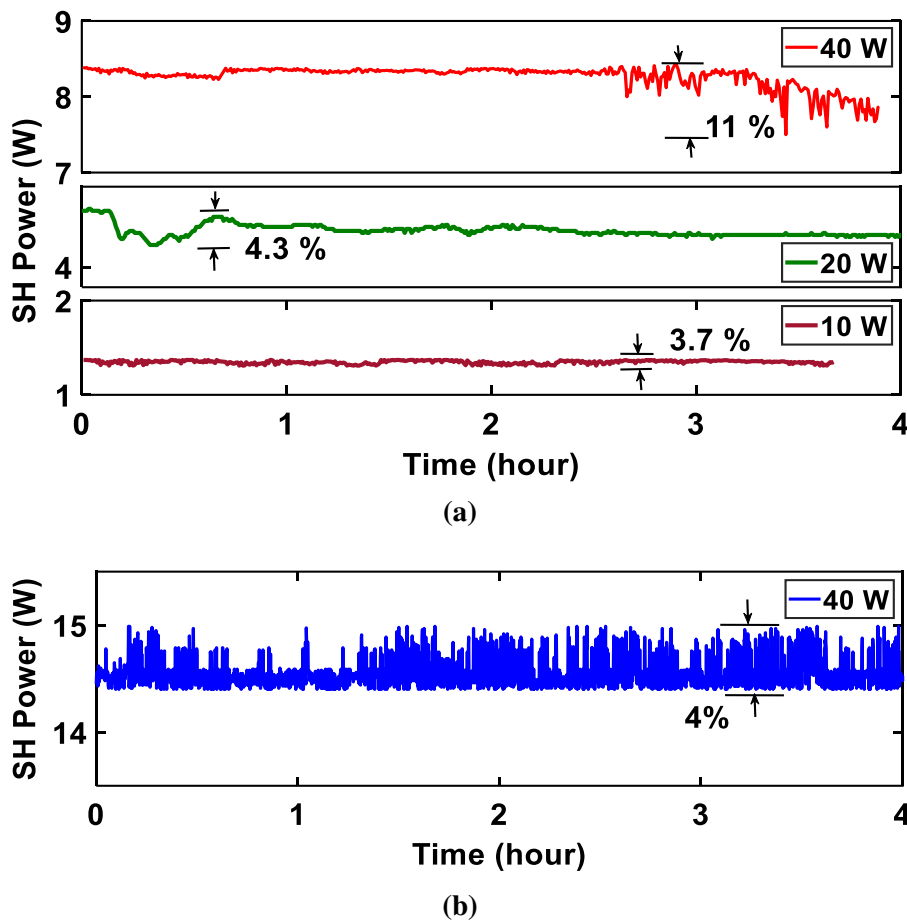


Figure 5.9 Stability measurement of the generated SH power in (a) MgO:cPPLT crystal at $P_{pump} \approx 10$ W, 20 W and 40 W. Rapid degradation in the SH power at 40W is due to the accumulated thermal effects. (b) Peak-to-peak power fluctuation in the MgO:sPPLT at $P_{pump} \approx 40$ W is $\approx 4\%$.

This provides concrete evidence that the ATE has significant contribution at high pump powers. For MgO:sPPLT we observed a power fluctuation of $\approx 4.1\%$ over a period of 1 hour. We did not observe any degradation at such high power in this crystal. This is basically due to its high thermal conductivity. It can also be noted that the pump power fluctuates $\approx 2\%$ in the same period of time. The power stability in the MgO:sPPLT crystal can be further improved by mainly two ways. One is to have an optimal oven design which can efficiently extract out the generated heat at high pump powers. The second one is to have a high resolution oven with which exact PM temperature can be achieved.

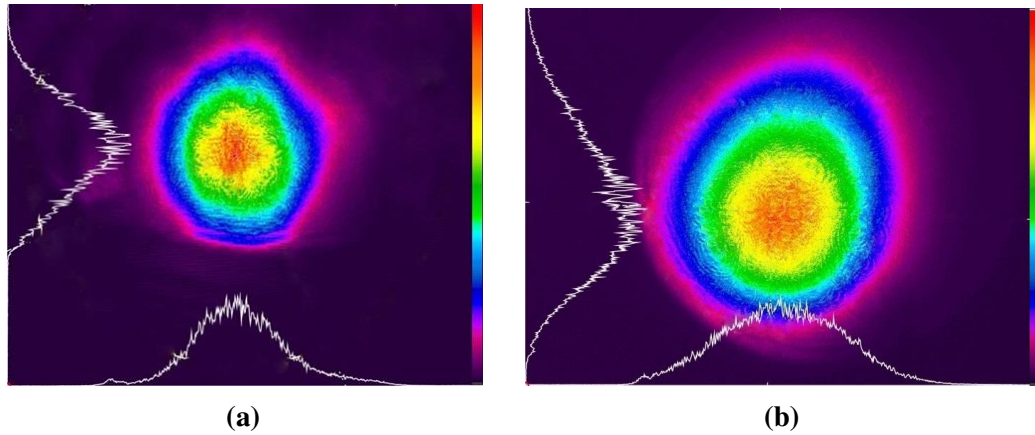


Figure 5.10 Transverse beam profile recorded with CCD camera for (a) MgO:cPPLT crystal and (b) MgO:sPPLT crystal.

5.5.2 M^2 and Beam-Profile

We have measured the M^2 of both the generated green beams at the maximum available pump which is $P_{pump} = 40\text{ W}$. It is measured with scanning beam profiler (NanoScan, Ophir). The lens used for this have focal length of $f = 200\text{ mm}$. By recording the beam size data from both sides of the focused Gaussian beam we calculated the M^2 . For the MgO:cPPLT crystal we calculated $M_x^2 = 1.11$ and $M_y^2 = 1.15$. And similarly for MgO:sPPLT we evaluated $M_x^2 = 1.12$ and $M_y^2 = 1.06$. It can also be noted here that the pump laser exhibit $M^2 = 1.05$.

We recorded the transverse beam profile of the generated SH beams from both the crystals. They are shown in the Fig. 5.10. They are captured from a CCD camera (Spiricon, Ophir). These transverse profiles confirm the Gaussian beam operating in the TEM_{00} mode for both the crystals.

5.5.3 Single frequency operation and frequency stability

We utilised the Fabry-Perot interferometer (FPI-100, Toptica) for the spectral measurement of the green beam from both the crystals. This measurement gives the confirmation about the generated beam for being single frequency and also the line-width is calculated

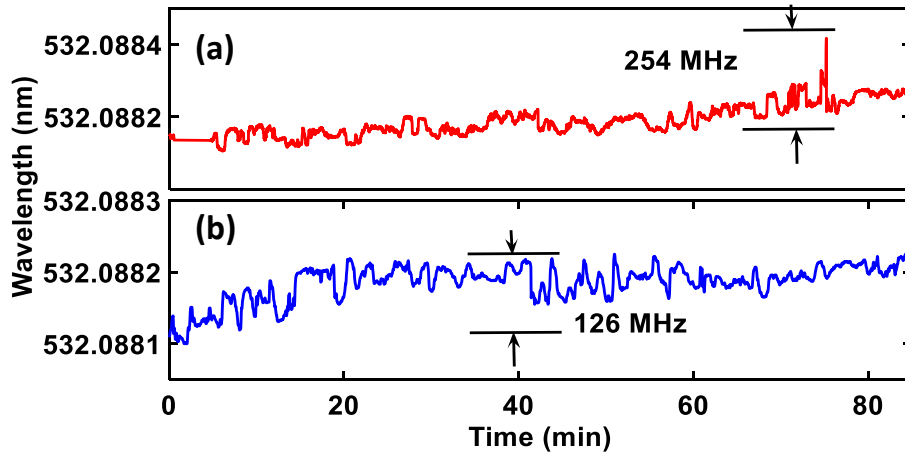


Figure 5.11 Peak-to-peak fluctuation in the wavelength of the generated SH from (a) MgO:cPPLT crystal and (b) MgO:sPPLT crystal.

from this. The FPI-100 has a free spectral range *i.e.* $FSR = 1GHz$ and the finesse of the cavity is ≈ 400 at the wavelength of interest. This measurement is also performed at the highest generated SH powers from both the crystals. The spectral trace within one ramp is shown in the Fig. 5.12(a) for MgO:cPPLT whereas Fig. 5.12(b) is for the crystal MgO:sPPLT. The FPI peaks in both the traces are of equal height and they are within one ramp. This confirms that the generated SH power is of single frequency. By extracting individual peaks we have calculated the line-width for both the crystals. The estimated line-width for the MgO:cPPLT is $\approx 12MHz$. And for the MgO:sPPLT crystal it is $\approx 5MHz$.

In order to perform the measurement of the frequency (or wavelength) stability, we have used a wavemeter (HighFinesse, GmbH). This wavemeter has a resolution of $\approx 10MHz$ and it works in the wavelength band of 220–1100 nm. We have recorded the wavelength for ≈ 90 min at the maximum available pump *i.e.* $P_{pump} = 40$ W. For the entire time duration the peak-to-peak fluctuation in the wavelength for both the crystals are plotted in the Fig. 5.11(a) and (b). As can be seen in the Fig. 5.11(a) the peak-to-peak fluctuation in the MgO:cPPLT crystal is $\approx 274MHz$ over the time. And for the same time frame this fluctuation in the MgO:sPPLT crystal is ≈ 126 MHz. This suggests that the

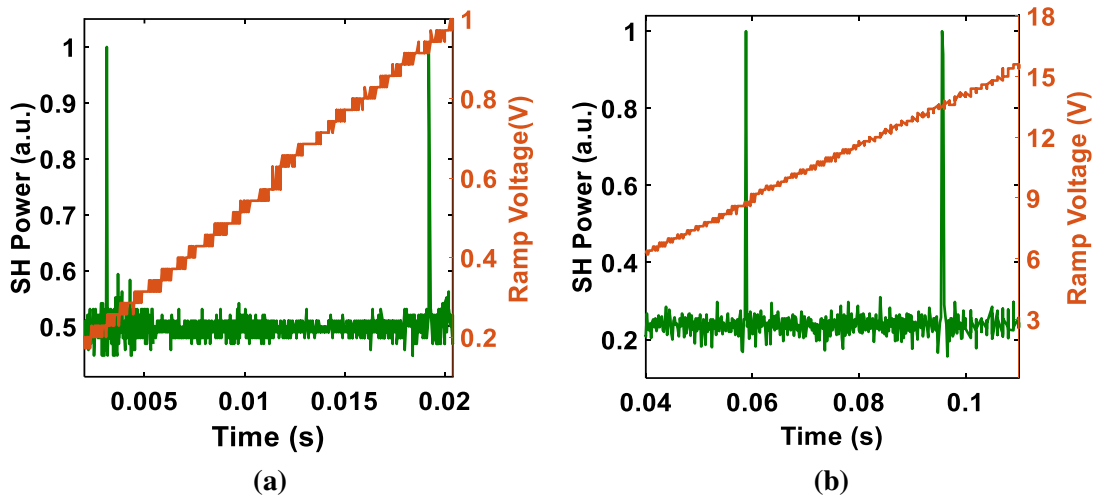


Figure 5.12 Fabry-Perot spectra of the (a) MgO:cPPLT and (b) MgO:sPPLT crystal.)

frequency drift for the MgO:cPPLT is more than double the frequency drift in the MgO:sPPLT crystal.

5.6 Conclusion

We have demonstrated two high power single frequency green laser sources. Both the sources are based on the QPM SHG. The nonlinear crystals are the same materials $LiTaO_3$ but their growth methods are different, one is congruent and the other is stoichiometric. A comparison based on their SHG performance is shown in the Table 5.1. The congruent variant of PPLT is 5 cm long whereas the stoichiometric one is 3 cm long. The conversion efficiency saturates early in the MgO:cPPLT showing its inefficient behaviour in the high power regime. This is basically due to the lower thermal conductivity of the crystal which does not allow the efficient heat extraction at high pump powers. The maximum observed conversion efficiency for this crystal was 24% with a maximum SH power of 8.5 W. However, we achieved 36 % conversion efficiency in the case of MgO:sPPLT crystal. And the maximum power observed for this crystal was 14.5 W. The other characteristics such as power stability and the frequency stability for the MgO:sPPLT thrived over the MgO:cPPLT crystal making it a better crystal for the SHG. These kind of sources are

Table 5.1 Properties of the generated SH power from the MgO:cPPLT and Mg:sPPLT crystals.

	Pump	cPPLT	sPPLT
Power (W)	40	8.5	14.5
Efficiency (%)	-	24	36
Power Fluctuation(%)	2	11	4
Single Frequency	Yes	Yes	Yes
Line-Width (MHz)	0.089	12	5
Frequency Fluctuation (MHz)	55	254	126
Mode Profile	TEM ₀₀	TEM ₀₀	TEM ₀₀
M ²	1.05	M _x ² ≤ 1.11 M _y ² ≤ 1.15	M _x ² ≤ 1.12 M _y ² ≤ 1.06

in high demand as a pump source for femtosecond *Ti : sapphire* lasers and also for the OPOs [107, 91]. They can also be utilised in the development of efficient solar cells.

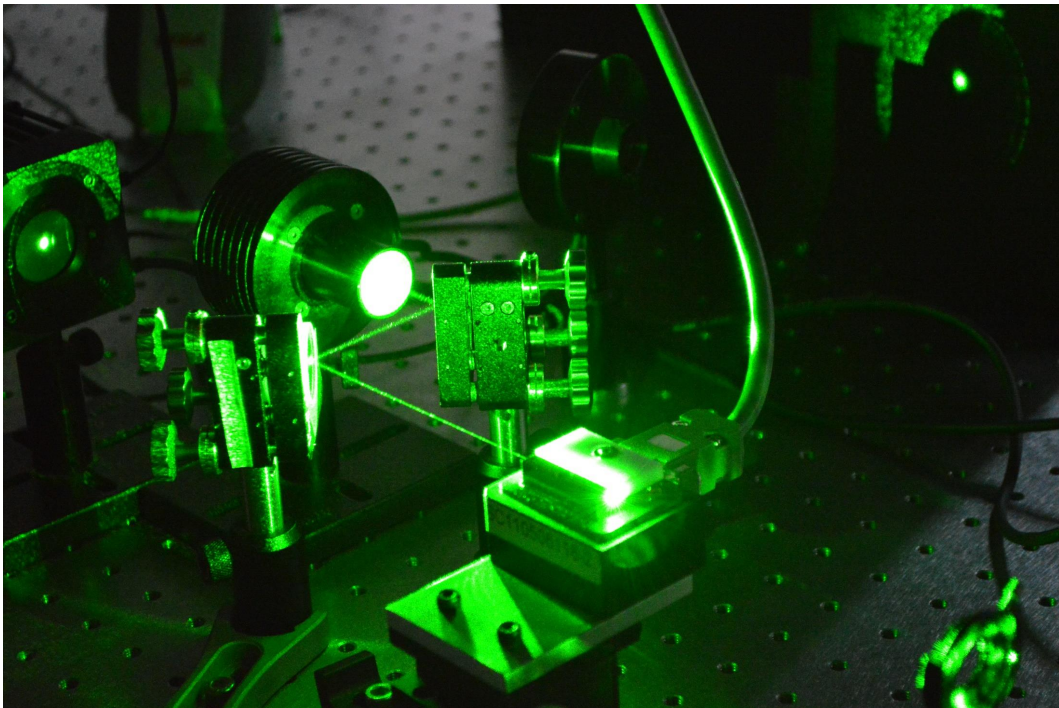


Figure 5.13 *A picture of generated SHG in the lab*

Chapter 6

Summary and future perspective

This thesis presents the experimental demonstration of CW singly-resonant optical parametric oscillators (SROs) which are tunable across broad electromagnetic spectrum. The unique feature associated with the demonstrated sources lies in the fact that they are all pumped by a high-power, single-frequency *Yb* – *fiber* laser operating at 1064 *nm*.

Our first demonstration includes a high-power single-frequency, tunable optical source delivering coherent radiation in the MIR as well as in NIR. The tunability in the SRO is achieved through dependence of refractive index on temperature for the *MgO* : *PPLN* crystal. The source is tunable across 3760 – 3970 *nm* in the MIR in addition to broad tunable band across 1450 – 1483 *nm* in the NIR. The maximum power 2 *W* at a wavelength of 3895 *nm* is obtained at a pump power of ≈ 16 *W*. However, in the MIR band, the power is ≈ 1 *W* across the entire tunable band. Interestingly, we observed sidebands in the signal spectrum across the tunable spectrum which we attribute to the stimulated polariton scattering as the nonlinear crystal *LiNbO*₃. This is primarily due to large number of ‘optical phonon’ modes existing in *LiNbO*₃ crystal which renders it Raman-active as well as infrared-active. In order to suppress these modes, we have introduced additional cavity losses through signal beam out-coupling which inevitably reduces the cavity finesse and consequently, increases the SRO threshold to ≈ 7 *W*. Through this route, we were able to obtain appreciable out-coupled signal power which could be employed for different

applications. We obtained a maximum out-coupled power of 4 W at a wavelength of 1465 nm. On an average, the power in the signal beam remained ≈ 2 W across the entire tunable band. Further, we characterized the coherent source by carrying out the power stability measurements for the signal as well as the idler over an ≈ 1 hour at the maximum pump power and free-running conditions. This resulted in signal and idler beam fluctuations (about the mean) to be $\approx 4.7\%$ and 1.9% respectively. The fluctuations in the frequency or wavelength of the signal beam is measured over an hour under free-running conditions which was estimated to be ≈ 41 GHz. The single-frequency for the signal beam is confirmed through the spectrum of scanning Fabry-Perot interferometer which provided signal linewidth of 22.5 MHz.

In a second experiment, we have carried out intra-cavity SHG of the signal beam of mid-infrared SRO. The cavity in this experiment is a six-mirror ring cavity which ensures focusing of the generated signal beam at a beam-waist of 65 μm inside the cavity. Due of the extra additional cavity losses, the stimulated Raman modes in the signal beam vanish. Further, we employ 10 mm long BBO and BIBO crystals to perform the SHG of intra-cavity signal which results in single-frequency tunable radiation in the visible/NIR. We obtained coarsely tunable visible radiation in the wavelength band of 753 – 780 nm. With the BBO crystal, we obtained a maximum SHG power of 2 W at a wavelength of 756 nm whereas the BIBO crystal facilitates the generation of a ≈ 4 W of power at 758 nm. This is essentially attributed to the fact that the BIBO exhibit higher value of nonlinear coefficient (d_{eff}) than BBO along with improved thermal management characteristics. We characterised both the sources based on their performance under free-running conditions and consequently, we measured the random fluctuations in output power as well as frequency of radiation. The single-frequency operation was confirmed from the spectral measurements of scanning Fabry-Perot interferometer which also facilitated the measurement of linewidth of signal as well as visible/NIR radiation.

Further, we have demonstrated high-power green laser source by frequency doubling of a Yb – fiber laser in two separate configurations. In order to accomplish this, a

straightforward single-pass scheme is employed. The experiment involves two variants of periodically-poled $LiTaO_3$ (or *PPLT*) crystal, namely MgO-doped congruently-grown PPLT crystal (MgO:cPPLT) and stoichiometrically-grown PPLT (MgO:sPPLT) crystal. In two different experiments, we have generated 8.5 W and 14.5 W of power at a wavelength of 532 nm respectively. Although, MgO:cPPLT crystal is longer than the MgO:sPPLT crystal, we observed an onset of early saturation in the generated green radiation from MgO:cPPLT crystal. In order to gain some physical insight, we investigated the possibilities of back-conversion, thermally-induced dephasing, and green-induced infrared absorption (GRIIRA). These studies reveal that the saturation in MgO:cPPLT crystal is a consequence of the cumulative thermal dephasing arising out of accumulated thermal effects. This manifestation is essentially governed by weaker thermal conductivity of MgO:cPPLT crystal. In order to characterize the generated green beam from both the crystals, we recorded the power-stability and frequency-stability for more than 4 – hours at a maximum pump power of ≈ 40 W and under free-running conditions. We observed a 11.4% fluctuation in the green power from the MgO:cPPLT crystal. However, the power fluctuations in the green beam for MgO:sPPLT crystal was measured to be $\approx 4\%$. The observed frequency fluctuation in green power was 254 MHz and 126 MHz for MgO:cPPLT and MgO:sPPLT crystals respectively. The spatial and temporal beam qualities of the green beam were also measured for both the experiments. It was found that the green beam exhibit Gaussian beam profile in TEM_{00} mode with good M^2 values.

The present thesis revolves around discussion on tunable CW laser sources in the visible, in the NIR and in the MIR spectral band. Also, in the SRO configuration, we have utilized two gratings of the periodically-poled $LiNbO_3$ crystal only. The tunability could be further enhanced by selecting other grating periods of the nonlinear crystal *e.g.* the use of $\Lambda = 28.5 \mu m$ for the PPLN crystal could have resulted in generation of 4 μm MIR. Shorter wavelengths of the visible spectra could also be covered by optimally frequency-doubling the generated signal. The generation of radiation due to the phenomenon of SPS in the SRO configuration could be a potential source for generating THz radiation

efficiently. By using silicon prisms, the generated THz radiation in the PPLN crystal (due to SPS) could be extracted and characterised. SPS modes could also be for efficient THz generation in intra-cavity configurations. In order to accomplish this, THz generating crystals such as DAST or BNA can be appropriately positioned within the SRO cavity and using the parabolic mirrors, the THz could be detected.

In case of SRO to be used for spectroscopic applications, the frequency fluctuations and output power fluctuations from the SRO could be improved significantly by deploying active-frequency stabilisation techniques and better thermal management schemes respectively. For example, thermal ovens (for housing the nonlinear crystals) would be designed which exhibit better resolution along with selective heating of the crystal for efficient heat extraction.

Finally, as an important future work related to this, we propose to generate a tunable ultra-violet radiation using Yb-doped fiber laser operating at 1064 *nm* wavelength. The design essentially depends on efficient intra-cavity frequency-quadrupling of NIR/MIR signal. Such a configuration along with its compact feature would be an apt coherent source for laser projector technology which simultaneously employ red-green-blue (RGB) sources.

Bibliography

- [1] C. H. Townes, *How the Laser Happened: Adventures of a Scientist*. Oxford University Press, USA, 1999.
- [2] A. L. Schawlow and C. H. Townes, “Infrared and optical masers,” *Phys. Rev.*, vol. 112, pp. 1940–1949, 1958.
- [3] W. Koechner, *Solid-State Laser Engineering*. Springer-Verlag, New York, USA, 6th ed., 2011.
- [4] T. H. Maiman, “Stimulated optical radiation in ruby,” *Nature*, vol. 187, no. 4736, pp. 493–494, 1960.
- [5] A. Javan, W. R. Bennett, and D. R. Herriott, “Population inversion and continuous optical maser oscillation in a gas discharge containing a He–Ne mixture,” *Phys. Rev. Lett.*, vol. 6, pp. 106–110, 1961.
- [6] M. H. Anderson, J. R. Ensher, M. R. Matthews, C. E. Wieman, and E. A. Cornell, “Observation of Bose-Einstein Condensation in a Dilute Atomic Vapor,” *Science*, vol. 269, no. 5221, pp. 198–201, 1995.
- [7] B. P. Abbott *et al.*, “Observation of Gravitational Waves from a Binary Black Hole Merger,” *Phys. Rev. Lett.*, vol. 116, pp. 061102–16, Feb 2016.
- [8] R. L. Byer, “Nonlinear optics and solid-state lasers: 2000,” *IEEE J. Sel. Top. Quant. Electron.*, vol. 6, pp. 911–930, Nov. 2000.

- [9] A. E. Willner, R. L. Byer, C. J. Chang-Hasnain, S. R. Forrest, H. Kressel, H. Kogelnik, G. J. Tearney, C. H. Townes, and M. N. Zervas, "Optics and photonics: Key enabling technologies," *Proc. IEEE*, vol. 100, pp. 1604–1643, May 2012.
- [10] P. A. Franken, A. E. Hill, C. W. Peters, and G. Weinreich, "Generation of Optical Harmonics," *Phys. Rev. Lett.*, vol. 7, pp. 118–119, Aug. 1961.
- [11] J. Kerr, "A new relation between electricity and light: Dielectrified media birefringent," *Philosophical Magazine Series 4*, vol. 50, no. 332, pp. 337–348, 1875.
- [12] J. Kerr, "Electro-optic observation on various liquids," *Philosophical Magazine Series 5*, vol. 8, no. 47, pp. 85–102, 1879.
- [13] R. C. Gray, "The Rev. John Kerr, F.R.S., Inventor of the Kerr Cell," *Nature*, vol. 136, pp. 245–247, 1935.
- [14] C. V. Raman and K. S. Krishnan, "A new type of secondary radiation," *Nature*, vol. 121, pp. 501–502, 1928.
- [15] E. Schrodinger, "Nonlinear optics," *Proc. Royal Irish Academy*, vol. 47A, pp. 77–117, 1942.
- [16] E. Schrodinger, "A new exact solution in non-linear optics," *Proc. Royal Irish Academy*, vol. 49 A, pp. 59–66, 1943.
- [17] R. W. Boyd, *Nonlinear Optics*. Academic Press, Elsevier, UK, 3rd ed., 2009.
- [18] A. V. Smith, "How to use SNLO nonlinear optics software to select nonlinear crystals and model their performance," *Proc. SPIE*, vol. 4972, pp. 4972 – 4980, 2003.
- [19] D. N. Nikogosyan, *Nonlinear Optical Crystals: A Complete Survey*. Springer-Verlag, New York, 2005.

- [20] J. A. Giordmaine and R. C. Miller, "Tunable Coherent Parametric Oscillation in $LiNbO_3$ at Optical Frequencies," *Phys. Rev. Lett.*, vol. 14, pp. 973–976, Jun 1965.
- [21] M. H. Dunn and M. Ebrahimzadeh, "Parametric generation of tunable light from continuous-wave to femtosecond pulses," *Science*, vol. 286, no. 5444, pp. 1513–1517, 1999.
- [22] P. J. Smith, N. Blunt, M. Wiltshire, T. Hoy, P. Teesdale-Spittle, M. R. Craven, J. V. Watson, W. Brad Amos, R. J. Errington, and L. H. Patterson, "Characteristics of a novel deep red/infrared fluorescent cell-permeant DNA probe, DRAQ5, in intact human cells analyzed by flow cytometry, confocal and multiphoton microscopy," *Cytometry*, vol. 40, no. 4, pp. 280–291, 2000.
- [23] R. Lubart, H. Friedmann, M. Sinyakov, N. Cohen, and H. Breitbart, "Changes in calcium transport in mammalian sperm mitochondria and plasma membranes caused by 780 nm irradiation," *Lasers Surg. Med.*, vol. 21, no. 5, pp. 493–499, 1997.
- [24] H. G. Breunig, H. Studier, and K. Konig, "Multiphoton excitation characteristics of cellular fluorophores of human skin in vivo," *Opt. Exp.*, vol. 18, pp. 7857–7871, Apr 2010.
- [25] H. J. Butler, L. Ashton, B. Bird, G. Cinque, K. Curtis, J. Dorney, K. Esmonde-White, N. J. Fullwood, B. Gardner, P. L. Martin-Hirsch, M. J. Walsh, M. R. McAinsh, N. Stone, and F. L. Martin, "Using Raman spectroscopy to characterize biological materials," *Nature Protocols*, vol. 11, p. 664, Mar. 2016.
- [26] M. van Herpen, S. Li, S. Bisson, S. te Lintel Hekkert, and F. Harren, "Tuning and stability of a continuous-wave mid-infrared high-power single resonant optical parametric oscillator," *Appl. Phys. B: Lasers and Optics*, vol. 75, pp. 329–333, Sep 2002.

- [27] M. Vainio and L. Halonen, “Mid-infrared optical parametric oscillators and frequency combs for molecular spectroscopy,” *Phys. Chem. Chem. Phys.*, vol. 18, no. 6, pp. 4266–4294, 2016.
- [28] S. T. Yang, R. C. Eckardt, and R. L. Byer, “Continuous-wave singly resonant optical parametric oscillator pumped by a single-frequency resonantly doubled nd:yag laser,” *Opt. Lett.*, vol. 18, pp. 971–3, Jun 1993.
- [29] M. K. Shukla and R. Das, “High-Power Single-Frequency Source in the Mid-Infrared Using a Singly Resonant Optical Parametric Oscillator Pumped by Yb-Fiber Laser,” *IEEE J. Sel. Top. Quant. Electron.*, vol. 24, pp. 1–6, Sep 2018.
- [30] M. K. Shukla, P. S. Maji, and R. Das, “Yb-fiber laser pumped high-power, broadly tunable, single-frequency red source based on a singly resonant optical parametric oscillator,” *Opt. Lett.*, vol. 41, no. 13, p. 3033, 2016.
- [31] M. K. Shukla, S. Kumar, and R. Das, “Single-Pass Multi-Watt Second-Harmonic-Generation in Congruent and Stoichiometric $LiTaO_3$,” *IEEE Photon. Technol. Lett.*, vol. 27, pp. 1379–1382, Jul 2015.
- [32] M. G. Kuzyk, *Lecture notes in nonlinear optics: A students perspective*. NLOsource.com, 1st ed., 2013.
- [33] W. P. Risk, T. R. Gosnell, and A. V. Nurmikko, *Compact Blue Green Lasers*. Cambridge: Cambridge University Press, 2003.
- [34] K. Thyagarajan and A. K. Ghatak, *Lasers: Fundamentals and Applications*. Macmillan India, 2nd ed., 2011.
- [35] D. Zhang, Y. Kong, and J.-y. Zhang, “Optical parametric properties of 532-nm-pumped beta-barium-borate near the infrared absorption edge,” *Opt. Commun.*, vol. 184, no. 5, pp. 485 – 491, 2000.

- [36] J. A. Armstrong, N. Bloembergen, J. Ducuing, and P. S. Pershan, "Interactions between Light Waves in a Nonlinear Dielectric," *Phys. Rev.*, vol. 127, pp. 1918–1939, Sep. 1962.
- [37] M. M. Fejer, G. A. Magel, D. H. Jundt, and R. L. Byer, "Quasi-phase-matched second harmonic generation: tuning and tolerances," *IEEE J. Quant. Electron.*, vol. 28, pp. 2631–2654, Nov. 1992.
- [38] S. E. Harris, "Tunable optical parametric oscillators," *Proc. IEEE*, vol. 57, pp. 2096–2113, Dec. 1969.
- [39] R. G. Smith, J. E. Geusic, H. J. Levinstein, J. J. Rubin, S. Singh, and L. G. Van Uitert, "Continuous optical parametric oscillation in $Ba_2NaNb_5O_{15}$," *Appl. Phys. Lett.*, vol. 12, no. 9, pp. 308–310, 1968.
- [40] R. L. Byer, M. K. Oshman, J. F. Young, and S. E. Harris, "Visible CW Parametric Oscillator," *Appl. Phys. Lett.*, vol. 13, no. 3, pp. 109–111, 1968.
- [41] M. Ebrahim-Zadeh and M. H. Dunn, "Optical Parametric Oscillators," in *OSA Handbook of Optics*, vol. 4, ch. 22, pp. 1–67, 2010.
- [42] O. Paul, A. Quosig, T. Bauer, and M. Nittmann, "Temperature-dependent Sellmeier equation in the MIR for the extraordinary refractive index of 5% MgO doped congruent $LiNbO_3$," *Appl. Phys. B: Lasers and Optics*, vol. 115, pp. 111–115, 2007.
- [43] A. Siegman, *Lasers*. University Science Books, Sausalito, California, 1986.
- [44] G. D. Boyd and D. A. Kleinman, "Parametric interaction of focused Gaussian light beams," *J. Appl. Phys.*, vol. 39, pp. 3597–3639, Jul. 1968.
- [45] M. Veithen and P. Ghosez, "First-principles study of the dielectric and dynamical properties of lithium niobate," *Phys. Rev. B*, vol. 65, no. 21, p. 214302, 2002.

- [46] P. Hermet, M. Veithen, and P. Ghosez, “First-principles calculations of the nonlinear optical susceptibilities and Raman scattering spectra of lithium niobate,” *J. Phys. : Condensed Matter*, vol. 19, no. 45, p. 456202, 2007.
- [47] A. Lee, Y. He, and H. Pask, “Frequency-tunable thz source based on stimulated polariton scattering in *rmMg:LiNbO₃*,” *IEEE J. Quant. Electron.*, vol. 49, pp. 357–364, Mar. 2013.
- [48] A. M. Warriier, J. Lin, H. M. Pask, A. J. Lee, and D. J. Spence, “Multiwavelength ultrafast *LiNbO₃* Raman laser,” *Opt. Exp.*, vol. 23, no. 20, p. 25582, 2015.
- [49] A. Barker and R. Loudon, “Dielectric Properties and Optical Phonons in *LiNbO₃*,” *Phys. Rev.*, vol. 158, no. 2, pp. 433–445, 1967.
- [50] H. E. Puthoff, R. H. Pantell, B. G. Huth, and M. A. Chacon, “Near-Forward Raman Scattering in *LiNbO₃*,” *J. Appl. Phys.*, vol. 39, no. 4, pp. 2144–2146, 1968.
- [51] D. L. Mills and E. Burstein, “Polaritons: the electromagnetic modes of media,” *Rep. Prog. Phys.*, vol. 37, no. 7, p. 817, 1974.
- [52] G. Butcher, *Tour of the electromagnetic spectrum*. Washington, D.C.: National Aeronautics and Space Administration, 2016.
- [53] A. A. Richards, *Alien Vision: Exploring the Electromagnetic Spectrum with Imaging Technology*. SPIE press, 2001.
- [54] K. L. Sorokina, Irina T.; Vodopyanov, *Solid-State Mid-Infrared Laser Sources*, vol. 10.1007/3-540-36491-9, pp. 409–436. 2003.
- [55] F. K. Tittel, D. Richter, and A. Fried, “Mid-infrared laser applications in spectroscopy,” in *Solid-State Mid-Infrared Laser Sources* (I. T. Sorokina and K. L. Vodopyanov, eds.), pp. 458–529, Berlin, Heidelberg: Springer Berlin Heidelberg, 2003.

- [56] B. M. Walsh, H. R. Lee, and N. P. Barnes, "Mid infrared lasers for remote sensing applications," *Journal of Luminescence*, vol. 169, pp. 400–405, 2016.
- [57] I. Breunig, D. Haertle, and K. Buse, "Continuous-wave optical parametric oscillators: Recent developments and prospects," *Appl. Phys. B: Lasers and Optics*, vol. 105, no. 1, pp. 99–111, 2011.
- [58] Y. Yao, A. J. Hoffman, and C. F. Gmachl, "Mid-infrared quantum cascade lasers," *Nature Photon.*, vol. 6, p. 432, June 2012.
- [59] F. Capasso, C. Gmachl, R. Paiella, A. Tredicucci, A. L. Hutchinson, D. L. Sivco, J. N. Baillargeon, A. Y. Cho, and H. C. Liu, "New frontiers in quantum cascade lasers and applications," *IEEE J. Sel. Top. Quant. Electron.*, vol. 6, pp. 931–947, Nov. 2000.
- [60] J. F. Butler, A. R. Calawa, R. J. Phelan, T. C. Harman, A. J. Strauss, and R. H. Rediker, "PbTe Diode Laser," *Appl. Phys. Lett.*, vol. 5, no. 4, pp. 75–77, 1964.
- [61] H. Preier, "Physics and applications of IV-VI compound semiconductor lasers," *Semiconductor Science and Technology*, vol. 5, no. 3S, p. S12, 1990.
- [62] R. H. Rediker, "Semiconductor diode luminescence and lasers. A perspective," *IEEE J. Sel. Top. Quant. Electron.*, vol. 6, no. 6, pp. 1355–1362, 2000.
- [63] L. D. DeLoach, R. H. Page, G. D. Wilke, S. A. Payne, and W. F. Krupke, "Transition metal-doped zinc chalcogenides: spectroscopy and laser demonstration of a new class of gain media," *IEEE J. Quant. Electron.*, vol. 32, no. 6, pp. 885–895, 1996.
- [64] S. B. Mirov, V. V. Fedorov, D. Martyshkin, I. S. Moskalev, M. Mirov, and S. Vasilyev, "Progress in Mid-IR Lasers Based on Cr and Fe-Doped II-VI Chalcogenides," *IEEE J. Sel. Top. Quant. Electron.*, vol. 21, no. 1, pp. 292–310, 2015.

- [65] R. C. Eckardt, H. Masuda, Y. X. Fan, and R. L. Byer, "Absolute and relative nonlinear optical coefficients of KDP, KD*P, BaB_2O_4 , $LiIO_3$, $MgO:LiNbO_3$, and KTP measured by phase-matched second-harmonic generation," *IEEE J. Quant. Electron.*, vol. 26, no. 5, pp. 922–933, 1990.
- [66] M. M. J. W. van Herpen, S. E. Bisson, and F. J. M. Harren, "Continuous-wave operation of a single-frequency optical parametric oscillator at $4 - 5\mu m$ based on periodically poled $LiNbO_3$," *Opt. Lett.*, vol. 28, no. 24, pp. 2497–2499, 2003.
- [67] A. Silva and I. D. Lindsay, "Wavelength-swept optical parametric oscillator for broadband mid-infrared spectroscopy," *Appl. Phys. B: Lasers and Optics*, vol. 107, pp. 685–689, Feb. 2012.
- [68] M. Siltanen, M. Vainio, and L. Halonen, "Pump-tunable continuous-wave singly resonant optical parametric oscillator from 2.5 to $4.4\mu m$," *Opt. Exp.*, vol. 18, pp. 14087–14092, Jun. 2010.
- [69] A. Henderson and R. Stafford, "Low threshold, singly-resonant CW OPO pumped by an all-fiber pump source," *Opt. Exp.*, vol. 14, pp. 767–772, Jan. 2006.
- [70] A. J. Henderson, R. Stafford, and P. Hoffman, "Long-Term Frequency-Stable Operation of a Single Frequency CW OPO without Active Locking," in *Laser Applications to Chemical, Security and Environmental Analysis*, p. LMC2, Optical Society of America, 2008.
- [71] A. Henderson and R. Stafford, "Intra-cavity power effects in singly resonant CW OPOs," *Appl. Phys. B*, vol. 85, pp. 181–184, Jun. 2006.
- [72] M. Vainio, J. Peltola, S. Persijn, F. J. M. Harren, and L. Halonen, "Thermal effects in singly resonant continuous-wave optical parametric oscillators," *Applied Physics B*, vol. 94, p. 411, Nov. 2008.

- [73] K. Devi, S. C. Kumar, and M. Ebrahim-Zadeh, "High-power, continuous-wave, single-frequency, all-periodically-poled, near-infrared source," *Opt. Lett.*, vol. 37, pp. 5049–5051, Dec. 2012.
- [74] R. Sowade, I. Breunig, J. Kiessling, and K. Buse, "Influence of the pump threshold on the single-frequency output power of singly resonant optical parametric oscillators," *Appl. Phys. B: Lasers and Optics*, vol. 96, pp. 25–28, Dec. 2009.
- [75] E. Lippert, H. Fonnum, G. Arisholm, and K. Stenersen, "A 22-watt mid-infrared optical parametric oscillator with V-shaped 3-mirror ring resonator," *Opt. Exp.*, vol. 18, pp. 26475–26483, Mar. 2010.
- [76] Q. Sheng, X. Ding, C. Shi, S. Yin, B. Li, C. Shang, X. Yu, W. Wen, and J. Yao, "Continuous-wave mid-infrared intra-cavity singly resonant PPLN-OPO under 880 nm in-band pumping," *Opt. Exp.*, vol. 20, pp. 8041–8046, Mar. 2012.
- [77] S. Guha, "Focusing dependence of the efficiency of a singly resonant optical parametric oscillator," *Appl. Phys. B*, vol. 66, pp. 663–675, Apr. 1998.
- [78] M. K. Shukla, S. Kumar, and R. Das, "High-power, single-frequency, single-pass second-harmonic-generation by optimally focused yb-fiber laser," in *Advanced Solid State Lasers*, p. ATh2A.22, Optical Society of America, 2014.
- [79] A. V. Okishev and J. D. Zuegel, "Intracavity-pumped Raman laser action in a mid IR, continuous-wave (cw) MgO: PPLN optical parametric oscillator," *Opt. express*, vol. 14, pp. 12169–12173, Dec. 2006.
- [80] A. Henderson and R. Stafford, "Spectral broadening and stimulated Raman conversion in a continuous-wave optical parametric oscillator," *Opt. Lett.*, vol. 32, pp. 1281–1283, May 2007.

- [81] T.-H. My, O. Robin, O. Mhibik, C. Drag, and F. Bretenaker, “Stimulated Raman scattering in an optical parametric oscillator based on periodically poled MgO-doped stoichiometric $LiTaO_3$,” *Opt. Exp.*, vol. 17, pp. 5912–5918, Mar. 2009.
- [82] A. M. Warriar, R. Li, J. Lin, A. J. Lee, H. M. Pask, and D. J. Spence, “Tunable terahertz generation in the picosecond regime from the stimulated polariton scattering in a $LiNbO_3$ crystal,” *Opt. Lett.*, vol. 41, pp. 4409–4412, Sep. 2016.
- [83] O. Mhibik, T.-H. My, D. Pabœuf, F. Bretenaker, and C. Drag, “Frequency stabilization at the kilohertz level of a continuous intracavity frequency-doubled singly resonant optical parametric oscillator,” *Opt. Lett.*, vol. 35, pp. 2364–2366, Jul. 2010.
- [84] A. Foltynowicz, P. Masłowski, A. J. Fleisher, B. J. Bjork, and J. Ye, “Cavity-enhanced optical frequency comb spectroscopy in the mid-infrared application to trace detection of hydrogen peroxide,” *Appl. Phys. B*, vol. 110, pp. 163–175, Feb. 2013.
- [85] B. R. Wood, P. Caspers, G. J. Puppels, S. Pandiancherri, and D. McNaughton, “Resonance raman spectroscopy of red blood cells using near-infrared laser excitation,” *Analytical and Bioanalytical Chemistry*, vol. 387, pp. 1691–1703, Mar. 2007.
- [86] W. R. Zipfel, R. M. Williams, and W. W. Webb, “Nonlinear magic: multiphoton microscopy in the biosciences,” *Nature Biotechnology*, vol. 21, pp. 1369–1377, Oct. 2003.
- [87] P. F. Moulton, “Spectroscopic and laser characteristics of $Ti : Al_2O_3$,” *J. Opt. Soc. Am. B*, vol. 3, pp. 125–133, Jan. 1986.
- [88] P. F. Moulton, “Titanium-doped sapphire laser research and design study,” *NASA*, pp. 1–59, 1987.

- [89] W. R. Rapoport and C. P. Khattak, "Titanium sapphire laser characteristics," *Appl. Opt.*, vol. 27, pp. 2677–2684, Jul. 1988.
- [90] T.-H. My, C. Drag, and F. Bretenaker, "Single-frequency and tunable operation of a continuous intracavity-frequency-doubled singly resonant optical parametric oscillator," *Opt. Lett.*, vol. 33, pp. 1455–1457, Jul. 2008.
- [91] G. K. Samanta, S. C. Kumar, R. Das, and M. Ebrahim-Zadeh, "Continuous-wave optical parametric oscillator pumped by a fiber laser green source at 532 nm," *Opt. Lett.*, vol. 34, pp. 2255–2257, Aug. 2009.
- [92] D. Sands, *Diode Lasers*. Institute of Physics publishing, Bristol, 2005.
- [93] <https://www.thorlabs.com/catalogpages/693.pdf>.
- [94] M. K. Shukla, S. Kumar, and R. Das, "Single-pass, efficient type-I phase-matched frequency doubling of high-power ultrashort-pulse Yb-fiber laser using LiB_3O_5 ," *Applied Physics B*, vol. 122, p. 114, Apr. 2016.
- [95] L. B. Kreuzer, "Single and multilode oscillation of the singly resonant optical parametric oscillator," in *Proceedings of the joint conference on Lasers and Electro-optics*, p. 52, The Institution of Electronic and Radio Engineers, March 1969.
- [96] K. S. Zhang, T. Coudreau, M. Martinelli, A. Maître, and C. Fabre, "Generation of bright squeezed light at $1.06 \mu\text{m}$ using cascaded nonlinearities in a triply resonant cw periodically-poled lithium niobate optical parametric oscillator," *Phys. Rev. A*, vol. 64, pp. 033815–7, Aug. 2001.
- [97] O. Crisafulli, N. Tezak, D. B. S. Soh, M. A. Armen, and H. Mabuchi, "Squeezed light in an optical parametric oscillator network with coherent feedback quantum control," *Opt. Express*, vol. 21, pp. 18371–18386, Jul. 2013.
- [98] J. B. Pawley, *Handbook of Biological Confocal Microscopy*. Springer, USA, 2006.

- [99] S. Brustlein, P. Ferrand, N. Walther, S. Brasselet, H. Rigneault, C. Billaudeau, and D. D. Marguet, “Optical parametric oscillator-based light source for coherent raman scattering microscopy: practical overview,” *Journal of Biomedical Optics*, vol. 16, Feb.
- [100] J. Roufs, *Light as a true visual quantity : principles of measurement*. CIE publication, International Commission on Illumination, 1978.
- [101] J. J. Vos, “Colorimetric and photometric properties of a 2° fundamental observer,” *Color Research & Application*, vol. 3, no. 3, pp. 125–128, 1978.
- [102] E. Schubert, *Light-Emitting Diodes*. Cambridge University Press, 2006.
- [103] D. Sizov, R. Bhat, and C. E. Zah, “Gallium Indium Nitride-Based Green Lasers,” *J. Lightwave Technol.*, vol. 30, pp. 679–699, Mar. 2012.
- [104] K. Moutzouris and G. Hloupis, “Temperature-dependent visible to near-infrared optical properties of 8 mol% Mg-doped lithium tantalate,” *Opt. Mater.*, vol. 1, no. 3, pp. 400–402, 2011.
- [105] A. Bruner, D. Eger, M. B. Oron, and P. Blau, “Temperature-dependent Sellmeier equation for the refractive index of stoichiometric lithium tantalate,” *Opt. Lett.*, vol. 28, no. 3, pp. 194–196, 2003.
- [106] F. R. Nash, G. D. Boyd, M. Sargent III and P. M. Bridenbaugh, “Effect of Optical Inhomogeneities on Phase Matching in Nonlinear Crystals,” *Journal of Applied Physics*, vol. 41, no. 6, pp. 2564–2576, 1970.
- [107] S. Sawai, A. Hosaka, H. Kawauchi, K. Hiroswawa, and F. Kannari, “Demonstration of a Ti:sapphire mode-locked laser pumped directly with a green diode laser,” *Appl. Phys. Exp.*, vol. 7, no. 2, pp. 022702–3, 2014.

Appendix A

Mirror characterization

The schematic to measure the reflectivity of the mirror M_6 used in chapter 4 is shown in the Fig. A.1. In order to accomplish the measurement, we perform the optical parametric generation (OPG) in MgO:PPLN (same as used in chapter 4) crystal. The pump source for this experiment is a nanosecond laser (Bright-Solutions, Italy). This laser delivers sub-nanosecond ($\approx 0.7 \text{ ns}$) pulses at two different wavelengths 1064 nm and 532 nm . For the present measurement, we have used the 1064 nm beam. At 80 kHz repetition rate, the maximum power in 1064 nm beam is $\approx 2 \text{ W}$. A HWP and a PBS is utilised to control the optical power incident on the nonlinear crystal. A second HWP allows to obtain appropriate polarization for carrying out the phase-matching in OPG. We have used a 100 mm converging lens to focus the pump beam at the center of crystal. The $30 \mu\text{m}$ grating of MgO:PPLN has been utilised for carrying out the OPG. This results in the signal and idler wavelength generation in the 1500 nm band and $3 \mu\text{m}$ band respectively. By optimally changing the nonlinear crystal temperature, the signal and idler frequencies could be tuned over an identical band as that discussed in ‘Chaper 4’ of the present thesis. Further, we separated the signal from pump and idler. We focused the signal beam into a 10 mm long BIBO crystal for carrying out the frequency doubling so as to generate wavelength in the visible (red) band ($\approx 750 \text{ nm}$). By using a dichroic mirror M_2 , we have separated the signal from the frequency-doubled red beam. Consequently, we measured

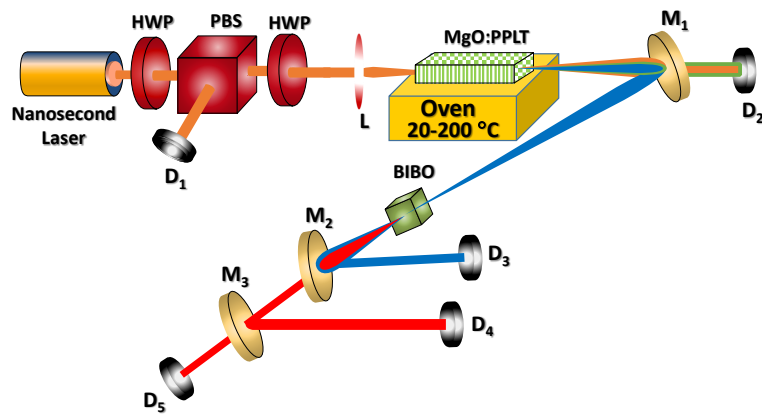


Figure A.1 Experimental set-up for the OPG of the 1064 nm nanosecond laser and SHG of the generated signal beam.

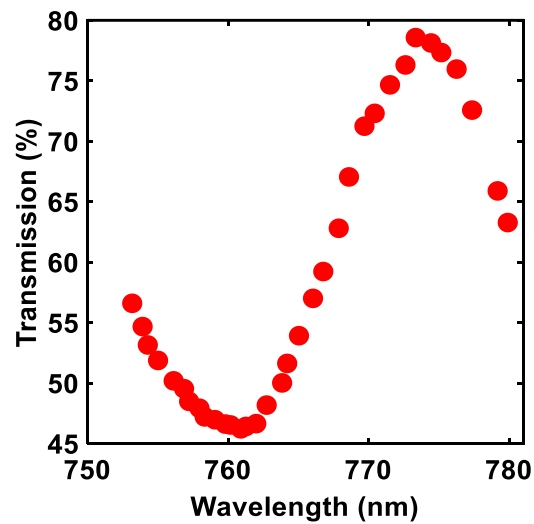


Figure A.2 Transmission of the mirror at different wavelengths

the transmission of mirror M_6 in 'Chapter 4' (M_3 in Fig. A.1) which is plotted as a function of wavelength in Fig. A.2.

Appendix B

M^2 Measurement

Several M^2 measurements have been performed in this thesis. These measurements were basically performed with two set-ups. One is directly with $M^2 - 200s$ instrument which is a plug and play device. And the other is by measuring the beam diameter variation of a focused Gaussian along both sides of the focus. The beam diameter is measured with slit-based beam-profiler (Nanoscan, Ophir)

In order to measure the M^2 we first align the beam with a pair of 45° reflecting mirror and further attenuate it by using HWP and PBS. And then a lens having large focal length $f = 250 \text{ mm}$ is used to focus the beam. Now the beam profiler will measure the beam diameter in X as well as in Y directions at different positions along the both sides of this focus which is shown in the Fig. B.1.

The M^2 has been calculated with the formula

$$M^2 = \frac{\pi \times D_{min}^2}{2\lambda \times 2Z_r} \quad (\text{B.1})$$

Here, D_{min} is the beam diameter at the beam waist, λ is the wavelength and Z_r is Rayleigh length which is defined as $Z_r = |Z_{max} - Z_{min}|/2$ where Z_{max} is the distance along beam propagation where the beam diameter is $\sqrt{2} \times D_{min}$ on one side and the Z_{min} is the distance along the beam propagation on other side where beam diameter is $\sqrt{2} \times D_{min}$. Using Eq.

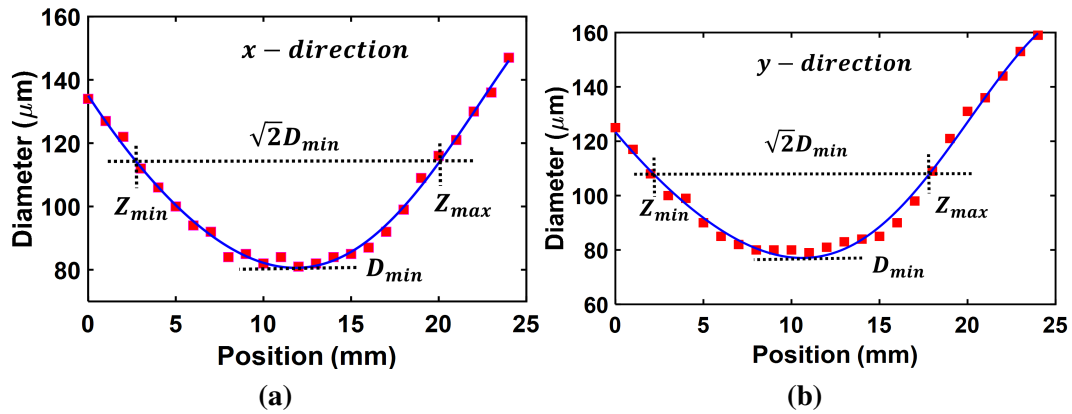


Figure B.1 Variation of the beam diameter to and fro the focus along (a) x -direction and (b) y -direction. The solid lines are the Gaussian fit to the data.

1 we have calculated the M^2 of the generated green from sPPLT crystal to be $M_x^2 \geq 1.11$ and $M_y^2 \geq 1.06$.

